

Copyright
by
Liyang Zhang
2005

**The Dissertation Committee for Liying Zhang Certifies that this is the approved
version of the following dissertation:**

Multiscale Flow and Transport in Highly Heterogeneous Carbonates

Committee:

Steven L. Bryant, Supervisor

James W. Jennings Jr., Co-Supervisor

Larry W. Lake

William R. Rossen

Todd J. Arbogast

Multiscale Flow and Transport in Highly Heterogeneous Carbonates

by

Liyang Zhang, B.S.; M.S.

Dissertation

Presented to the Faculty of the Graduate School of

The University of Texas at Austin

in Partial Fulfillment

of the Requirements

for the Degree of

Doctor of Philosophy

The University of Texas at Austin

August, 2005

Dedication

This dissertation is dedicated to my parents, Zhilin Zhang and Suyun Xie.

Acknowledgements

I would like to express my deep gratitude to Dr. Bryant and Dr. Jennings for their guidance, encouragement, and patience throughout my research. This dissertation could never be completed without their constructive criticism and help.

Thanks also go to Narayan Nair and Jillain Jopling for their help with the experiments, and Ramoj Paruchuri for his previous simulation work. Special thanks to Tony Bermudez. It would have been impossible to set up the experiments without his experience and great assistance. I would also like to thank my colleagues Raman Jha, Xingru Wu and many others who have been helping me in transferring the large experimental apparatus up and down the counter.

I am very grateful to those who shared their knowledge with me during these three years; especially Xingru Wu who offered his generous help and had numerous valuable discussions with me. I would also like to thank Hung Lai for his support and encouragement.

This list would not be complete without thanking my parents and my sisters for their continuous support and trust in my ability to accomplish.

Multiscale Flow and Transport in Highly Heterogeneous Carbonates

Publication No. _____

Liyang Zhang, Ph.D.

The University of Texas at Austin, 2005

Supervisors: Steven L. Bryant and James W. Jennings

Vuggy carbonates often exhibit multiscale features that make rock characterization a challenging problem. Moreover, a thorough understanding of the variability and fluid flow in vuggy carbonates is lacking. Classical theories of flow and transport are not applicable for highly heterogeneous carbonates. Therefore, it is necessary to conduct research on this type of carbonate which is found in many petroleum reservoirs and aquifers. A new method was developed in this research to understand the flow and transport properties of a vuggy carbonate sample. This method combines physical experiments, theoretical modeling, numerical simulations, and high resolution visualizations. The study focused on a Cretaceous carbonate sample containing centimeter-scale vugs. This roughly cylindrical sample, 25 cm in diameter by 36 cm in height, was X-ray CT scanned with a resolution of 0.5 mm.

Effective permeability and transport properties were determined from experiments on three sub-samples from the 36-cm high rock. Single phase flow and transport through

a computational sub-sample was numerically simulated using the parallel subsurface simulator (Parssim). Flow and transport through a touching-vug network, characterized from CT scan data were also numerically simulated.

Seven types of pore space were characterized for the computational sub-sample, whose porosity is 21.6%. The total pore volume in this sub-sample is partitioned into 64% of vugs and 36% of matrix porosity. The vug volume is composed of separate-vugs and a touching-vug network, which account for 21% and 43% of the total pore volume respectively. The touching-vug network is divided into a flowing-vug network and dead-end-vugs, which account for 22% and 21% of the total pore volume respectively.

Study results show that vugs in this sample are interconnected with relatively narrow throats of a few millimeters or less in diameter. Dispersivity in this sample is a non-trivial convolution of at least three phenomena: advection through a flowing-vug network, mass-transfer between the flowing-vug network and dead-end vugs, and transport through the matrix and non-touching vugs. This miscible flooding behavior cannot be simply explained by classical one dimensional convection-dispersion model.

Table of Contents

List of Tables	xii
List of Figures	xiv
Chapter 1 Introduction	1
1.1 Importance	1
1.2 Literature Review.....	3
1.2.1 Groundwater Applications.....	3
1.2.2 Previous Flow Modeling.....	4
1.2.3 Oil Field Applications.....	5
1.2.3.1 Carbonate Permeability Characterization and Prediction .5	
1.2.3.2 General Carbonate Core Sample Studies.....	7
1.2.3.3 Vuggy Carbonate Porosity Classification Studies	10
1.2.3.4 Carbonate Pore Scale Studies	11
1.3 Objectives of This Work.....	12
1.4 Chapter Overview	13
Chapter 2 Vuggy Carbonate Rock Sample	15
2.1 Geological Background	15
2.2 X-ray CT Scan	17
2.3 Porosity Map.....	19
2.4 Sub-samples Introduction	21
2.4.1 Sub-samples Used in Experiments.....	21
2.4.2 The Computational Sub-sample.....	22
Nomenclature.....	31
Chapter 3 Vuggy Rock Micro-structure Visualization	32
3.1 Visualization Software.....	32
3.2 Touching-vug Network Computation.....	33
3.2.1 Flow Path Computations.....	34
3.2.1.1 The Computation Procedure	35

3.2.1.2 Results.....	38
3.2.2 Floodfill Type Study.....	40
3.2.3 Intensity Threshold Study.....	41
3.2.4 Touching-vug Network within the Computational Sub-sample.....	43
3.3 Summary.....	43
Chapter 4 Flow and Transport Experiment Studies.....	54
4.1 Flow Experiments.....	54
4.1.1 Sample A.....	54
4.1.1.1 Apparatus.....	54
4.1.1.2 Effective Permeability Calculation.....	55
4.1.1.3 Experiment Results and Analysis.....	56
4.1.2 Sample B.....	56
4.1.2.1 Experiment Apparatus.....	57
4.1.2.2 Experiment Results and Analysis.....	60
4.1.3 Sample C.....	61
4.1.4 Discussion.....	62
4.2 Conservative Tracer Experiment on Sample C.....	62
4.2.1 Instruments.....	63
4.2.2 Apparatus.....	64
4.2.3 Procedure.....	65
4.2.4 Results and Discussion.....	67
4.2.4.1 Effluent Concentration Analysis.....	68
4.2.4.2 Effluent Concentration History Plot.....	69
4.2.5 Theoretical Dispersion Models.....	72
4.2.5.1 Literature Review on Miscible Flow through Heterogeneous Cores.....	72
4.2.5.2 Dispersion Models Matching of Experiment Four.....	77
4.2.6 Tracer Preferential Flow Tests.....	78
4.3 Summary.....	79
Nomenclature.....	102

Chapter 5 Theoretical Model Calculations	103
5.1 Theoretical Model Calculations on Sample A	103
5.1.1 Model Calculations Assuming Laminar Flow through Connected Vugs	104
5.1.2 Model Calculations Assuming Turbulent Flow through Connected Vugs	106
5.2 Theoretical Model Calculations on Sample C	107
5.3 Summary	110
Nomenclature	118
Chapter 6 Flow and Transport Simulations on Computational Sub- sample	119
6.1 Numerical Simulator and Machines	119
6.1.1 Parallel Subsurface Simulator (Parssim)	119
6.1.2 Machines	121
6.2 Parameters Input to Parssim	122
6.3 Permeability Scale-up Investigation	123
6.3.1 Literature Review on Power Averaging	124
6.3.2 Investigation of Permeability Upscaling Method	125
6.3.2.1 Power Average Method	125
6.3.2.2 Common Vug Cell Method	127
6.4 Single Phase Flow Simulation	129
6.4.1 Vug Connectivity Investigation	129
6.4.2 Comparison of Simulations with Experiments	130
6.4.3 Summary	131
6.5 Conservative Tracer Transport Simulation	131
6.5.1 Physical Dispersion Evaluation	132
6.5.2 Summary	134
6.6 Flow and Transport Simulation on Touching-vug Network System	135
6.6.1 Flow Simulation Results	136
6.6.2 Transport Simulation Results	137
6.6.3 Summary	138

Nomenclature.....	155
Chapter 7 Conclusions and Future Study	156
7.1 Conclusions.....	156
7.2 Future Study.....	159
Appendix A Effective Permeability Derivation for the Bucket Geometry System in Flow Experiments on Sample A.....	161
Nomenclature.....	168
Appendix B Derivation of Effective Permeability of Bundle-of-Capillary-Tubes Assuming Turbulent Flow through Tubes	170
Nomenclature.....	175
Appendix C Sample Parssim Input File	176
References.....	187
Vita	195

List of Tables

Table 3.1	Touching-vug network volumes in the computational sub-sample. The volumes are expressed as the number of voxels in the networks. X0 and X1 are used to indicate two faces of the computational sub-sample at two ends in the x direction. Y0, Y1, Z0, and Z1 are defined similarly. This table shows the volumes of the networks obtained for 15 face combinations in the computational sub-sample. A largest touching-vug network was detected for all 15 cases and it is the only network detected for parallel face combinations (X0-X1, Y0-Y1, Z0-Z1).....	45
Table 3.2	The largest touching-vug network volumes in the computational sub-sample collected from the floodfill type (connection type) study. The “Change” column shows the volume change in percentage compared with the reference volume 774,353. The maximal intensity threshold in these computations was set as 157, identified as the threshold between matrix and vug voxels in the CT scan data.	46
Table 3.3	The largest touching-vug network volumes in the computational sub-sample collected from the intensity threshold study. The “Change” column shows the volume change in percentage compared with the reference volume 774,353. The connection type was set as 6 neighbors in these computations. The table shows that the connected volume is not very sensitive to the threshold when it is between 150 and 170.	47
Table 4.1	Flow experimental results of sample A.....	80
Table 4.2	Screen size distribution of the sand used in the flow experiments shown in Table 4.1.	80
Table 4.3	Flow experimental results of sample B.....	81
Table 4.4	Flow experimental results of sample C.....	81
Table 4.5	Parameters and estimates from four tracer experiments on sample C. ...	82
Table 5.1	Table of size and number of tubes in the capillary-tube model III. Sample C was modeled by 10 types of capillary tubes. Each type tube contains three sections of two diameters with the total length of three sections to be the length of sample C. The number of tubes is summarized for each tube type in this table. A few of such tubes in Model III are shown in Fig. 5.5.	111

Table 5.2	Comparison of results from capillary-tube model with those from experiment four. In the column labeled “Experiment four”, the pore volume of sample C was from the CT scan; other parameters were from experiment four.	111
Table 6.1	Grid cells at each upscale level.	140
Table 6.2	Hierarchy of seven types of pore volumes in the computational sub-sample.	140

List of Figures

- Figure 2.1 Illustration of a typical 4-6 cm diameter Cretaceous (Albian) caprinid fossil in Central Texas (Wilson, 1975). 24
- Figure 2.2 Sketch of X-ray CT scan volume. The CT scan voxels corresponding to the box of volume 28 cm × 28 cm × 36 cm are 512 × 512 × 240. The CT scan resolution is 0.547 mm × 0.547 mm × 1.5 mm. One of the 240 scan slices of 1.5 mm thickness is indicated in the sketch. 24
- Figure 2.3 Two horizontal CT scan slices of the carbonate rock sample. These two slices are randomly taken from 240 slices obtained from CT scan. Each slice is one voxel thick of thickness 1.5 mm. Each slice includes voxels of 512 × 512 with each voxel a square of 0.547 mm × 0.547 mm. 25
- Figure 2.4 Average fraction of vug voxels at each horizontal CT scan slice. The number of vugs at each slice was normalized by the total voxels in the rock sample at each slice. This figure also indicates the locations of four sub-samples illustrated in Fig. 2.7 and Fig. 2.9. 26
- Figure 2.5 Porosity histograms. This picture shows results directly from two X-ray CT scans. The second scan result was filtered and edited. The results obtained are also plotted in this figure. The edited scan was used in subsequent calculations. 27
- Figure 2.6 Illustration of a categorization of vuggy pore space. The flowing-vug volume is indicated by dashed arrows. The total pore space includes matrix and vugs. The total vugs in the pore space include separate-vugs and vugs in the touching-vug network. The vugs in the touching-vug network include dead-end vugs and vugs in the flowing-vug network. These seven types of pore space were quantified for the computational sub-sample as shown in Table 6.2. 28
- Figure 2.7 Illustration of the relative positions of three sub-samples used in the experiments. The interface between sample A and sample B corresponds to CT scan slice 71. The interface between sample C and the top portion of sample B corresponds to CT scan slice 149. 29
- Figure 2.8 Photographs of the three rock sub-samples sketched in Fig. 2.7. 29
- Figure 2.9 Computational sub-sample cross-section sketch. 30
- Figure 3.1 ConnectedComponents module in Amira. 48

Figure 3.2	Computational sub-sample with two extra faces at two ends of the computational sub-sample in the x direction.	49
Figure 3.3	A snapshot of the largest touching-vug network in the computational sub-sample computed from CT scan data using Amira. The transient blue color in the picture shows the background; the surface of touching-vug network is shown as green color. This touching-vug network touches all six faces in the sub-sample. The network contains 774,353 voxels. Some isolated parts seen in the picture were generated by the surface smoothing process and they actually belong to the network.	50
Figure 3.4	Graylevel CT scan data histogram for the computational sub-sample. .	51
Figure 3.5	Touching-vug network volume in the maximal intensity threshold study. The percentage plot uses the volume at threshold 157 as the reference. The plots show that the connected volume is relatively insensitive to the threshold when it is around 160.	52
Figure 3.6	Touching-vug network volume cumulative probability. This plot collected all the touching-vug networks in the computational sub-sample. The largest network contains vug voxels of 774,353.	53
Figure 4.1	Flow experimental apparatus for sample A. C is a container to collect effluent during the experiments. B is the outlet in container C, from which effluent was collected for flow rate measurements.	83
Figure 4.2	Geometric sketch of the combined system in flow experiments of sample A. The flow goes from the top to the bottom.	83
Figure 4.3	Flow experimental apparatus for sample B (denoted as “Rock” in the figure). The rock sample was sealed around the side with the top surface open for water flow through. Water was filled in the big pipe D up to the overflow level. Container C is used to collect effluent from the experiment. Effluent was collected from outlet B for flow rate measurements.	84
Figure 4.4	Flow experimental apparatus for sample B (denoted as “Rock” in the figure). The rock was sealed around the side; water head was built up in tube A; water level in the big pipe D was maintained to be not less than that in tube A. The effluent from outlet F was collected for flow rate measurements.	85
Figure 4.5	Flow experimental apparatus for sample B (denoted as “Rock” in the figure). The rock was sealed around the side. Tubes E and A are connected and the water head built up in tube E was controlled by	

	adjusting the height of tube A. Water level in pipe D was maintained to be not less than that in tube E. Effluent coming out of outlet B was collected for flow rate measurements. Flow goes from the top to the bottom of the rock sample.....	86
Figure 4.6	Rock sealed on a plastic disk, which has a hole in the center that allows water to flow through; the diameter of the hole is 23 cm.	87
Figure 4.7	Flow experimental results of sample B. The plot shows the permeability measured changes with time. With the same water head, the permeability measured decreases with time.....	88
Figure 4.8	Conductivity meter calibration. The slope of the straight line (1.1356) is used in calibrating the TDS reading from the experiment into concentration.....	89
Figure 4.9	Tracer experimental apparatus for sample C, which was built based on the flow experiment apparatus shown in Fig. 4.5. Tube F was added for supplying salt water. Container B is used to collect effluent from the experiment. Port C in the outlet tube is used for placing the conductivity probe. Valves G and H are used to control the supply of either salt water or tap water and they can also control the flow rate. Valve I is used to drain out the fluid remaining on top of the rock sample.....	90
Figure 4.10	Flow capacity and storage capacity diagram for tracer transport experiment four (sample C). This plot was generated using Shook and Forsmann's spreadsheet. The plot shows some 45% of the total flow coming out of 18% of the storage.....	91
Figure 4.11	Effluent concentration history from experiment one. The injecting tracer concentration is 20,000 mg/l. The slug size is 1.6 pore volumes.	92
Figure 4.12	Effluent concentration history from experiment two. The injecting tracer concentration is 20,000 mg/l. The slug size is 0.7 pore volumes.	93
Figure 4.13	Effluent concentration history from experiment three. The injecting tracer concentration is 18,000 mg/l. The slug size is 3.4 pore volumes.	94
Figure 4.14	Effluent concentration history from experiment four. The injecting tracer concentration is 18,000 mg/l. The slug size is 4.1 pore volumes.	95
Figure 4.15	Effluent concentration history from experiment four in dimensionless forms. This figure labels five common characteristics, which are also observed in curves from the other three experiments. The dimensionless	

pore volume was normalized based on the CT scan pore volume of 1142 cm ³ in sample C.	96
Figure 4.16 Effluent concentration history from experiment four. This figure emphasizes the tracer early breakthrough on a log plot.....	97
Figure 4.17 Effluent concentration history from experiment four. This figure emphasizes the long tail in the history plot.....	98
Figure 4.18 Tracer transferring from dead-end vugs into flow paths. The boundary condition is injecting tap water. Fine dashed arrows represent tap water, coarse dashed arrows represent tracer.....	99
Figure 4.19 Effluent concentration histories from experiment four and 1D convection dispersion equation with Peclet number 0.1. The figure shows the analytical solution does match the experimental data poorly.	100
Figure 4.20 Model matching of effluent concentration history from experiment four. The concentration history from the experiment before the end of slug injection was modeled with three analytical solutions from 1D convection-dispersion model with both finite and infinite boundary conditions and Koval model.	101
Figure 5.1 Bundle-of-capillary-tubes model I. This model contains identical capillary tubes of a single diameter through the entire section.....	112
Figure 5.2 Illustration of experimental setup for flow through sample A.....	112
Figure 5.3 Average permeability of the combined system vs. tube radius for laminar flow assumption. In the figure labels, n means the number of the capillary tubes. This figure gives the effective permeability of the combined system for different number of capillary tubes n . The sand permeability is 135 Darcy and the effective permeability is 124 Darcy for the combined system measured from experiment three. The arrow in the figure points to a tube radius of nearly 2,000 microns, which shows the tube radius that corresponds to the intersection of the permeability from the model with $n = 1$ and that from the experiment.	113
Figure 5.4 Average permeability of the combined system vs. tube radius for turbulent flow assumption. In the figure labels, n means the number of the capillary tubes. This figure conveys similar information as that of Fig. 5.3 except this shows the result of turbulent flow assumption in tubes.	114

Figure 5.5	Bundle-of-capillary-tubes model used for modeling sample C. Model II contains different tubes of constant diameters. Model III contains different tubes with each having three sections of two different diameters.	115
Figure 5.6	The effluent concentration profile estimated from capillary tube model III with tube radius and section length shown in Table 5.1. The effluent concentration history from experiment four was also plotted and it showed a good match with the model result.	116
Figure 5.7	Sketch of the largest capillary tube in model III. The constraint of this tube is of size 1 mm in diameter.	117
Figure 6.1	Illustration of composite block. (Cardwell et al., 1944)	141
Figure 6.2	Effective permeability for flow in the x direction. L1, L2, L4 and L8 in the figure represent upscale level 1, 2, 4, and 8, respectively. α is the exponent in the power averaging equation (Eq. 6.1).	141
Figure 6.3	Effective permeability for flow in the y direction. L1, L2, L4 and L8 in the figure represent upscale level 1, 2, 4, and 8, respectively. α is the exponent in the power averaging equation (Eq. 6.1).	142
Figure 6.4	Effective permeability for flow in the z direction. L1, L2, L4 and L8 in the figure represent upscale level 1, 2, 4, and 8, respectively. α is the exponent in the power averaging equation (Eq. 6.1).	143
Figure 6.5	Effective permeability calculated from common vug cell permeability upscale method. The horizontal axis is the number of vugs, a parameter in the common vug cell upscale method; the vertical axis is the effective permeability of the computation sub-sample calculated from the flow simulations on the first upscale level with common vug cell permeability upscale method. The circle and triangular dots in the plots represent the effective permeabilities of the computational sub-sample in the x and z directions calculated from the flow simulations on the first level with 1/3 power averaging permeability upscaling method.	144
Figure 6.6	Dimensionless effective permeability for flow in the x direction. The effective permeability calculated from the simulation and the permeability assigned to vug cells are normalized by the matrix permeability. L1, L2, L4 and L8 in the figure represent upscale level 1, 2, 4, and 8 respectively.....	145
Figure 6.7	Dimensionless effective permeability for flow in the y direction. The effective permeability calculated from the simulation and the	

	permeability assigned to vug cells are normalized by the matrix permeability. L1, L2, L4 and L8 in the figure represent upscale level 1, 2, 4, and 8 respectively.....	146
Figure 6.8	Dimensionless effective permeability for flow in the z direction. The effective permeability calculated from the simulation and the permeability assigned to vug cells are normalized by the matrix permeability. L1, L2, L4 and L8 in the figure represent upscale level 1, 2, 4, and 8 respectively.....	147
Figure 6.9	Dimensionless effective permeability in three directions. The effective permeability calculated from the simulation and the permeability assigned to vug cells are normalized by the matrix permeability. L1, L2, L4 and L8 in the figure represent upscale level 1, 2, 4, and 8 respectively.	148
Figure 6.10	Effluent concentration histories at upscale level 1 for simulations with and without dispersions modeling in the simulations.	149
Figure 6.11	Comparison of effluent concentration history from experiment four with numerical results from simulations on upscale level 1.	149
Figure 6.12	Effluent concentration histories from simulation for upscale level 1 and 8. “L1 wo disp.” shows results from upscale level 1 without dispersion modeling in the simulation. “L1 dispersivity = 1 cm” shows results from upscale level 1 with dispersion modeling in the simulation. Results from upscale level 8 are labeled similarly.	150
Figure 6.13	Velocity streamlines from touching-vug network simulation for flow in the vertical direction. The touching-vug network is shown in Fig. 3.3. ..	151
Figure 6.14	Effluent concentration histories from experiment four and touching-vug network simulation on upscale level 1. The longitude dispersivity used in the modeling was 0.5 cm for both simulations.	152
Figure 6.15	Effluent concentration histories from transport simulation on the touching vug network simulation for the upscale level 2. 100d-network&10md-matrix in the label means that the permeability field at the zero level was assigned as 100 Darcy for vugs in the touching vug network and 10 md was assigned for matrix. 100d-network&1md-matrix in the label means that the permeability field at the zero level was assigned as 100 Darcy for vugs in the touching vug network and 1 md for matrix. This figure shows the more heterogeneous the permeability	

field, the more heterogeneous displayed in the concentration histories. .
..... 153

Figure 6.16 Effluent concentration histories from transport simulation on the touching-vug network simulation on the same permeability field at different upscale level. L1 means upscale level 1; L2 means upscale level 2. The zero level permeability fields for both simulations were 100 Darcy for vugs in the network and 10 md in the matrix. 154

Figure A.1 Cross section sketch for rock permeability calculation. 167

Figure B.1 Geometry of experiment three. 174

Chapter 1 Introduction

This chapter introduces the importance of research on highly heterogeneous carbonates, reviews related studies in the literature on oil field and ground water applications, and summarizes the previous work on flow modeling in vuggy carbonates. The objective of this work is described afterwards. A brief overview of the following chapters is given at the end.

1.1 IMPORTANCE

Carbonate rocks often exhibit a wide range of pore sizes because they commonly contain vugs on a scale of one centimeter or larger. The pore level heterogeneity governs to a large extent the flow and transport properties through carbonates. However, modeling the flow and transport through such a system is difficult because of its high level of heterogeneity. Understanding the physics of flow in vuggy carbonates is particularly a challenging problem because we lack knowledge of the distribution and the connectivity of the vugs. A major hypothesis of this work is that an accurate, fine-scale geometric description of a vuggy sample can be the basis for a better understanding of flow and transport in this type of rock.

Carbonate rocks commonly exhibit more complex features than sandstone formations because the formation of a carbonate often undergoes two geological processes. The initial process of carbonate sedimentation produces particles with a wide range of sizes and shapes after years of deposition in the ocean environment, where organisms are very active. The post-depositional diagenesis process changes the depositional texture and possibly produces more complicated pore size distribution than

the initial carbonate sediments. However, the high level of heterogeneity displayed in the Cretaceous carbonate studied in this research was generated during the sedimentation process. The large vugs (centimeter scale) in the carbonate are the remains of macro organism (such as rudist) that dominated the Cretaceous era. Consequently, the heterogeneities displayed in the vuggy carbonate rocks are often at a centimeter scale or larger.

The vuggy fabrics which are the products of geological processes include a variety of pore types that generally fall into two groups. The first group is composed of non-tectonic fractures, karst conduits, caverns and collapse breccias; and this group is normally associated with karsting and massive dissolution. The second group is composed of interconnected molds that are associated with selective dissolution of fossil fragments, or voids within or between fossils that were never filled in by sediment (Lucia, 1999). In this research, the rock fabric of interest, a multiscale structure system, belongs in the second group.

The study of flow and transport properties of a vuggy system is important for both research and engineering applications for the following reasons. First, studying vuggy porous media will enrich the research on core analysis and modeling because the standard sampling method is on a scale too small to capture the large-scale heterogeneities of the vuggy porous media. The study is also beneficial to modeling because there is no obvious mathematical formalism to accurately model flow through this highly heterogeneous system. Second, developing a better flow model of these multiscale heterogeneities is of both economic and environmental interest for a variety of applications. Fluid flow in carbonates is environmentally important in the movement of groundwater, and economically important in the recovery of hydrocarbons. Groundwater supplies about one third of the water for public, agricultural, and industrial use in the U.S.; over 46% of

the population in the U.S. consumes groundwater according to the 1998 United States Geological Survey. Many of these aquifers are found in limestone formations. Carbonate rocks contain more than 50% of the world's hydrocarbon reserves (Chilingar et al. 1972); many of them exhibit complex geology such as the vuggy porous system described above. A better understanding of the flow and transport properties through this multi-scale heterogeneous system will help remedy or prevent groundwater contamination and reduce risks related to reservoir management.

1.2 LITERATURE REVIEW

1.2.1 Groundwater Applications

Flow and solute transport through porous media with macroscopic heterogeneity has been studied for groundwater applications. These media include fractured and karsted, which were created by dissolution and diagenesis over the years and contain large size holes and conduits. These features are similar to the touching-vug network exhibited in vuggy porous media.

White's (2002) review of studies in karst hydrology found that karst has often been modeled as a triple porosity and permeability system. These three sub systems were matrix, fracture, and conduit, with matrix having the smallest permeability, fracture having intermediate permeability, and conduit (apertures > 1 cm) having the largest permeability.

In the study by Hauns et al. (2001), Fick's Law was used to describe diffusion through a tube (< 1 cm), and an equation similar to the standard convection-dispersion equation for porous media was developed for turbulent dispersion through the tube. The karst conduit was viewed as a tube and the average fluid velocity was considered to be

homogeneous in the tube. The dispersion coefficient in this equation is not proportional to the fluid velocity as in a homogeneous medium. Kosakowski et al. (2001), however, stated that Fick's Law failed to apply to heterogeneous porous media, and they developed a random walk approach to model transport through a fractured till.

1.2.2 Previous Flow Modeling

Some research on modeling of a 2-Dimensional flow through the vuggy carbonate sample of this research has been previously done. Arbogast and Lehr applied Darcy-Stokes equations to the vuggy system, in which the matrix was modeled by Darcy's law and the vug was modeled by Stoke's law. In the study by Arbogast and Brunson, a mixed finite element method was developed to solve the Darcy-Stokes system for a vuggy porous medium. Arbogast and Lehr derived a macro-model, which effectively includes the important information of the Darcy-Stokes micro-model. The effective permeability of the entire system can be calculated using the macro-model. Computation studies were performed on this macro-model by Arbogast et al. (2004).

It was found from the computational results that the effective permeability depends significantly on the connectivity of the vugs. The effective permeability was found to be in the same order as that of the matrix when the vugs are disconnected. However, it was found to be much larger than the matrix permeability when vugs are connected, and it increases with the vug's permeability. In addition, the upscaling from fine grids to coarse grids was found to be complicated because the connectivity of vugs is complicated and an inappropriate upscaling technique may not preserve the topology of vug connections.

1.2.3 Oil Field Applications

This section reviews previous studies of vuggy carbonates in oil field applications by three topics: general carbonate studies, carbonate porosity classification, and carbonate pore scale studies. The first topic reviews the permeability prediction and characterization of carbonate reservoirs, and summarizes the study on carbonate core samples, especially vuggy carbonates. The second topic introduces different porosity categories for vuggy carbonates in the literature. The third topic covers the pore scale studies on carbonates.

1.2.3.1 Carbonate Permeability Characterization and Prediction

To understand carbonate reservoirs, permeability estimation is an important yet a difficult and complex problem because it is mostly predicted from well-log data that may not provide enough formation information. Moreover, the permeability and porosity relationship is difficult to obtain and varies with rock type. An extensive review of predicting permeability for carbonate reservoirs using well-log data is given by Babadagli and Al-Salmi (2004). They reviewed the common permeability prediction methods using well-log techniques, which include the multivariable regression analysis (MRA) and the artificial neural network (ANN). They also thoroughly summarized permeability correlation methods based on pore scale considerations, which include Kozeny-Carman, percolation and many other theories. The ANN technique was used by Badarinadh et al. (2002) for permeability prediction of a heterogeneous carbonate reservoir in the Middle East. They found that the permeability obtained from this method has a good match with that obtained from core studies.

Also using well-log data, Mathisen et al. (2003) developed another method of predicting permeability by first classifying the well-log data into electrofacies types and then applying a nonparametric regression method using well-logs in each electrofacies.

The electrofacies type was defined as rock type, which was obtained from well-log data that reflect minerals and lithofacies within the logging interval. Jennings and Lucia (2003) presented a generalized model to predict permeability using a rock-fabric number that links to the geology. This method was developed to predict the permeability for stratigraphic frameworks with systematical changes.

Reservoir characterization is an important step in predicting flow performance in the subsurface, especially in a heterogeneous carbonate reservoir. Lucia et al. (2003) gave a general description in carbonate reservoir characterization. Azim et al. (2003) characterized a carbonate reservoir in North Kuwait with fractures and vuggy zones. The method they used involved many parameters of the reservoir including geology, geophysical, and petrophysical properties. In characterizing a Lower Cretaceous carbonate reservoir in one of the Abu Dhabi Onshore oil fields, Silva et al. (2002) developed a rock type method honoring the spatial and local changes of properties such as lithology, capillary curves and petrophysical properties for cored wells. For non-cored wells, they resorted to regression, statistical and geostatistical techniques to predict the permeability and the rock type.

A rock type concept was used to characterize carbonate rock based on the pore size distribution (Marzouk et al., 1998, Qassim et al., 2003). The Thamama and Arab reservoirs in Abu Dhabi were studied. In their study, the mercury injection capillary pressure method was used to study the pore size distribution of the carbonates. Shedid and Almehaideb (2002) developed another technique to characterize carbonate reservoirs, which was called characterization number. This method allowed them to create a dimensionless group, which incorporated rock properties, fluid properties, rock-fluid properties and fluid flowing dynamics conditions. They proved that this technique

worked well for a UAE (United Arab Emirates) carbonate reservoir, which had available validation data.

The research methods reviewed in this section mostly apply to carbonate reservoirs or uncored carbonates, which is not the case in our study because our study focuses on one carbonate sample. The following section reviews the studies on carbonate core samples.

1.2.3.2 General Carbonate Core Sample Studies

Core analysis is necessary for reservoir characterization. Vuggy carbonate core samples were studied by Hidajat et al. (2004). Their samples were less than 1.5 in. (3.8 cm) in diameter and were from a West Texas field. The vugs present in their samples were less than 5 mm across. The vuggy core samples were first characterized using routine core analysis methods of mercury capillary pressure, thin section, formation factor, and NMR (nuclear magnetic resonance) T2 measurements. They also obtained a 3-Dimensional porosity map from X-ray CT (Computed Tomography) scanning. In addition, transport properties, the residual oil saturation, and initial water saturation were also measured. They found that the largest permeability and porosity of the six core samples were 2 Darcy and 21.8% respectively. It was also discovered that the semivariograms of the porosity in their samples follow the exponential model with the largest heterogeneity scale of 1.5 cm for one of the six samples. In addition, they correlated the permeability from capillary pressure and NMR using various models and included the connectivity of vugs in the permeability prediction using NMR data.

Egermann et al. (2004) reported a study on vuggy dolomite cores. They found that 1-mm vugs in their samples were disconnected and were embedded in a tight matrix having an average pore-throat radius of 2 microns. A simulation using a pore-network model assuming a homogeneous medium gave reasonable information about water-gas

relative permeabilities. It was observed that the imbibition of water in the matrix was slow due to its small permeability. Imbibition phenomena were simulated with both single and dual-porosity models and the results agreed well with the experiments.

A relative permeability and wettability study was reported for a Lower Cretaceous carbonate by Okasha et al. (2003). Samples of 1.5 in. (3.8 cm) in diameters were studied. They observed from their samples that the wettability of the Lower Cretaceous carbonate had a wide range, which indicated that the carbonates were heterogeneous. The relative permeability results in their study showed that a significant amount of oil was recovered after water breakthrough.

Waterflood through a vuggy carbonate core sample at full reservoir conditions was conducted by Dabbouk et al. (2002). Their sample was from a high permeability layer with the presence of rudist shells and debris in a giant Middle East reservoir located offshore in the Arabian Gulf. Rudist shells and debris distributed with a variable density along this layer. The sample had small vugs and macro-pores from dissolution with a porosity of about 27% and a permeability of about 19 md. Small vugs in this sample were scattered inside the rudist fragments of about 1 cm large. To simulate the waterflood experiments, they input a porosity field obtained from a CT scan, a permeability field from a porosity and permeability relationship, and homogeneous relative permeability and capillary pressure curves with adjustments to fit the waterflood data. A good match of experiments with simulations was obtained in their study.

The recovery mechanisms were studied for a vuggy carbonate core by Dehghani and Kamath (2001). Their sample was 10 cm in diameter with a permeability of 1000 md. They showed that the dispersivity of their core sample was greater than 15 cm, the length of the sample, and the tracer breakthrough occurred at 0.2 PVI (pore volume injected). Their experimental results showed that the oil recovery was greatly enhanced during a

steamflood/blowdown process. The mechanism involved was that the low permeability regions were heated by the vuggy and high permeability regions during high temperature steamflooding, which allowed displacing more oil from the low permeability regions.

Moctezuma-Berthier and Fleury (2000) studied a volcanic vuggy core sample and developed a 3D permeability map using X-ray CT scans, NMR, tracer experiments, and numerical simulations. Their sample was 5 cm in diameter with a porosity of 22% and a permeability of 0.5 md. The vug fraction in their sample was obtained from NMR measurements, which was around 60%. The porosity map in their study did not show any correlation but a preferential flow was observed in tracer experiments. Therefore, they increased the permeability ratio of vug to matrix in a binary permeability field that was input into the streamline simulator to match the experiments. The approach they used to create the binary permeability map is similar to ours, which is explained in Chapter 6. They found that with a permeability ratio of vug to matrix of 360, the simulation results agreed with the concentration profile from the experiment. The preferential flow path or fast path in their sample was characterized as vugs connecting to vugs through the matrix with a shorter distance than that of the slow path. This connection type of one vug to another through matrix is classified as separate-vug, also called isolated-vug, pores by Lucia (1983), which is introduced in Chapter 2.

Waterflood through vuggy carbonates was modeled for a carbonate reservoir in West Texas (Dehghani et al., 1997). The vuggy zones in this study were recognized when a secondary porosity was greater than 8%. It was reported in this study that a large permeability of 5.5 Darcy assigned to vuggy zones resulted in a simulation match with the oil production and water cut histories. The permeability assignment and modeling for a large permeability zone was also studied by Massonnat et al. (2002) and Botton-Dumay et al. (2002). Massonnat et al. modeled the deposition and dissolution process, which

created the large permeability in carbonates, using stochastic approaches. Botton-Dumay et al. developed a methodology to characterize dual permeability in carbonate reservoirs with karst layers.

Waterflood through vuggy carbonates was also studied by deZabala and Kamath (1995). Their core samples were from the Beaverhill Lake formation, Canada with a correlation length of 1 cm. Similarly to the sample in the study by Moctezuma-Berthier and Fleury (2000), deZabala and Kamath found that the distributions of the porosity and permeability of their samples were different from each other. The porosity of the whole core sample in their study was exponentially distributed, which is similar to the porosity distribution of our vuggy sample. They concluded from their study that the conventional core analysis methods including the capillary number and capillary end effect methods failed to explain their experiment data. Therefore, pore-network models were developed (Xu et al. 1999) to analyze the flow and transport through heterogeneous carbonates. Cooper et al. (1999) also used the pore-network model to understand the flow properties of carbonates.

1.2.3.3 Vuggy Carbonate Porosity Classification Studies

Vuggy porosity was determined from the mercury injection technique before the development of X-ray CT scanning in carbonates (Gaulier, 1971). Nowadays, the high resolution CT scanning technique has been increasingly used for vuggy carbonate characterization (Hicks et al., 1992, Dehghani, and Kamath, 1995 and 2001). In Ramakrishnan et al.'s study (1998), the vug porosity was calculated from the CT images. They categorized the porosity of the core samples from the Thamama formation in the Middle East into three groups: vug porosity, intergranular porosity, and intragranular porosity. The total porosity is the sum of these three types of porosity. The vuggy

porosity was the area occupied by voids in the CT image. The intergranular and intragranular porosity were calculated from thin sections.

The same porosity classification was used by Ramakrishnan et al. in 2001 for the Thamama formation. In this study, the vug fraction was estimated from borehole FMI (formation micro-imager) data. They first binarized the FMI images and then calculated the vug porosity as the fraction of the dark voxels (void areas). To find an appropriate threshold in the image data for this calculation, they employed four thresholding methods in their study. In two of their methods, a porosity histogram was used to estimate the threshold and the vug fraction. According to them, the area under the histogram before the threshold is the pore fraction in the matrix. The vug fraction is the difference between the total porosity and the matrix pore fraction.

The vug porosity was partitioned into matrix and fracture systems in the study by Iwere et al. (2002). They considered vugs as pore throats that were larger than 5 microns. They calculated the vug porosity from the pore size distribution, which was obtained from capillary pressure measurements and NMR T2 distributions. The partitioning of the porosity into two systems is required for simulating reservoirs using dual porosity simulators. It was also pointed out in this study that the presence of isolated vugs in the matrix required special treatment with capillary pressure and relative permeability curves because the isolated vugs contributed much to the porosity but very little to the permeability.

1.2.3.4 Carbonate Pore Scale Studies

Pore scale studies have been performed on carbonates by Arns et al. (2004) and Ausbrooks et al. (1999). Arns et al. found that with an increase of the X-ray CT scan resolution, the vuggy porosity of their 5 mm plug sample increased because the higher resolution allowed detecting smaller pores, which increase the vuggy porosity. Vuggy

porosity was defined as the fraction of the pores with radius greater than 100 μm , according to Ramakrishnan et al. (2001). Similarly to Ramakrishnan et al., Arns et al. also set up a threshold for their X-ray attenuation and binarized the image data into pore and mineral phases. Cluster labeling was performed on the pore phase of the binarized image. It was discovered that vugs in their plug sample were disconnected when the X-ray resolution is low, whereas they were connected when the resolution is high. A comparison was made by Ausbrooks et al. in obtaining pore size distribution using different methods of core photos, FMI, NMR, and MICP (mercury intrusion capillary pressure). They observed that the pore size distribution obtaining from these methods was similar. They also concluded that NMR technique was able to capture large size pores in the rock.

A bimodal porous medium was constructed for vuggy carbonates by Moctezuma-Berthier et al. (2004). They considered the real porous medium as two types of medium each having its own porosity and correlation length. One of these media had small pores; the other had large pores like vugs. They found that the single-phase permeability depended mainly on the correlation of the small pores when the vugs were not percolated. When the vugs were percolated, the permeability also depended on the density of the vugs.

1.3 OBJECTIVES OF THIS WORK

There is one significant difference between previous studies and ours: the size of the vugs displayed in the carbonates. Vugs in our sample are as large as 10 cm in length. The presence of large size vugs extends the heterogeneity scale of our sample from microns to tens of centimeters. However, none of the above reported vuggy carbonate core studies had a sample diameter greater than 10 cm. Obviously, cores with less than 10

cm long or diameter are not large enough to include vugs displayed in our sample. Moreover, the heterogeneity in the vuggy carbonates in previous works was much smaller than ours. Even so, there were few reports on petrophysical properties of vuggy carbonates such as relative permeability and capillary pressure mainly because of the difficulties caused by the heterogeneity. Therefore, it is more difficult to characterize the petrophysical properties of a highly heterogeneous carbonate like our sample. In fact, there is even no available technique in the literature to explain the single-phase flow properties such as the permeability, or dispersivity of a sample like ours. As a result, we focus only on the vuggy rock characterization and single-phase flow studies in this research.

The four objectives of this work are to (1) investigate the connectivity of vugs in the studied carbonate sample, (2) study the flow and transport behavior of fluids through the highly heterogeneous rock sample, (3) develop methods to explain flow and transport behavior from experiments and CT scan data, and (4) develop methods to characterize the touching-vug network present in the samples from CT scan data.

1.4 CHAPTER OVERVIEW

This dissertation contains seven chapters, including this chapter. Chapter two introduces the vuggy sample studied in this research. It includes the geology of the outcrop from which the sample was taken, the dimensions of the sample, the X-ray CT scan and the porosity derivation, and the sub-samples used in this research. Three sub-samples were used for physical experiments; one rectangular sub-sample was used for computations. In addition, the pore volume and vug volume of some sub-samples were calculated. Chapter three explains the touching-vug network characterization from CT scan data using visualization software, Amira. A detailed introduction is included to some

functions in Amira that are important to the touching-vug network computation. In addition, the touching-vug volume was calculated. Chapter four explains the flow and transport experiments conducted on the three sub-samples. The experiment apparatus, procedures, results and discussions are provided in this chapter. Chapter five presents the theoretical modeling of flow and transport through vuggy carbonate sample using a simple capillary tube model. Chapter six describes the flow and transport simulations performed for the computational sub-sample. It introduces the numerical simulator and the permeability upscaling techniques. This chapter also illustrates the vug connectivity investigation from flow simulations. Flow and transport simulations on touching-vug network were described as well. Flow volume and dead-end-vug volume were computed for the computational sub-sample in this chapter. Chapter seven summarizes and concludes the research topic and lists the future works.

Chapter 2 Vuggy Carbonate Rock Sample

This chapter describes the geological background and the X-ray CT (Computed Tomography) scanning of a large Cretaceous carbonate rock sample. The sample, 25 centimeters in diameter and 36 centimeters in length, was collected from the Pipe Creek Reef outcrop in Central Texas. The sub-samples of the entire rock that were used in the physical experiments and numerical simulations are also introduced.

2.1 GEOLOGICAL BACKGROUND

Important hydrocarbon reservoirs are found in subsurface rudist reefs: some in Mexico (Coogan et al., 1974) and some in the Middle East (Edgell, 1997). Shelf-margin reefs across south Texas are also successfully explored as petroleum reservoirs (Bebout, 1974). It has been found that outcropping Cretaceous reefs in Central Texas are similar to those reported from the subsurface (Rose, 1963; Perkins, 1974; Bein, 1976).

The Pipe Creek Reef is a well-known Cretaceous (Albian) rudist build-up in the lower Glen Rose Formation in Central Texas (Perkins, 1974). The reef complex was exhumed by Red Bluff and Pipe Creek in south-eastern Bandera County, Texas, and is recognized as the best exposed rudist reef in the world (Petta, 1977). Shell Oil Company drilled 18 shallow wells in this area in the 1950s and 60s; these drilled cores are now held by the Core Research Center at UT Austin.

Rudists are extinct bivalve mollusks from the Jurassic and Cretaceous era that developed massive sessile shells, often with the two valves showing strong asymmetry (Dechaseaux et al., 1969). Rudists usually were attached to the substrate and were either

solitary or in reef-like masses. Caprinids, shown in Figure 2.1, were categorized by Coogan in 1977 as one of the five rudist families involved in the Middle Cretaceous (Albian-Cenomanian) at the Gulf Coast. He classified the caprinids as a more plastic, rapidly changing, and adaptive rudist family in Gulf Coast Cretaceous groups.

Caprinids were found to be the most important reef-building rudists in the Pipe Creek Reef among several different rudist fossils that were observed. Caprinids were transported to the Pipe Creek area during the Cretaceous (Albian) period, and were attached to local substrates such as other mollusks (Petta, 1977). These Caprinids grew and generated young rudists until they completely colonized this area. Living in a high wave energy environment, Caprinids eventually formed the thickest shell walls and most wave-resistant framework compared to other animals in this area. The Caprinid framework was strengthened by the filtering of the fine-grained calcareous sediment into the framework voids and the internal framework cementation (Petta, 1977).

The Caprinid mounds, along with the associated deposits, demonstrate a variety of heterogeneities: decimeter-scale vugs within mound-core caprinid fossils standing upright in sediment; decimeter-scale vugs within and between caprinid fragments in flank beds; a heterogeneous arrangement of mounds, mound-flanking debris deposits, and inter-mound sediment; and the organization of these features in kilometer-scale shore-parallel belts stacked in depositional cycles up to 10 meters thick.

In the Pipe Creek Reef outcrop, vugs in the mound cores were observed primarily inside the caprinid fossils and do not appear to form a connected network. Vugs in the debris deposits, however, are both inside and between the fossilized shells and they do form a strong connected network. The degree and scale of vug interconnections in the debris are to be studied here with a sample collected from the debris area of the reef.

A vug is commonly present as a dissolved grain, fossil chamber, fracture, etc. (Lucia, 1999). It is often pore space that is large enough to be visible by the naked eye. Carbonate pore space is classified by Lucia (1983) into two types: interparticle and vuggy. Interparticle porosity can be both intergranular and intercrystalline. Vuggy porosity is defined as pore space that is within grains or crystals or that is significantly larger than grains or crystals. In other words, vuggy porosity is all the pore space that is not interparticle. Vuggy porosity is subdivided into separate-vug pores (also called isolated-vug pores) if the vugs are interconnected through the interparticle network and touching-vug pores if the vugs are in direct contact with one another independent of interparticle porosity. The addition of a moderate amount of separate-vug porosity to interparticle porosity increases the total porosity but does not significantly increase the permeability as mentioned by Lucia (1983). However, touching-vug porosity can increase permeability well beyond our expectation from the interparticle pore system because the touching-vug pore network may dominate the flow through the system.

2.2 X-RAY CT SCAN

Most of the information in section 2.2 and 2.3 is collected from a progress report to Petroleum Development Oman in March 2001 by Jennings et al. This report showed preliminary CT scan studies, which have not yet been published, on the carbonate sample studied in this research.

The collected rock sample is irregular in shape but roughly cylindrical with dimensions of 25 cm in diameter and 36 cm in length. The sample was scanned with an industrial high-resolution X-ray CT scanner at The University of Texas, Department of Geological Sciences. Compared with medical scanners, this instrument operates at higher

energies with configurable source and detector geometries, which makes it capable of scanning high-density objects with higher resolution (Ketcham et al., 2001).

The Pipe Creek Reef sample was scanned with 240 slices of 1.5 mm thickness. The scanned volume is illustrated in Figure 2.2. Each scanned slice was reconstructed with 512×512 pixels, each of which is a square with sides of 0.547 mm by 0.547 mm. Therefore, the CT scan data of the whole scanned volume, including the outside non-rock volume in the rectangular box (a bucket), was mapped into $512 \times 512 \times 240$ grid cells for future numerical simulations.

Figure 2.3 shows images of two selected slices from the sample. The grayscales in the figure display relative X-ray attenuation, which has an approximate linear relationship with bulk density. Lighter shades in the images indicate denser materials, which corresponds to matrix in our rock sample. The darker shades indicate less dense materials, which correspond to vugs in the sample. The intermediate density shades show vugs that are partially filled by recent sediment when the rock was exposed in the creek bed.

The image data were exported to a binary integer data file with values from 0 to 255. The smaller values in this grayscale data represent less dense material and larger values represent more dense materials. The graylevel histogram of the image data was plotted with an array size of $512 \times 512 \times 240$. Several peaks were observed in the histogram. The peak corresponding to the smaller graylevel values denoted the largest number of voxels having the lightest material, which was air. To reduce the effect of air outside of the rock, the value (42) corresponding to this peak was selected as the lowest gray value for this array. Here “outside” denotes the volume outside the rock but inside the CT scanned volume as shown in Figure 2.2. The range from 42 to 255 was divided into three sub-ranges: 42-79, 80-157, and 157-255. These sub-ranges were used to define

three materials in the CT scanned volume: air, mud, and rock (matrix). The air was further divided into air in the vugs and air outside the rock. Hence, the scanned volume was categorized into four domains: outside, vug, mud filled vug, and matrix. These four domains were each assigned as an integer; thus an indicator file was created which contained four integers. Mud is the recent sediment in the vugs when the rock was exposed to the creek bed. In the following CT scan data computations in this dissertation, mud voxels were considered as vug voxels because modern sediment was not originally present in the rock at depth. Moreover, an attempt was made to clean out mud from the vugs before experiments, as described later. Therefore, it is adequate to consider mud voxels as vug voxels to simulate either the real situation or the experiments.

The numbers of vug voxels were calculated in each of the 240 horizontal slices. The calculated number was then normalized by the total voxels in the rock sample at each slice (Figure 2.4). The normalized vug voxel number is the fraction of vug voxels to the total voxels in the rock sample. The rock was originally in place with the upward direction from slice 1 to slice 240 as shown by the arrow in the figure. This plot shows that on average, the vuggy porosity decreases from the bottom to the top of the sample.

2.3 POROSITY MAP

The linear relationship between the X-ray attenuation (CT scan data) and the density of the material attenuating the X-rays is shown in Eq. 2.1.

$$\rho_i = a + bN_i \quad (2.1)$$

where ρ_i is the density of the material in a voxel i , [ML⁻³],

N_i is the gray level CT scan value for a voxel i ,

a , b are constant coefficients.

The two constant coefficients can be solved by the equations listed below, which have two unknowns.

$$W = \sum_i \rho_i V_i = \sum_i (a + bN_i) V_i \quad (2.2)$$

$$\rho_{air} = 0 = a + b \times 42 \quad (2.3)$$

where W is the weight of the bulk rock sample, [M],

V_i is the volume of a voxel i , [L^3].

The weight of the bulk rock sample is known. The density of the air is approximated to be zero and the gray level CT value for air is 42, which is the lowest gray level threshold. All voxels have the same volume of $0.547 \text{ mm} \times 0.547 \text{ mm} \times 1.5 \text{ mm}$. After the two coefficients a and b were solved from the above equations, the material density in each voxel can be obtained using Eq. 2.1.

Because calcite is the main component of the rock, the porosity also has a linear relationship with the bulk density of a voxel, which is shown in Eq. 2.4. Hence, the porosity of each voxel can be obtained using Eq. 2.4.

$$\phi_i = \frac{\rho_r V_i - \rho_i V_i}{\rho_r V_i} = 1 - \frac{\rho_i}{\rho_r} \quad (2.4)$$

where ϕ_i is the porosity of a voxel i ,

ρ_r is the density of the rock or the density of the calcite, [ML^{-3}].

The histograms of the porosity for two CT scans and two editions on the second scan are shown in Figure 2.5. Because of the heavy noise of the first CT scan, the sample

was rescanned. The second scan was filtered to reduce the noise in the data. This filtered data set was then edited to eliminate the effect of the bucket in the CT scan volume.

There is a hierarchy of void volume in this rock, which can be broken into seven types, illustrated in Figure 2.6. These seven types of pore space were quantified for the computational sub-sample as shown in Table 6.2. They are total pore volume, total vug volume, separate-vug volume, touching-vug network volume, flowing-vug volume, and dead-end-vug volume. Vug volume is a subset of the total pore volume, while separate-vug volume and touching-vug network volume are subsets of vug volume. Flowing-vug volume and dead-end-vug volume are subsets of the touching-vug network volume. The total pore volume includes both the matrix pore space and the vuggy porosity. Some connected vugs in the vug volume form the touching-vug network volume. The rest of vugs in the vug volume form the separate-vug volume. In the touching-vug network system, some connected vugs contribute to flow, others do not. The vugs in this network that contribute to flow form a flowing-vug volume. The dead-end-vug volume is the difference of the flowing-vug volume from the touching-vug network volume.

2.4 SUB-SAMPLES INTRODUCTION

2.4.1 Sub-samples Used in Experiments

A simple sketch, Figure 2.7, is used to help illustrate the positions of the three sub-samples in the original sample. The original sample was sitting within the Pipe Creek Reef outcrop with upward direction as shown by the arrow. Sample A, also called the “small sample,” was cut from the rock after the CT scan. Sample A is about 11 cm high and sample B, also called the “big sample,” is about 25 cm high. After conducting several

experiments on sample B, it was cut in half. Sample C with length of about 10 cm is from the bottom of sample B. These three sub-samples are shown in Figure 2.8.

The cutting surfaces of the sub-samples were compared with the CT scan slices. Slice 71 was found corresponding to the cutting surface between sample A and sample B; slice 149 was found corresponding to the cutting surface of sample C and the other part of sample B. These two slices are labeled in Figure 2.4. The figure shows sample A has the largest number of vug voxels. Sample C has less vugs than sample A but more vugs than sample B because sample B contains a section that has the lowest number of vugs. It is reasonable to expect that connections between discrete vugs are more likely in regions where the vug voxel fraction is larger. Thus, we should expect the permeability of sample C to fall between the permeabilities of samples A and B. This expectation was confirmed by flow experiments on these three sub-samples described in Chapter 4.

The average porosity was calculated by taking an average of the porosity in each voxel in the rock sample. The average porosity of the entire sample was 21.3%. The average porosity of sample C was 21.8%. The pore volume of sample C was calculated with the known porosity and dimensions of each voxel from the CT scan. The result was 1142 cm^3 . Similarly, the vug volume of sample C was calculated, which was the sum of volumes of vug voxels. The result vug volume of 762 cm^3 , a vuggy porosity of 14.6% in sample C, accounts for 67% of the total pore volume. The pore volume of sample C is compared with the pore volume measured from the tracer experiments explained in Chapter 4.

2.4.2 The Computational Sub-sample

A rectangular sub-volume of the CT data, central within the rock volume, was selected for numerical investigations introduced in Chapter 6. This computational sub-

sample (Figure 2.9) of size $13.125 \text{ cm} \times 13.125 \text{ cm} \times 21.6 \text{ cm}$ corresponding to $240 \times 240 \times 144$ CT voxels was selected starting from slice 137 in the x and y directions and slice 49 in the z direction. The slices correspond to this computational sub-sample are also labeled in Figure 2.4, which are between slice 49 and slice 193. The computational sub-sample was selected for numerical simulations instead of the entire volume of the sample because the current available computer clusters are not capable of processing large data set efficiently. The other reason of choosing this computational sub-sample was to have rectangular boundaries that are convenient to handle in numerical simulations. This computation volume was also used for investigations of the vug connectivity explained in Chapter 3.

The seven types of pore volume in the hierarchy described above were calculated for the rectangular computational sub-sample. The calculations of the pore volume and vug volume are explained in the following; the calculations of the others are explained in sections 3.2.1.2 and 6.6.1. The pore volume of the computational sub-sample was found to be 806 cm^3 , which corresponds to an average porosity of 21.6%. The vug volume in this sub-sample is 517 cm^3 , which accounts for 64% of the total pore volume. This indicates that the vugs account for the majority of the entire pore space and matrix pores only account for 36% of the total pore volume. Nevertheless, the results explained in sections 3.2.1.2 and 6.6.1 show that not all the vug volume contributes to the flow through the system and there are large volumes of separate-vugs and dead-end-vugs present in the sample.

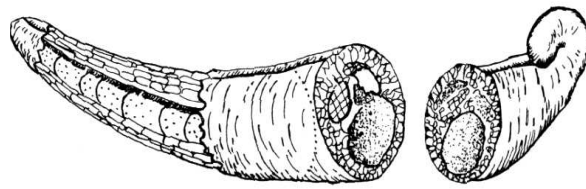


Figure 2.1 Illustration of a typical 4-6 cm diameter Cretaceous (Albian) caprinid fossil in Central Texas (Wilson, 1975).

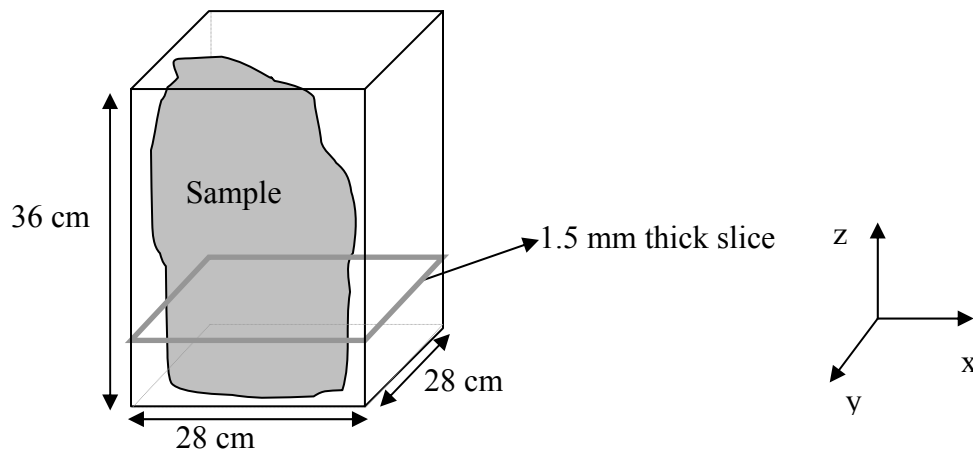


Figure 2.2 Sketch of X-ray CT scan volume. The CT scan voxels corresponding to the box of volume $28\text{ cm} \times 28\text{ cm} \times 36\text{ cm}$ are $512 \times 512 \times 240$. The CT scan resolution is $0.547\text{ mm} \times 0.547\text{ mm} \times 1.5\text{ mm}$. One of the 240 scan slices of 1.5 mm thickness is indicated in the sketch.

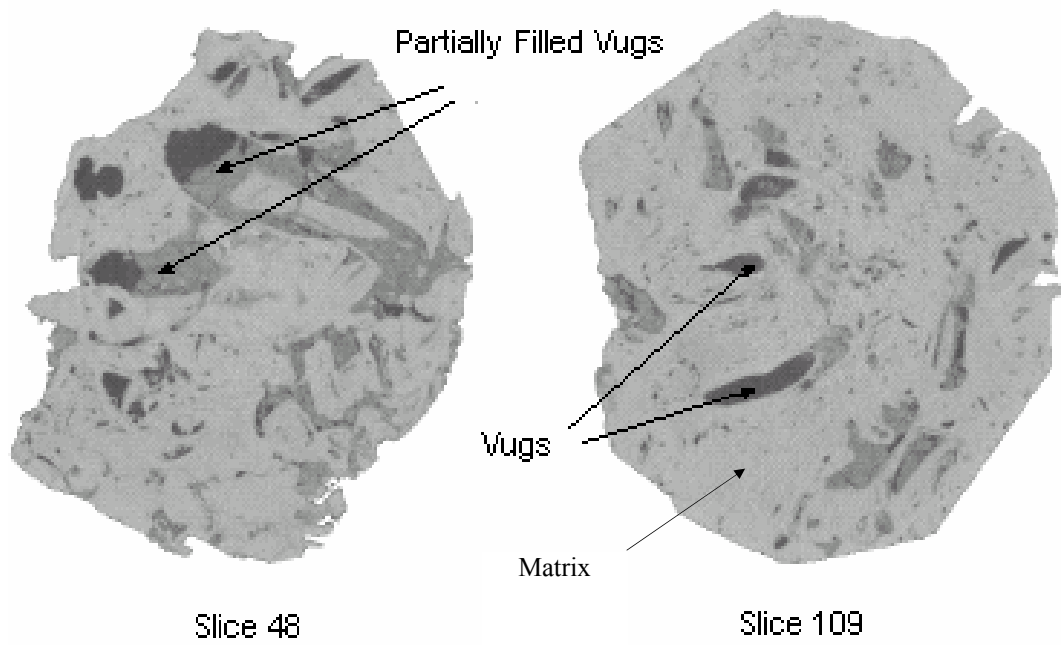


Figure 2.3 Two horizontal CT scan slices of the carbonate rock sample. These two slices are randomly taken from 240 slices obtained from CT scan. Each slice is one voxel thick of thickness 1.5 mm. Each slice includes voxels of 512×512 with each voxel a square of $0.547 \text{ mm} \times 0.547 \text{ mm}$.

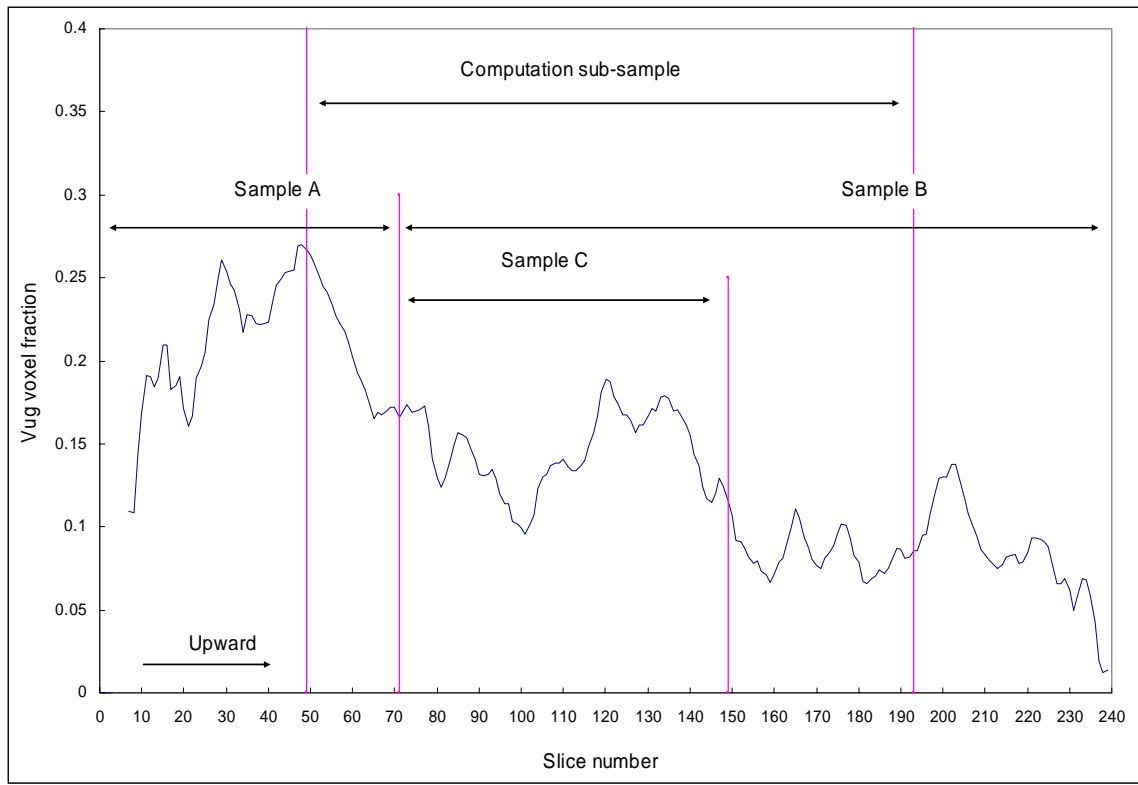


Figure 2.4 Average fraction of vug voxels at each horizontal CT scan slice. The number of vugs at each slice was normalized by the total voxels in the rock sample at each slice. This figure also indicates the locations of four sub-samples illustrated in Fig. 2.7 and Fig. 2.9.

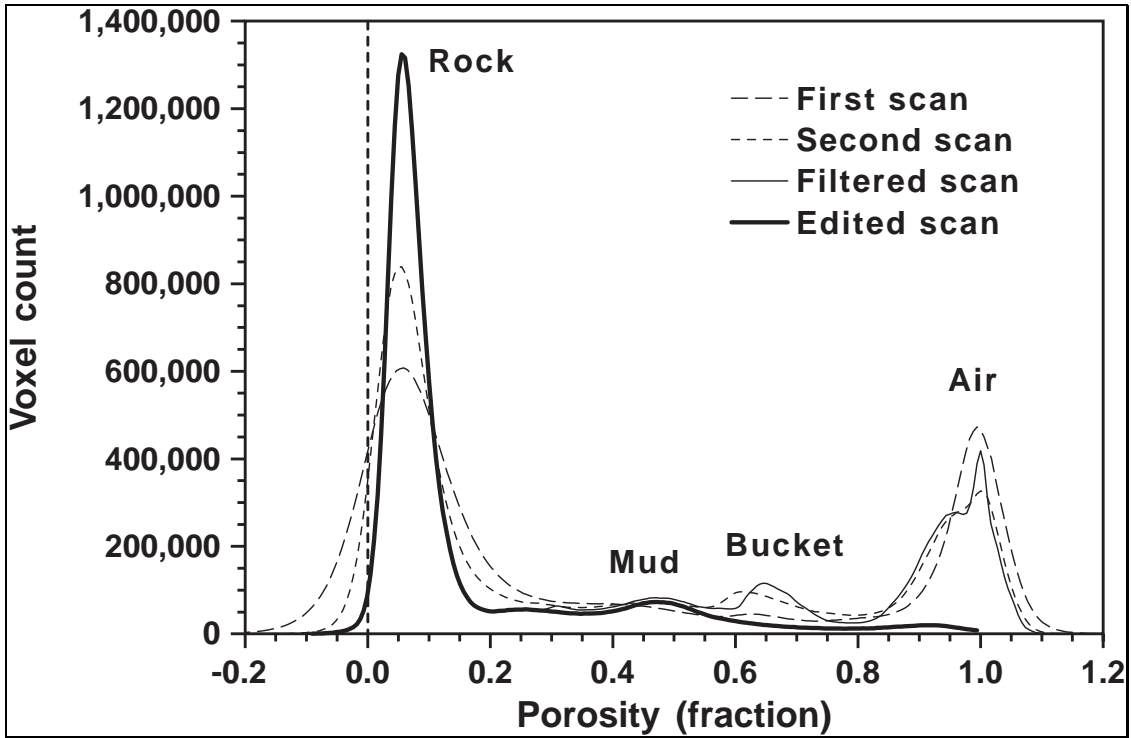


Figure 2.5 Porosity histograms. This picture shows results directly from two X-ray CT scans. The second scan result was filtered and edited. The results obtained are also plotted in this figure. The edited scan was used in subsequent calculations.

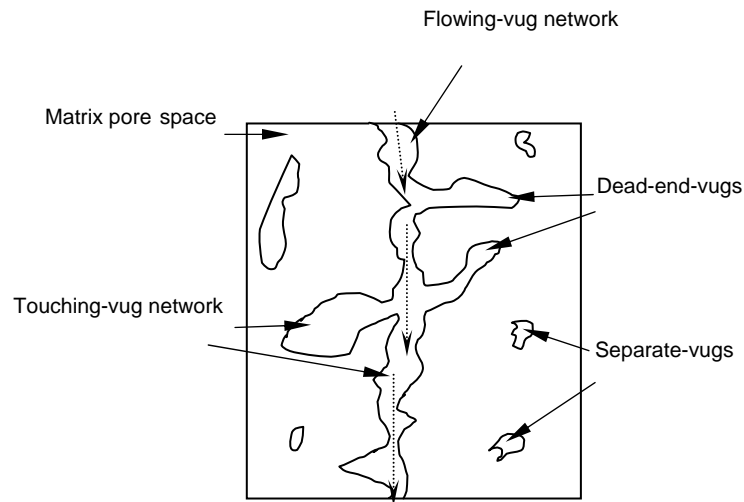


Figure 2.6 Illustration of a categorization of vuggy pore space. The flowing-vug volume is indicated by dashed arrows. The total pore space includes matrix and vugs. The total vugs in the pore space include separate-vugs and vugs in the touching-vug network. The vugs in the touching-vug network include dead-end vugs and vugs in the flowing-vug network. These seven types of pore space were quantified for the computational sub-sample as shown in Table 6.2.

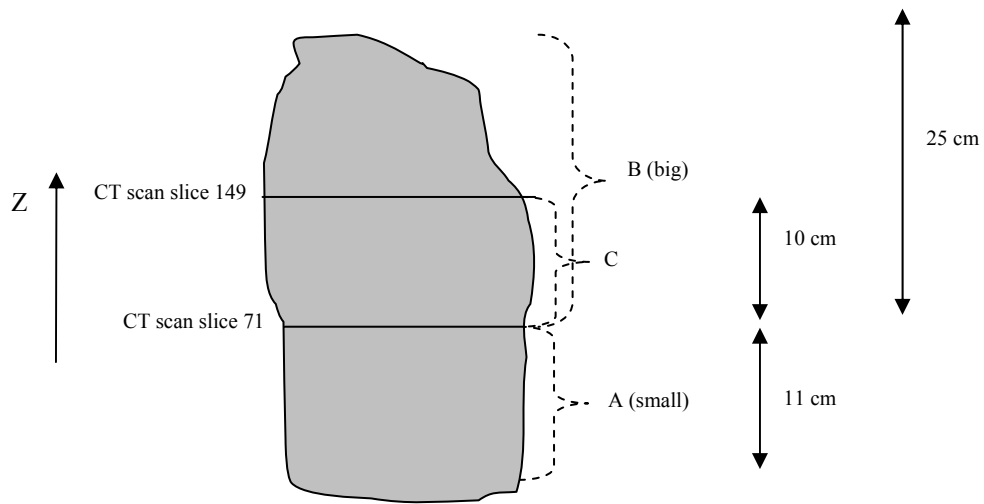


Figure 2.7 Illustration of the relative positions of three sub-samples used in the experiments. The interface between sample A and sample B corresponds to CT scan slice 71. The interface between sample C and the top portion of sample B corresponds to CT scan slice 149.



Figure 2.8 Photographs of the three rock sub-samples sketched in Fig. 2.7.

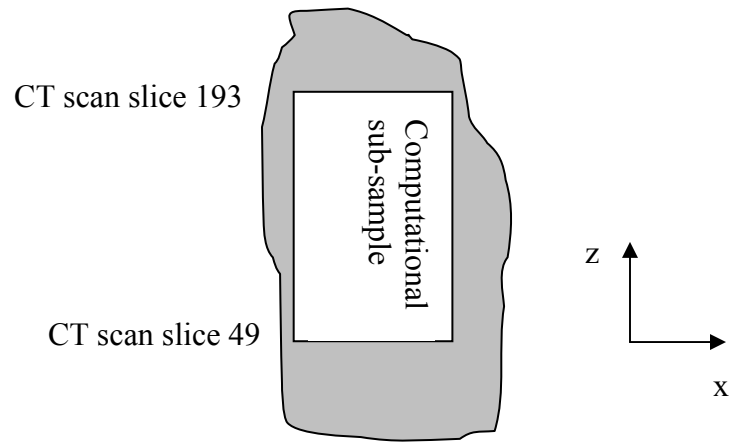


Figure 2.9 Computational sub-sample cross-section sketch.

NOMENCLATURE

ρ_i	Density of the material in a voxel i , [ML ⁻³]
ρ_r	Density of the rock, [ML ⁻³]
ϕ_i	Porosity of a voxel i
a, b	Constant coefficients
N_i	Gray level CT scan value for a voxel i
V_i	Volume of a voxel i , [L ³]
W	Weight of the bulk rock sample, [M]

Chapter 3 Vuggy Rock Micro-structure Visualization

Insight into the vug structure was gained by visualizing CT (Computed Tomography) scan data of the studied vuggy sample using a software package, Amira. This chapter gives an overview of some main functions in Amira. It also explains the touching-vug network computation. A summary is presented at the end.

3.1 VISUALIZATION SOFTWARE

Amira is a commercially available 3-Dimensional visualization and modeling system for advanced visualization, data analysis and geometry reconstruction. The version used in this research is Amira 3.0. Three main functions in Amira are introduced in the following. First, voxel data from X-Ray CT scans can be read into Amira and then processed. Second, new data can be written out in grids suitable for numerical simulation. The output grids can be either rectangular or tetrahedral. Third, Amira includes a general purpose interactive 3D viewer. It allows vector field visualization, such as flow fields computed in this research and 3D image data visualization such as CT, MR (Magnetic Resonance), and Confocal Microscopy. Amira also supports many standard file formats.

This research used some Amira's functions, such as computing connected components, generating 3D surfaces, visualizing surface structure, and visualizing 3D image data and vector fields. The ConnectedComponents module will be introduced in detail because computations using this module were the critical step in understanding vug connectivity. The ConnectedComponents module searches for regions that contain connected voxels in a 3D image volume. The region is a set of voxels whose intensity

values are inside a user-defined range, and are connected to other voxels in the range. Figure 3.1 shows the layout of the ConnectedComponents module.

There are four important “ports” associated with ConnectedComponents module. The first port is Intensity, where users input the minimal and maximal intensity values. If the data are outside this intensity range, voxels are considered to be background. The second port is Floodfill Type, where users select one of the three available neighbor types to define the connectivity type. Neighbors can be defined as sharing a common face, a common edge or a common vertex. Each voxel would have 6, 18 or 26 neighbors, respectively.

The third port is Size, where users input the minimal and the maximal number of voxels to define the lower and the upper size limit of a connected region. Regions with size smaller or larger than this range are considered to be background. Thus a number of regions could be generated with each containing a unique number of voxels. The fourth port is Output, where users select either to generate the Region Field, which is a scalar field of integers, or to create a Spreadsheet, which contains a list of size and position of all detected regions, or both. If the Region Field is checked, the grayscale integers for those voxels that belong to one region are set as a non-zero value, while the integers for the background voxels are set as zero. A value from range 1 to 255 is assigned to each detected region, and these values repeat if more than 255 regions are found.

3.2 TOUCHING-VUG NETWORK COMPUTATION

Two approaches were employed to investigate connectivity of vugs. One approach, introduced in Chapter 6, is to obtain results from numerically simulating the flow through a vuggy system. Vugs are determined to be connected if the vuggy system’s effective permeability increases with the increase of permeability assigned to vug cells

for a series of simulations. The other approach, explained in this chapter, is to compute the network of connected vug voxels using Amira. The studied sample is the computational sub-sample with an array size of $240 \times 240 \times 144$, as described in Chapter 2.2. The connected regions are called “touching-vug” networks in this dissertation.

The general procedure of touching-vug network computations using the ConnectedComponents module is as follows. Rock graylevel CT image data were first read into Amira. The CT data were then processed using the ConnectedComponents module to find the regions that have vug voxels touching together. At this step, appropriate intensity thresholds, floodfill type and region size were selected. Floodfill type can also be called neighbor type or connectivity type. Finally, the computed regions were written out for post processing.

To compute the touching network, the lower limit of the region size was controlled, whereas the upper limit was left open. The open upper limit allows the region size up to the total number of the array ($240 \times 240 \times 144$) in the computational sub-sample. The exact value of the lower region size limit depends on the purpose of computations, which is explained in sections 3.2.1 and 3.2.4. The selections of the floodfill type and intensity thresholds are explained in sections 3.2.2 and 3.2.3.

3.2.1 Flow Path Computations

Since flow through this vuggy system was the main research question, the objective of performing flow path computations was to investigate whether vug voxels are connected into flow paths in the flow direction. A flow path computation method was developed to accomplish this goal. This method assumed the “flow direction” was from one end in the rectangular computational sub-sample to the other end. If at least one region is found containing vug voxels in both of these two ends, we conclude there is at

least one flow path in this flow direction. Regions were computed from the graylevel data of an array size of $240 \times 240 \times 144$ using the ConnectedComponents module. This computation method required two extra faces adding outside of these two ends in the flow direction in the sub-sample. The method is further explained in the following.

In Figure 3.2, the inner box is the rectangular computational sub-sample, shown in Figure 2.7; Face1 and Face2 are two extra layers added on this sub-sample, each layer being one voxel thick. All voxels in Face1 and Face2 were defined as vug voxels. Thus if voxels in Face1 and Face2 are all included in a connected region detected by Amira, then this region spans the computation volume. This is a convenient way to examine whether vug voxels in a connected region connect from Face1 to Face2 and form a flow path in the examined flow direction.

All fifteen face combinations in the rectangular computational sub-sample were investigated. An example is given below to explain the computing procedure using the computation method for vug connectivity investigation in the x direction. The following two subsections explain the procedure and results of flow path computations. For these computations, the maximal intensity threshold was set as 157 and the floodfill type was set as 6 neighbors.

3.2.1.1 The Computation Procedure

The flow path computation method required three important steps. The first step was to find an Array1, which contains a volume that includes all vug voxels in Face1. The second step was to find an Array2, which contains a volume that includes all vug voxels in Face2. The third step was to multiply graylevel integers in Array1 to those of corresponding integers in Array2. The generated result from this step was called FinalArray. The FinalArray obtained from the third step would provide information on whether vugs are connected between Face1 and Face2.

Three sub-steps were needed in the first step of searching for Array1. First, two extra layers of Face1 and Face2 were added on both ends of the computational sub-sample in the x direction. Face1 and Face2 had the same amount of voxels of 240×144 ; thus the new array became a 3D array of $242 \times 240 \times 144$. Second, the graylevel integer 0 was assigned to all voxels in Face1, and an integer 255 was assigned to all voxels in Face2. 0 and 255 are the two extremes of a graylevel integer file. As explained in Chapter 2, 0 represents the lightest material of air and 255 represents the densest material of rock. Therefore, a voxel with integer 0 was considered as a vug voxel, a voxel with integer 255 was considered as a matrix voxel. Till now, Face1 and Face2 were successfully added to the computational sub-sample with Face1 and Face2 containing vug and matrix voxels respectively.

The third sub-step in obtaining Array1 was to compute the touching-vug networks (regions containing connected vug voxels) with minimal region size of 242×144 voxels. Because the connection of vug voxels, not matrix voxels, was investigated, this minimal size allowed us to obtain regions that are larger than the total number of vug voxels in Face1. Therefore, any possible touching-vug network(s) with the number(s) of connected vug voxels larger than 242×144 would be detected and at least one of them contains all vug voxels in Face1.

It was found that multiple touching-vug networks (multiple regions) might be generated from the above computation. A touching-vug network was stored in Amira with one integer assigned for all voxels in this network. Since the number of networks was less than 255, each of the generated networks had an integer that was in the range between 1 and the maximal number of networks. The background voxels that do not belong to any detected network were assigned as 0 by Amira. It was discovered that only one of the generated networks (the largest one) could possibly span across the

computational sub-sample from Face1 to Face2; the rest of the networks were all smaller regions compared to the largest one and could be certainly recognized as of not touching Face2 from Amira visualization. Therefore, voxels in the networks of smaller regions were assigned in Amira as 0, which represented background. Voxels in the network of the largest region were assigned in Amira as 1, which represented vug in this research. If only one touching-vug network was detected, then voxels in this network were assigned as integer 1 automatically by Amira. If no touching-vug network was detected, then all voxels were given 0.

Therefore, at the end of the third step, Array1 was obtained which contained a touching-vug network that included all vug voxels in Face1, and it was a binary file with integers 0 and 1. One must realize that in flow path computations, the integer 0 represented matrix and 1 represented the touching-vug network. This was opposite to the meaning in the graylevel data where both 0 and 1 represent vug. Array1 was a 3D array of size $242 \times 240 \times 144$.

Similarly, Array2 was obtained which contained a touching-vug network that included all vug voxels in Face2. Array2 was also a binary file with integers 0 and 1, and a 3D array of size $242 \times 240 \times 144$.

The third step in the flow path computation was to get a FinalArray by multiplying Array1 and Array2 with the Arithmetic module in Amira. Before the array multiplication, Face1 in Array1 and Face2 in Array2 were snipped out; thus both arrays returned to the size of $240 \times 240 \times 144$ for the original computational sub-sample. Therefore, a voxel with a subscript of (i, j, k) in Array1 would correspond to the same voxel with the same subscript in Array2. Thus the FinalArray was obtained with the size of $240 \times 240 \times 144$.

The Arithmetic module in Amira allows multiplying the integer of a voxel in one array with another integer of a corresponding voxel in another array. Namely, one integer in each of the $242 \times 240 \times 144$ voxels in Array1 multiplied another integer of the same voxel in Array2. Therefore, for the same voxel, either zero or one in Array1 would multiply either zero or one in Array2. If a voxel had integer 1 for both Array1 and Array2, then this voxel must be previously found connecting both Face1 and Face2. Therefore, if a voxel in the FinalArray was found to be 1, then this voxel was determined as a voxel belongs to the flow path in the flow direction. As a result, integer 1 appeared in the FinalArray, then it was concluded that vugs are connected in this flow direction. Otherwise, vugs are not connected in this direction.

3.2.1.2 Results

Flow path computations were performed for all 15 face combinations for the rectangular computation volume. It was found that the FinalArrays in the 15 computations all have integer 1 in them. This suggested that vugs are connected in different directions in the computation volume. The FinalArrays were visualized in Amira. One such result is shown in Figure 3.3, which displays the result of the flow path computation in the vertical direction. The FinalArray corresponding to this computation was exported and the new data set was used to perform numerical simulations, which were called touching-vug network simulations in section 6.6.

The volume of the touching-vug network in the exported data set was calculated. Because the voxels were labeled as either 0 or 1, and 1 represented the voxels that belong to touching- vug network, the arithmetic average of 0 and 1 in $240 \times 240 \times 144$ voxels in the computational sub-sample was the ratio of touching vug network volume to the bulk volume. The calculated result was 0.093359. This indicates that about 9% of the bulk rectangular volume is in the touching-vug network volume. It was determined that the

touching vug-network volume accounts for 43% of the total pore volume in the sub-sample. From the computation result in section 2.4.2, the vug volume accounts for 64% of the total pore volume. Therefore, 21% of the total pore volume was found to be in the separate-vug volume. Nevertheless, it was discovered that not all vug voxels in the touching-vug network contribute to flow and a dead-end-vug volume was detected, which is explained in detail in section 6.6.

To discover the number of voxels in a touching-vug network in a flow direction, another `ConnectedComponents` computation was performed on the `FinalArray`. The minimal and maximal thresholds were both set as 1, which indicated that the focus was only on the touching-vug network (connected vug voxels). The minimal and maximal region sizes were set as 1 and infinite respectively. The connection type was set as 6 neighbors. This type of computations was performed for all 15 `FinalArrays` from 15 face combinations for the computational sub-sample.

The computation results are shown in Table 3.1. In this table, the X0 and X1 face combination gives the connected volume in the touching-vug network for flow in the x direction; the X0 and Y1 face combination gives the connected volume in the touching-vug network for flow from one face in the x direction to one face in the y direction; the rest in the table can be explained in a similar manner. Surprisingly, more than one region was found for some face combinations as seen in the table. We suspected that this might be caused by the 6 neighbor connection type constraint. This connection type created some voxels isolated from the touching-vug network. The table also shows that only the largest region of 774,353 voxels was found for all the parallel faces combinations, i.e. X0X1, Y0Y1 and Z0Z1. However more connected regions were found for almost all non-parallel face combinations, which suggests that some touching-vug networks sitting in the corners of two perpendicular faces were included in the networks obtained from the flow

path computations. These networks have small volumes like those shown in Table 3.1. These smaller regions could not appear for parallel faces combinations because large regions were required to connect two faces. Nevertheless, the largest region of 774,353 voxels was detected for all 15 computations. This indicates that there is a large connected volume in the rectangular computational sub-sample and it touches all six faces.

3.2.2 Floodfill Type Study

Touching-vug network computations were conducted to obtain the connected vug voxels within the rectangular computational sub-sample for different floodfill types. These computations were simply to find touching-vug networks within the sample without worrying about flow. Therefore they were performed directly from the original CT scan data without adding any additional layer like that in the flow path computation. For this set of computations, the intensity threshold was set as 157. The largest connected volumes (touching-vug network volumes) obtained from the computations were selected, which are listed in Table 3.2. The table shows that the connected volume increased with the increase of the neighbors in the connection type. The connection type of 6 neighbors gives the smallest connected volume. This is consistent with the definition of the connection type that 6 neighbors option has the strictest constraint on connections. In addition, the connected volume does not change much when the neighbor type was changed from 6 neighbors to 18 and 26 neighbors. Moreover, the generated network geometry was not affected when using 6 neighbor-type. Therefore, 6-neighbor type was selected for the connected vug computations.

3.2.3 Intensity Threshold Study

The objective of the intensity threshold study was to determine the sensitivity of the connected volume to the threshold. In addition, appropriate intensity thresholds allow for generating reasonable connected vug regions. As mentioned in Chapter 2.2, the smaller the integer in grayscale CT scan data, the lighter the material is. Recall that the focus of computations in section 3.2 is to find connected vugs. Therefore, to consider only vug and mud filled vug voxels, the minimal intensity threshold must be set as the smallest integer in the studied object, and the maximal intensity threshold must be set as an integer between matrix and mud filled vugs. However, it is not obvious which integer to assign for the maximal intensity threshold because there is an obscure range of grayscale data, which are on the border of mud filled vugs and matrix. The results of CT scan data analysis and flow path computations are shown in Figure 3.4, Figure 3.5 and Table 3.3. Figure 3.4 shows the result obtained directly from CT scan analysis. Figure 3.5 and Table 3.3 show the results obtained from CT data computation analysis.

Figure 3.4 shows the histogram of graylevel CT scan data of the rectangular computation volume. Three humps in this plot represent respectively air (vug), mud (mud filled vugs), and rock (matrix) as labeled in the plot. Figure 3.4 displays that the threshold between mud and rock is in the interval between 140 and 180. Two valleys were observed between rock and mud. These two valleys (lower voxel counts in CT data) were studied because a possible intensity threshold would be a graylevel value that corresponds to the lowest point in a valley between mud and rock. One of the valleys corresponds to larger graylevel values; any value in this range would not be appropriate for the threshold because rock voxels were seen obviously in the CT image when graylevel value range was below this possible threshold. Therefore, a graylevel value corresponding to the other valley, 157 (one of the integers from 154 to 161 correspond to

this valley), was selected as the threshold in the CT scan data analysis described in Chapter 2.

With flow path computations, the graylevel data ranging between 100 and 200, which cover the valley range from 140 to 180, were studied. The results are shown in Table 3.3 and Figure 3.5. Floodfill type of 6 neighbors was selected in these computations. Table 3.3 was created following the same procedure of creating Table 3.1 for computations on the rectangular sub-sample in the vertical direction. Table 3.3 shows that the connection volume is zero when the threshold is less than 140. In fact, there is only zero present in FinalArrays computed for these thresholds, which means vugs are not connected in the vertical direction. The table also shows that, in general, the connected volume increases with the threshold when it is greater than 140. The change of volumes from 774,353 (corresponding to the threshold of 157) shown in the table suggests that the connected volume is not very sensitive to the threshold value around 157. This could be observed better in Figure 3.5.

The plots in Figure 3.5 show that the connected volume increases fast when graylevel integer is between 140 and 155 and greater than 165; whereas, this increase is slow for graylevel integer between 155 and 165. This indicates that the connected volume is sensitive to the threshold when it is smaller than 155 and greater than 165. However, the connected volume is less sensitive to the threshold if it is in the interval between 155 and 165. This interval includes most of the interval between 154 and 161 discovered from the graylevel data histogram from the valley between rock and vug. Since 157 is in the middle of the connected volume less sensitive ranges, it was decided to be taken as the maximal intensity threshold in connected vug volume computations.

3.2.4 Touching-vug Network within the Computational Sub-sample

The touching vug network within the computational sub-sample was computed with the maximal intensity threshold of 157 and the connectivity type of 6 neighbors. This set of computations was similar to those described in section 3.2.2. Figure 3.6 shows the statistics of the touching-vug network volume for one computation with the minimal region size of 1 voxel. The plot shows that 99% of the networks (regions) detected have 1000 or less voxels, and 15% of the networks detected have only one voxel in them. In other words, the density probability plot of the touching-vug network volume in this computational sub-sample must be strongly skewed toward the left. This suggests that there are a number of small volumes of touching-vug network in the rectangular computational sub-sample. From the discussion in section 3.2.1, these small connected vug volumes belong to the separate-vug volume. The separate-vugs account for 21% of the total pore volume in the rectangular sub-sample. It was also found that the largest region from this computation contains 774,353 voxels. This result is the same as that discovered in Table 3.1.

3.3 SUMMARY

The visualization computations showed that some of the vugs in the computational sub-sample are connected into a touching-vug network. Moreover, intensity threshold investigations showed that the connection is sensitive to the maximal intensity threshold value when not in an appropriate range. If the maximal intensity threshold is too small, then vugs may lose connections because the small threshold is below the graylevel integer representing mud, and these mud voxels might be the throats connecting vug voxels. The maximal threshold value of 157 was chosen for flow path computations.

In addition, more than 99% of the touching-vug networks were isolated from the largest connected region within the computational sub-sample. This indicates that 99% of the touching-vug networks are separate-vugs, which are separated from the touching-vug network that would allow flow through it. These separate vugs account for 21% of the total pore volume. The results also showed that there is one large touching-vug network having 774,353 voxels that touches all six faces of the computation volume. This implies that there is only one large touching-vug network present in the sample and fluid within this network is able to flow through any direction. In subsequent chapters we will investigate the implication.

Table 3.1 Touching-vug network volumes in the computational sub-sample. The volumes are expressed as the number of voxels in the networks. X0 and X1 are used to indicate two faces of the computational sub-sample at two ends in the x direction. Y0, Y1, Z0, and Z1 are defined similarly. This table shows the volumes of the networks obtained for 15 face combinations in the computational sub-sample. A largest touching-vug network was detected for all 15 cases and it is the only network detected for parallel face combinations (X0-X1, Y0-Y1, Z0-Z1).

Vconnected	X1	Y0	Y1	Z0	Z1
X0	774353	774353	774353	774353	774353
			172	82741	1779
			51		30
			16		
X1		774353	774353	774353	774353
		29016	7210	4058	25
		23258	4298	1409	5
		4058	171	115	5
		14	1	17	2
		1			
		1			
Y0			774353	774353	774353
				82741	1886
				4058	
				124	
				55	
				4	
				3	
Y1				774353	774353
				2009	658
				1389	53
				4	21
					19
					1
					1
Z0					774353

Table 3.2 The largest touching-vug network volumes in the computational sub-sample collected from the floodfill type (connection type) study. The “Change” column shows the volume change in percentage compared with the reference volume 774,353. The maximal intensity threshold in these computations was set as 157, identified as the threshold between matrix and vug voxels in the CT scan data.

Threshold	157	
Neighbors	Vconnected	Change(%)
6	774353	0
18	821843	6.13
26	826100	6.68

Table 3.3 The largest touching-vug network volumes in the computational sub-sample collected from the intensity threshold study. The “Change” column shows the volume change in percentage compared with the reference volume 774,353. The connection type was set as 6 neighbors in these computations. The table shows that the connected volume is not very sensitive to the threshold when it is between 150 and 170.

Neighbors	6	
Threshold	Vconnected	Change(%)
100	0	0
120	0	0
125	0	0
126	0	0
127	0	0
128	0	0
130	0	0
135	0	0
140	366961	-0.53
150	612467	-0.21
155	683787	-0.12
157	774353	0
160	751834	-0.03
165	809591	0.05
170	903036	0.17
180	1042111	0.35
200	2431576	2.14

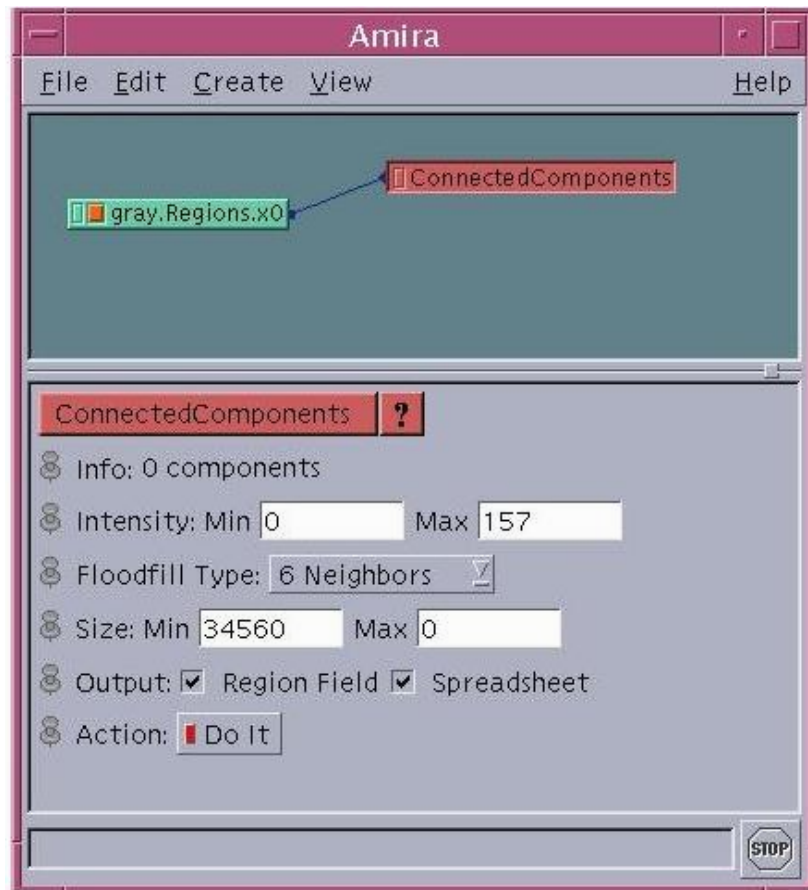


Figure 3.1 ConnectedComponents module in Amira.

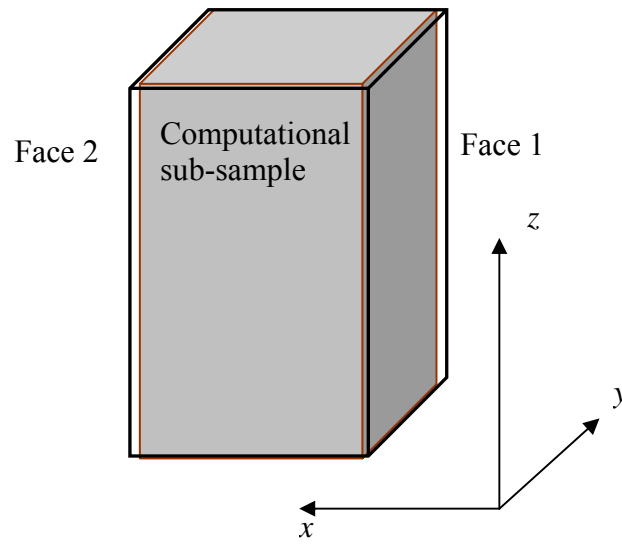


Figure 3.2 Computational sub-sample with two extra faces at two ends of the computational sub-sample in the x direction.

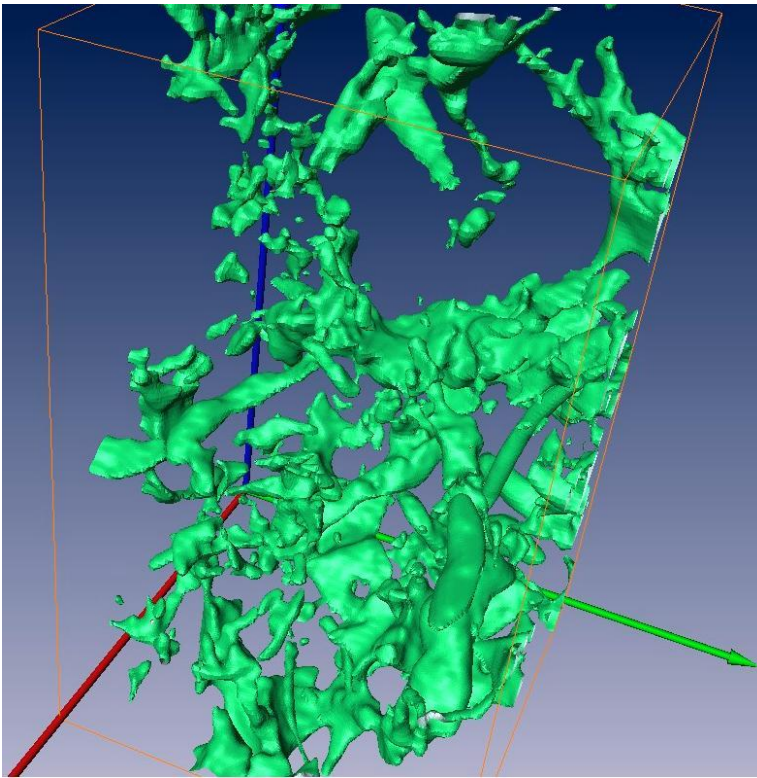


Figure 3.3 A snapshot of the largest touching-vug network in the computational sub-sample computed from CT scan data using Amira. The transient blue color in the picture shows the background; the surface of touching-vug network is shown as green color. This touching-vug network touches all six faces in the sub-sample. The network contains 774,353 voxels. Some isolated parts seen in the picture were generated by the surface smoothing process and they actually belong to the network.

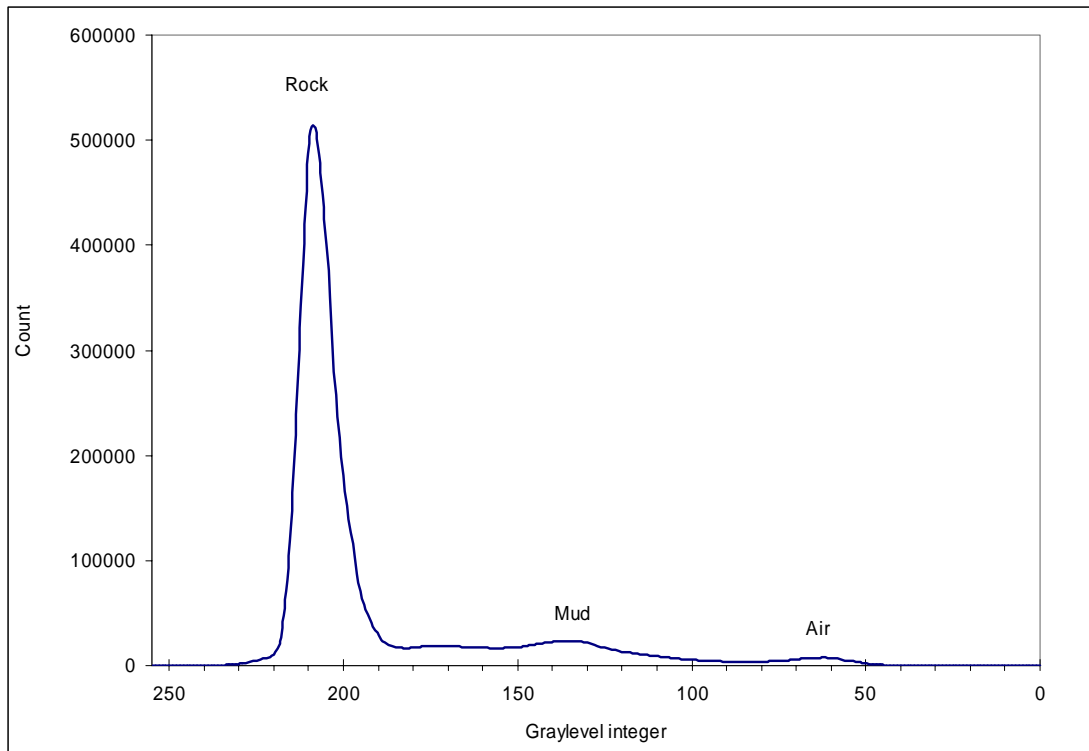


Figure 3.4 Graylevel CT scan data histogram for the computational sub-sample.

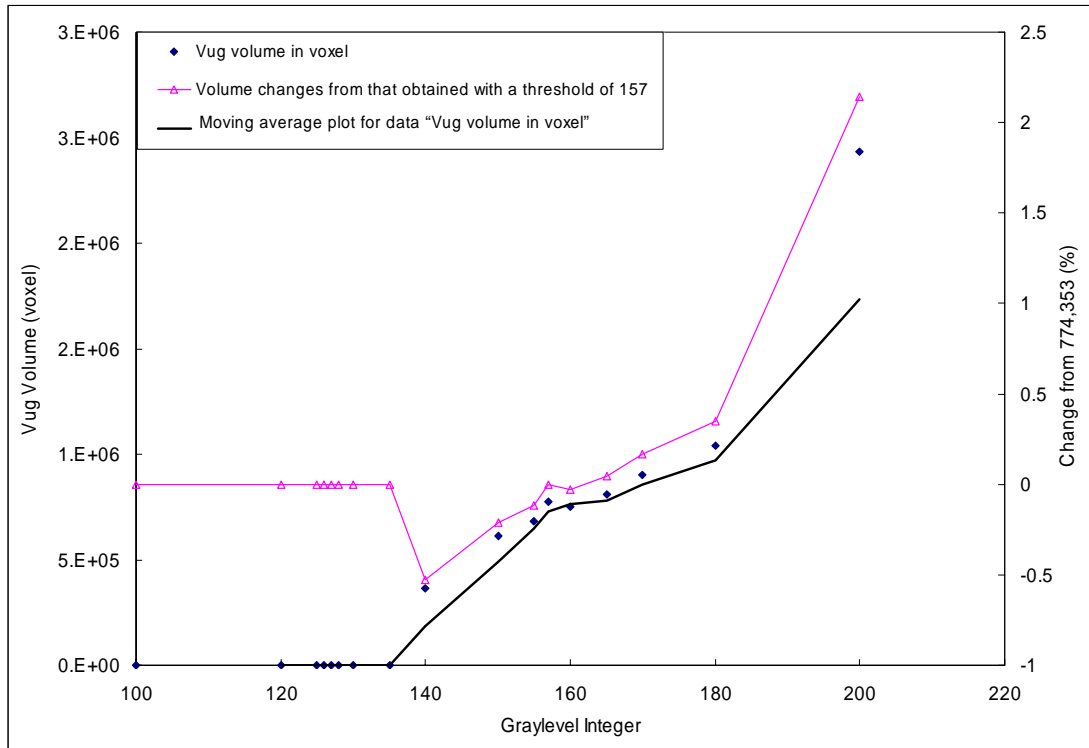


Figure 3.5 Touching-vug network volume in the maximal intensity threshold study. The percentage plot uses the volume at threshold 157 as the reference. The plots show that the connected volume is relatively insensitive to the threshold when it is around 160.

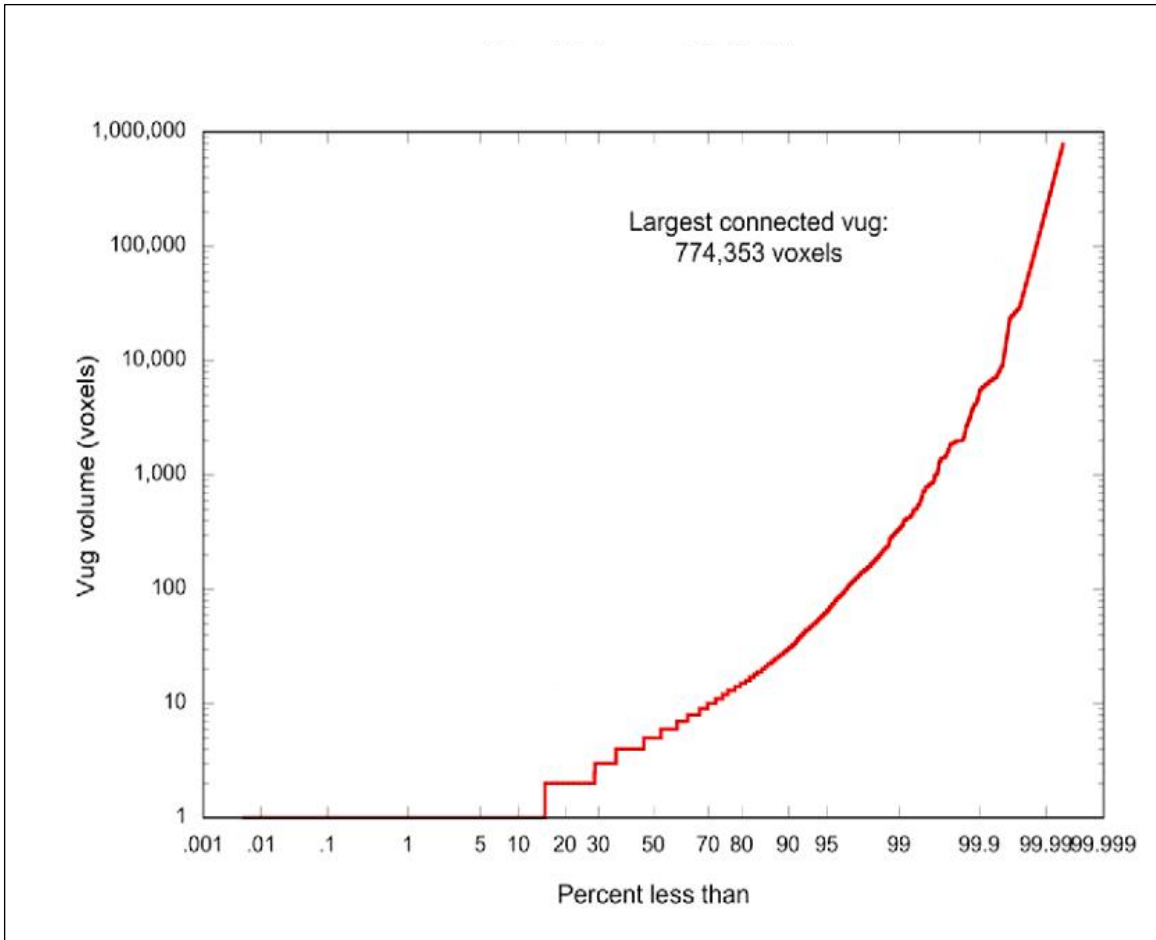


Figure 3.6 Touching-vug network volume cumulative probability. This plot collected all the touching-vug networks in the computational sub-sample. The largest network contains vug voxels of 774,353.

Chapter 4 Flow and Transport Experiment Studies

This chapter explains the flow experiments conducted on three sub-samples. The transport experiments on sample C are also explained. A summary is given at the end.

4.1 FLOW EXPERIMENTS

4.1.1 Sample A

As shown in Figure 2.8, sample A is of irregular shape and has many large vugs on the surface. Flow experiments on this sample were conducted by placing the sample onto a bed of sand within a five gallon bucket. Sand was filled in the annular space between the bucket and the rock. The flow experiment was conducted by supplying water at a constant head.

4.1.1.1 Apparatus

The experimental flow apparatus for sample A is shown in Figure 4.1. A bucket was prepared by drilling some evenly distributed small holes in the bottom, which allowed the water to flow out with negligible resistance. Six layers of small mesh screens were placed onto the bottom of the bucket to prevent sand from falling through the holes. Measurements showed that the screens provided negligible resistance to flow. The bucket was then filled about half-full with coarse sand. Water was allowed to flow through the sand to ensure that it was well packed. Sample A was wrapped in two layers of screen material and placed onto the sand pack in the bucket. The screen material prevents sand from entering the vugs. A rubber ring with a 24 cm opening in the center was placed

between the sand pack and the sample to prevent preferential flow through the annulus between the sample and the bucket. This annulus was then carefully filled in by sand and packed in the same way as before. The bucket and approximate sample dimensions are listed in Table 4.1. Table 4.2 shows the sand grain size distribution.

4.1.1.2 Effective Permeability Calculation

Constant water head at the inlet was maintained by flowing the injection fluid through the overflow A, located a few centimeters above the top of the sample. Effluent water was collected from an overflow outlet B in a large container. The flow measurements were conducted on the combined system of sand and sample A with a length L as shown in Figure 4.2. This system will be referred to as the “combined system” in the following discussion. Steady state flow rates for different water heads were measured by collecting the effluent for certain periods of time. The effective permeability for the combined system was calculated using Darcy’s Law. Eq. 4.1 gives the effective permeability of the combined system with the bucket geometry, from which the permeability of sample A was determined. The derivation of the effective permeability of the combined system and the rock permeability with the bucket geometry is shown in Appendix A.

$$k_{avg} = \frac{q\mu L}{\pi R_1 R_{out} \rho g (h + L)} \quad (4.1)$$

where R_1 is the bucket inner radius at the mouth of the combined system, [L],

R_{out} is the outlet radius (rubber ring radius), [L],

L is the length of the system, [L],

h is the water head above the top of the sample A, [L].

4.1.1.3 Experiment Results and Analysis

Table 4.1 shows the experimental results for sample A. Setup 2 in the table indicated the apparatus that had a section of sand on top of the sample. Setup 3 indicated an apparatus that was filled with impermeable wax around the annulus between the rock and the bucket. A layer of plastic tape was sealed onto the rock surface at this section to prevent wax from falling into the vugs. The results for these different experimental conditions listed in the table show that the permeability ranges from 95 Darcy to 151 Darcy.

The most important observation from these results was that the effective permeability was on the order of 100 Darcy. This large permeability suggested that the vugs in sample A are connected. The large size of vugs in the sample, as shown in the picture (Figure 2.8), might also contribute to the large permeability. However, the large vug sizes alone would not cause the large permeability without vug connectivity. The large permeability indicates the possibility of connections between vugs in sample A. The second important observation was that the effective permeability of the sample was much less than that of the vugs. This is because the largest vug present on the top surface of the sample is about 2 cm in diameter, which could give permeability of far more than 100 Darcy for this vug if it is connected all through the sample with the same diameter. This suggests that vugs are connected through relatively narrow throats.

4.1.2 Sample B

A preliminary experiment was conducted on sample B using the same setup described above for sample A with sand filled in the annulus between the sample and the bucket. In this preliminary experiment, meaningful values of permeability could not be obtained because the flow was going mainly through the sand in the annulus space rather

than through the sample. Hence, a better apparatus was required to allow meaningful flow measurements.

Figure 2.8 shows that compared with sample A, sample B is shaped more as a cylinder and has a smoother surface, which makes it possible to seal the sample's outer surface. Indeed, to seal the side of sample B was the only way to force flow through the rock. However, it was difficult to achieve an effective seal because this sample had an irregular shape, a rough surface, and large vugs that intersected with the surface. The sealing ability of materials such as shrink tube, silicon caulk, plasti-dip, wax, etc. were compared. Air lock was found to be the best seal for sample B. Air lock is a material used in air conditioning ductwork, it is thick and can stick on the rock surface without entering the vugs.

Unfortunately, the pressure at the intersection of the large vugs with the surface was too large to be constrained by the air lock seal especially for longer time periods. For this reason, a small piece of hard plastic was used to block off the largest vug opening (about 2 centimeters) on the rock surface before sealing the rock with air lock. To make a stronger and more effective seal, another material was put on top of the air lock seal. This new material was brushable urethane, which combines the properties of rubber and urethane to form an impact-resistant coating. Brushable urethane is waterproof, adhesive, and can adhere to the air lock.

4.1.2.1 Experiment Apparatus

We attempted to measure the effective permeability of sample B using three apparatuses, shown in Figure 4.3, Figure 4.4 and Figure 4.5. The following is the procedure of constructing the apparatus shown in Figure 4.3. First, sample B was sealed onto a large Lucite disk, which has a hole in the center (Figure 4.6). The hole was slightly smaller than the diameter of the rock, so the disk could hold the rock but did not have

much resistance on flowing effluent. Next, the rock was carefully sealed with several layers of air lock around the outer surface. Finally, a large-diameter PVC pipe was put onto the large disk and they were sealed together.

Tap water was constantly supplied into the large PVC pipe D. The water head was the height difference between the overflow outlet in pipe D and the top of the rock. The flow rate was measured from collecting effluent from outlet B in a certain period of time.

Using the apparatus shown in Figure 4.3, we made an approximate flow rate measurement. The flow rate was tiny even under the highest available water head (0.7 psi over 24 centimeter high rock). The smaller flow rate could be caused by two possible reasons. First, the water head did not supply enough pressure. This was overcome by building a new apparatus shown in Figure 4.4, where a height adjustable tube A was used. The net water head in this apparatus was the height difference between the overflow outlet in tube A and the effluent outlet in pipe E. Pipe E was a tall pipe sealed on top of the rock, which formed a connected system with the rock, and this system was isolated from annulus D. Since tube A was height-adjustable, we were able to reach higher water head than provided by the apparatus shown in Figure 4.3. The flow rate could be measured by collecting effluent coming out of outlet F in a certain period of time. The flow rate measured using this apparatus was still quite small.

The second possible reason of tiny flow rate was that flow was unable to go through the top part of the rock, where the rock had a small permeability due to outcrop weathering. However, it was unknown how deep this weathering process reached into the sample. Therefore, an arbitrary depth of 0.5 cm was selected and some evenly distributed holes were drilled on top of the rock. The holes were each 4.75 mm in diameter. Another reason to build the apparatus shown in Figure 4.4 besides that mentioned in the last paragraph was that we also attempted to test if flow was able to go through from the other

direction. Using this apparatus, flow could go from the bottom to the top of the rock and exit through outlet F in pipe E. Tap water was constantly supplied into tube A during the experiment. The constant water head for a steady state experiment was maintained through the overflowing supplied water.

Unfortunately, because of the leaking of water from the rock to annulus D through the sealing between the rock and the plastic disk, the apparatus shown in Figure 4.4 failed. The third apparatus shown in Figure 4.5 was then constructed. The rock was double sealed with air lock and brushable urethane for this new set up and the large vugs on the surface were blocked by a small piece of hard plastic as mentioned earlier.

In this apparatus, tube A, pipe E, and their connection acted as a connected system. Thus, the water level in tube A was the same as that in pipe E at steady state. The water head in this apparatus was also adjustable by changing the height of tube A. The water level in annulus D was maintained higher than the supply water level in tube A and pipe E as shown in Figure 4.5. This was to ensure that the differential pressure inside the rock did not increase to an extent that it would damage the seal.

The water head was the height of the water above the top of the rock sample. The flow rate was measured from collecting effluent water through outlet B in a certain period of time during the steady state experiment. The effective permeability of sample B was directly calculated using Darcy's law (Eq. 4.2).

$$k_{avg} = \frac{q\mu L}{\pi R^2 \rho g (h + L)} \quad (4.2)$$

where R is the radius of the plastic disk, where the sample open to the air, [L],

L is the length of sample B, [L],

h is the water head on top of sample B, [L].

4.1.2.2 Experiment Results and Analysis

The effective permeability of sample B was calculated from the measurement using the apparatus as shown in Figure 4.3. The approximate result was 35 md. The results obtained using apparatus shown in Figure 4.5 are listed in Table 4.3, where the run number corresponds to the measurement time order. Figure 4.7 shows the change of the permeability and the water head with time. The figure shows that the measured effective permeability of sample B using apparatus shown in Figure 4.5 ranges from 1.1 to 30.8 md, and it changes with water head. Moreover, the permeability has a decreasing trend with time.

These results suggests that there might be some residual mud constraining the flow channel in the sample even though we attempted to remove this recent river sediment by high-pressure washing before building the apparatus. This was further confirmed by the observation of mud collecting in the bottom of the container C, which was flushed out of the rock during the experiments. Perhaps with a decreasing water head, there was less pressure on the mud which then tended to block more of the pore throats, resulting in a smaller permeability measurement.

The conclusion to this experiment is that we did not measure the effective permeability of the sample itself. However, the important information we learned is that the vugs within this rock are connected because the recent sediment would not get into vugs all the way toward the bottom of the sample if vugs were not interconnected. Nevertheless, the smaller permeability compared with 100 Darcy of sample A and the fact that mud was easily trapped suggested that the vugs have narrow connections in this sample.

Flow through this sample eventually stopped with time. This indicates that mud flowing inside the vugs completely blocked some narrow connections, which was

confirmed by the observation of mud inside the vugs that intersect with the rock surface after we disassembled the apparatus. Moreover, mud was observed in the vugs that were within the sample while examining the sample cross-sections after we cut sample B in half. The mud seen on the cross-sections was carefully collected and their positions were labeled accordingly. The size and composition of the collected mud will be further investigated in a future study.

4.1.3 Sample C

Sample C, shown in Figure 2.8, was cut from the bottom of sample B. Flow and transport experiments were conducted on this sample. The flow experiment apparatus was the same as that for sample B, shown in Figure 4.5. The effective permeability measured is listed in Table 4.4.

The table shows that the variation of the effective permeability was relatively small, and the average value was around 12 Darcy. This value was larger than the effective permeability of sample B and smaller than that of sample A. This confirms the prediction in Chapter 2 that the permeability of sample C should fall between that of sample A and sample B. In addition, the reduced size of sample C relative to sample B increases the chances of finding a connected vug network between the top and bottom of the sample. Nevertheless, the most likely cause of the increased permeability of sample C was that additional modern river sediment was cleaned from the vugs after sample B was cut in half.

4.1.4 Discussion

The flow experimental results showed that the effective permeability was on the order of 100 Darcy, 10 Darcy, and 10 md for sample A, sample C, and sample B, respectively, although the permeability of sample B would probably have been larger if more mud could have been removed before the experiments. Nevertheless, it seems reasonable to infer that the permeability of the entire rock increases from top to the bottom, and that the vugs are more interconnected toward the bottom. This conclusion is consistent with the CT scan analysis that there are more vugs towards to the bottom of the sample (Figure 2.4), so there are more chances for vugs to be interconnected.

4.2 CONSERVATIVE TRACER EXPERIMENT ON SAMPLE C

Conservative tracer experiments on sample C were conducted to understand the transport properties in the vuggy sample. Because of the large size and irregular shape of the experiment sample, it is not practical to use techniques such as X-ray CT scan monitoring of the miscible flooding process, which would give detail dispersion information inside rocks. Therefore, typical tracer tests were conducted and effluent concentration histories were analyzed to understand the transport properties.

Sodium chloride was used as the tracer and slug displacement of salt water was conducted. The effluent concentration was measured using a conductivity meter. The effluent fluid was collected and weighed using a laboratory balance. The effluent concentration was then plotted against the cumulative volume of effluent. The conductivity meter, its calibration and the laboratory balance will be introduced in sections 4.2.1 to 4.2.3. The experiment apparatus, procedure and results will be explained in 4.2.4.

4.2.1 Instruments

The Orion Model 115 Conductivity Meter is a portable meter and can be used to measure conductivity, salinity, and total dissolved solids of the fluid. It allows a simple calibration procedure because of the Orion's DirectCal™ direct calibration technique. The TDS (total dissolved solids) mode was used in our experiment. We calibrated the meter based on the provided TDS standard and accessories before using it.

The second calibration of the meter for experimental salt water was performed. A linear relationship exists for concentration of the salt water between the actual value and the meter-measured value. Figure 4.8 shows the plot between actual salt water concentration and the calibrated meter TDS readings. The calibrated TDS readings were the real effluent TDS readings minus the TDS value of the tap water. The effect of TDS in the fresh water was removed from the effluent TDS readings using the calibration in Figure 4.8. The actual effluent concentration was calculated from the calibrated meter reading by a factor of 1.1356, the slope of the straight line shown in Figure 4.8.

A Sartorius laboratory balance, model LC 6200 S, was used in the experiment. The weighting capacity of this balance is up to 5800 gm with a resolution of 0.01 gm. The balance was calibrated appropriately before experiments. The SartoConnect Program was used to transfer the weighting data into Microsoft Excel. An appropriate cable was connected to our computer, which completes the prerequisites for data transmission. The SartoConnect program allows data transmission with a constant time interval. The minimum time interval allowed is one second. In our experiments, the time interval of data transmission was set as three seconds.

4.2.2 Apparatus

The experimental apparatus is shown in Figure 4.9. The new apparatus was based on the flow apparatus shown in Figure 4.5. Another tube F was included in this system in the same way as of building tube A. Tube F and its accessories were identical to that of tube A. The difference was that the previous group was used for supplying salt water, while the latter group was used for supplying tap water. The accessories to tube A and F were respectively valves G and H, which were set to control the supply of the tap water and the salt water. For example, if we open valve G and close H, then tap water from tube A will flow into pipe E; there will be no flow from tube F. Similarly, salt water will go into pipe E from tube F but no flow from tube A when valve G is set close and valve H is set open. Valve I was used to drain the fluid on top of the rock when we switched the rock inlet boundary condition between tap water and salt water. The openings of all the valves used in the apparatus are manually controllable, which helps to adjust flow from tube A and F to pipe E to maintain steady-state flow.

There was one salt water reservoir which is not shown in Figure 4.9. The salt water reservoir was a 30 gallon container, which provided salt water to tube F through the inflow connection as shown by the arrow in Figure 4.9. This reservoir was filled with salt water and was put onto a higher place to continuously supply salt water during the experiment.

A funnel was glued in the bottom of the plastic disk as shown in Figure 4.6; the opening of the funnel was large enough to cover the rock bottom and to collect the effluent. Port C was drilled in the channel part of the funnel, as shown in Figure 4.9. The port was used for placing the conductivity probe, and it was sealed carefully with plumber's putty to prevent effluent leakage. The probe connects to the meter through a cord. The meter was placed on a board that was easily reached by hand. A stop watch

was put on the same board along with the meter and both screens were video taped during the experiments. Port C was drilled as close to the rock outlet as possible to reduce the dead volume at the rock outlet.

One end of a flexible plastic tube was connected to the channel of the funnel, and the other end was placed into a container B. The container B was placed on the laboratory balance. A pair of identical containers was used to collect the effluent during the experiment. This was because the cumulative effluent weight was beyond the range of the balance, and one container needed to be replaced by an empty one when the weight went close to the upper limit. The filled container was then emptied for next round replacement. This iteration continued until the end of the experiment. The cumulative effluent weight was obtained by simply adding the weight of the dumped effluent at the time when the container was switched. Thus the effluent was able to successfully collected and weighed during the experiment.

4.2.3 Procedure

A sufficient amount of salt water of a certain concentration was prepared before starting the tracer experiments. An appropriate amount of salt water was filled into the 30 gallons container, and it was placed onto an appropriate position. A camcorder was setup to record the screens of conductivity meter and the stop watch. The data (TDS reading and time) recorded in the video tape was manually input into Excel after the experiments. The readings were taken at the same time interval as was set up for weight transmission from the balance.

There were five steps in running salt water slug displacements using apparatus shown in Figure 4.9. The second and the fourth steps were critical for the success of the

experiment. The first step was to run steady state flow experiments using tap water as described in section 4.1.2. The second step is explained in detail in next two paragraphs.

The second step was to switch from injecting tap water to salt water. There were two processes in finishing this step and several actions need to be done simultaneously in each process. First, valve G was turned off to stop tap water injection. Meanwhile, valve I was open to drain out the water on top of the rock. The reason for doing this was to make the change in boundary condition for the tracer slug displacement as close as possible to a step change. If the water on top of the rock had not drained, it would have mixed with the incoming water, and the concentration at the inlet of the rock would have varied with time in an unknown way. Second, as soon as the water was depleted, valve I was closed and valve H was opened to allow salt water flowing in. At the same time, an appropriate amount of salt water was poured into pipe E, which was to help build up the salt water as quickly as possible; the other end of plastic tube was placed into container B and the SartoConnect program was initiated to weight the effluent; the stop watch was started.

These two processes must be finished as quickly as possible to reduce the experimental error caused by deviation from the constant head boundary condition. After these two processes, the experiment system still needs to be monitored carefully and valve H may be adjusted if necessary to maintain the constant water head. Keep in mind that the overflow level in tube A was the same as that in tube F; thus the head of salt water was able to back up to the same level as that of tap water and the slug displacement condition was maintained.

The third step was steady-state salt water displacement. The slug time was chosen to be as long as possible without depleting the salt water reservoir. This was to mitigate the effect of the unstable water head error possibly caused by the second step. However,

due to the limitation of salt water reservoir in the current apparatus, the slug size could not be greater than five pore volumes.

The fourth step was to switch back from injecting salt water to tap water, which was similar to the second step. Valve H was closed to stop salt water injection, and valve I was open at the same time to drain out the salt water remaining on top of the rock. Then valve I was closed and valve G was opened to build up tap water on top of the rock. We also poured an appropriate amount of tap water into pipe E to help build up the water head quickly. To assure constant water head, effort was made to finish the whole switching process in a short time.

In the fifth step, tap water displaced the salt water from within the rock. The tap water was allowed to flow until the meter read TDS value of the tap water. The assumption was that at this time the salt water inside the rock was completely displaced. The video recorder was then stopped.

Since both the conductivity meter readings and the corresponding elapsed time shown on the stop watch were recorded, we watched the video tape after the experiment and manually recorded the TDS reading every three seconds. After calibrating the TDS reading as discussed in section 4.2.1, and correcting the weight data as mentioned in section 4.2.2, the effluent concentration, the produced volume, and the corresponding injecting time were obtained. The cumulative effluent volume was the result of weight measured divided by 1.01 g/cm^3 , the salt water density at concentration of 18,000 mg/l and 20,000 mg/l.

4.2.4 Results and Discussion

Four tracer experiments were conducted on sample C. The effective permeability measured was approximately 6 Darcy (Table 4.5), which is about half of that measured in

the previous experiments. This suggests that there was still some mud in the vugs. The measured data from the four experiments are analyzed in the next two sections.

4.2.4.1 Effluent Concentration Analysis

The mean residence time, pore volume of the sample, and a flow capacity versus storage capacity plot were obtained from the effluent concentration analysis in this section. The mean residence time of the injecting tracer was calculated with Eq. 4.3 using the first temporal moment (Shook, 2005). Similarly, the pore volume was calculated from the experiments using Eq. 4.4 (Dwarakanath et al. 1999).

$$\bar{t} = \frac{\int_0^{\infty} C t dt}{\int_0^{\infty} C dt} - 0.5 t_s \quad (4.3)$$

where t is fluid injecting time, [T],

t_s is the duration of the injected tracer slug (Deeds, 1999), [T].

$$\bar{V} = \frac{\int_0^{\infty} C V dV}{\int_0^{\infty} C dV} - 0.5 V_s \quad (4.4)$$

where \bar{V} is the first temporal moment of tracer volume, [L³],

C is the tracer concentration, [ML⁻³],

V is the cumulative volume of fluid injected since the injection of tracer slug, [L³],

V_s is the tracer slug volume, [L³].

At single phase flow and constant flow rate condition, \bar{V} is pore volume of the sample (Maxfield et al., 2002). The calculated results of pore volume in sample C, mean residence time, mass balance, and the CT scan pore volume are listed in Table 4.5. The table shows that the mean residence time is in the range of 3 to 4 minutes. This value is much longer than the nearly 5 seconds (around 0.03 PV) breakthrough time of the tracer. It indicates there is dead-end volume in the sample.

Although the pore volume estimates from the experiments, shown in Table 4.5, are different from the CT scan value, they are similar except for experiment three. The Table also shows that more mass was recovered from tracer tests for the four experiments with errors ranging from 4% to 48%. This might be attributed to the inaccuracy of the instruments.

The flow capacity and storage capacity plot (F-phi plot) was generated from the effluent concentration history from experiment four using the method by Shook (2003) and Shook and Forsmann (2005). This method assumes each flow path as a streamline, and the velocity and the pore volume associated with this streamline are calculated from concentration history data. The calculation result using this method will tell what fraction of the fluid flow comes from what fraction of the total pore volume. The flow capacity and storage capacity plot of our experiment is shown in Figure 4.10. This figure shows a fracture like system that has preferential flow paths present (Shook, 2003). The plot shows some 45% of the flow came from 18% of the pore volume, which indicates that a large amount of flow was contributed by a small amount of pore volume.

4.2.4.2 Effluent Concentration History Plot

The effluent concentration was plotted against volume produced as shown in Figure 4.11, Figure 4.12, Figure 4.13, and Figure 4.14. In the first two runs (run1 and

run2), the injected salt water concentration was 20,000 mg/l. In the last two runs (run3 and run4), the injected salt water concentration was 18,000 mg/l. The slug size was different for each run. Some oscillations observed on the plots at the very beginning were caused by the unstable water head when switching from injecting tap water to injecting salt water. The concentration histories from these four experiments look very similar from the plots in these four figures. Five common characteristics shared by these four plots were observed: early tracer breakthrough, multiple plateaus at high concentration during tracer slug injection, an abrupt concentration drop, and finally, a long concentration tail. The dimensionless form of the plot in Figure 4.14 (experiment four) was plotted in Figure 4.15. The five common characteristics are explained by referring to the plot shown in Figure 4.15.

First, the tracer breakthrough occurs at less than 0.03 pore volume injections (Figure 4.16, which shows effluent concentration from experiment four with logarithmic scale in horizontal axis). Moreover, the concentration climbs up to a higher value very quickly after tracer breakthrough. This strongly suggests that there is at least one fast path within the sample, and the salt water channeled through this path immediately when it was injected.

Second, after tracer breakthrough, concentration had a stepwise increase and multiple plateaus are observed before it reached a maximum value (Figure 4.15). This indicates that there is more than one fast path within the rock sample and they have different breakthrough times. Because the concentration almost reaches the injected value immediately after breakthrough it appears that the first fast path carries the most flow and the other fast paths carry much smaller fractions of the total flow. Moreover, the quickly climbing concentration indicates the salt water goes mainly through fast paths.

Third, there is an abrupt concentration drop (Figure 4.15, Figure 4.16) in effluent concentration history at the end of tracer slug injection. This was because the fresh water broke through immediately along the fast paths when the boundary condition was changed. This is exactly what would be expected from the first observation.

Fourth, the effluent concentration history shows another single plateau (Figure 4.15, Figure 4.16, and Figure 4.17) at lower concentration after tracer slug injection. This suggests that there is some dead-end pore space connected to the fast paths with a relatively slow rate of tracer transferring from dead-end pore space to main flow paths. The mechanism for transport from the dead-end pore space is not clear; it could be a combination of advection, diffusion and mixing.

The other interesting fact is that the length of the single plateau (in pore volume) is related to the size of the slug. For the first two runs, the length of the single plateau is about the same as the slug size (1.6 PV for run 1 and 0.7 PV for run 2). Thus for these experiments it took about the same time for tracer to enter and return from the dead-end-pore space. However, the length of the single plateau is about the same value of 3 PV for the last two runs. This value is smaller than the slug sizes (3.4 PV for run 3 and 4.1 PV for run 4). Therefore, it can be summarized that the length of the single plateau is equal to the slug size when it is less than about 3 PV; whereas the single plateau length remains at 3 PV when slug size is greater than about 3 PV. A possible explanation for this observation is that a dimensionless time of 3 PV is sufficient to fully occupy the dead-end volume in sample C. When a slug size is smaller than 3 PV, the dead-end volume is not fully occupied by tracer during slug injection; when slug size is greater than 3 PV, the dead-end-vugs volume is fully occupied by tracer and the volume is the product of unknown tracer transfer rate and dimensionless time of 3 PV. Figure 4.18 illustrates tracer transferring from dead-end-vugs into flow paths. Unfortunately, there was no way

to measure the tracer transfer rate. So it was not possible to calculate the dead-end volume of sample C from these experiments. However, this volume can be calculated from CT scanning combined with numerical simulation as explained in section 6.6.

Fifth, a long tail is observed in the effluent concentration history (Figure 4.17). This is typical for heterogeneous porous media because it takes long time for salt water to be displaced completely from a smaller permeability pore space.

These five characteristics observed from the plots demonstrate heterogeneity in the sample. There are at least three time scales associated with the heterogeneities. If we identify the connected vugs as a touching-vug network, and further divide it into flowing-vug network and the dead-end-vugs touching the flowing-vug network, then the multiple plateaus observed in the plot correspond to the flowing-vug network and the single plateau corresponds to the dead-end-vugs touching the flowing-vug network. Therefore, the three time scales correspond to the flowing-vug network, the dead-end-vugs connected to the flowing-vug network, and the tracer transfer through matrix pores and isolated vugs. Furthermore, there are also several time scales related to the flowing-vug network because there is more than one fast path observed. This indicates that sample C displays a multiscale system and dispersion in this sample might not be simply explained. Theoretical modeling of miscible flooding is explained in the following.

4.2.5 Theoretical Dispersion Models

4.2.5.1 Literature Review on Miscible Flow through Heterogeneous Cores

The convection-dispersion model (Eq. 4.5) has been widely used to describe 1-Dimensional miscible displacement through homogeneous porous media. Coats and Smith (1964) summarized three analytical solutions to Eq. 4.5 giving three different

boundary conditions for step-input miscible displacement test. The most widely used solution is Eq. 4.7 solved from initial and boundary conditions as follows (Eqs. 4.6).

$$D \frac{\partial^2 C}{\partial x^2} - v \frac{\partial C}{\partial x} = \frac{\partial C}{\partial t} \quad (4.5)$$

where D is the dispersion coefficient, [L^2T],

v is the average interstitial velocity, [LT^{-1}],

C is the flowing concentration, dimensionless,

x is the linear distance, [L],

t is the time, [T].

$$\begin{aligned} t = 0, C(x, 0) &= 0 \\ x = 0, C(0, t) &= 1 \\ x \rightarrow \infty, C(x, t) &\rightarrow 0 \end{aligned} \quad (4.6)$$

$$C = \frac{1}{2} \operatorname{erfc} \left(\frac{x - vt}{2\sqrt{Dt}} \right) + \frac{1}{2} e^{vx/D} \operatorname{erfc} \left(\frac{x + vt}{2\sqrt{Dt}} \right) \quad (4.7)$$

This solution works well for miscible displacement through a finite core if the mixing zone is small compared with the length of the core. However, when a mixing zone is comparable with the core length, Eq. 4.7 can not predict accurately the effluent concentration curve. Brigham (1974) clarified the appropriate boundary conditions for a solution of effluent concentration in miscible displacement through cores when the mixing zone is large. Brenner (1962) applied finite core boundary conditions (Eqs. 4.8) to solve Eq. 4.5. The solution is Eq. 4.9.

$$\begin{aligned}
t = 0, C(x, 0) &= 0 \\
x = 0, C - \frac{D}{v} \frac{\partial C}{\partial x} &= 1 \\
x = L, \frac{\partial C}{\partial x} &= 0
\end{aligned} \tag{4.8}$$

where L is the length of the core, [L].

$$C_D(t_D) = 1 - \left\{ \exp[P(1-t_D)] \times \sum_{k=1}^{\infty} \frac{\lambda_k \sin(2\lambda_k)}{\lambda_k^2 + P^2 + P} \exp(-\lambda_k^2 t_D / P) \right\} \tag{4.9}$$

where t_D is the dimensionless time, $\frac{vt}{L}$,

$$P = \frac{N_{Pe}}{4} = \frac{vL/D}{4}, \text{ dimensionless,}$$

$\lambda_k (k = 1, 2, 3, \dots)$ is the solution of $\lambda \tan \lambda = P$ for odd k ,

$\lambda \cot \lambda = -P$ for even k .

Eq. 4.5 with a finite boundary condition can be used to describe dispersion in a core with its length comparable with the length of the mixing zone. However, it can not predict long tails or asymmetries in effluent concentration histories from miscible displacement experiments because it does not include mass transfer between a flowing and a stagnant region. It was found that long tails in effluent concentration histories are caused by the trapped fluids in stagnant regions gradually seeping into flow channels. A stagnant region can be a dead-end pore region in which fluid is immobile and it transfers to mobile fluid region (Eqs. 4.10). Houseworth (1993) showed that the convection-dispersion model failed to describe these capacitance effects exhibited in the effluent history. Hence, the capacitance model (Eqs. 4.10) has been applied to explain tracer dispersions since Deans (1963) and Coats and Smith (1964). In the literature, the

capacitance model is also called dispersion-capacitance model, dead-end pore model, or three parameters model.

$$\begin{aligned}
 D \frac{\partial^2 C}{\partial x^2} - v \frac{\partial C}{\partial x} &= f \frac{\partial C}{\partial t} + (1-f) \frac{\partial C^*}{\partial t} \\
 (1-f) \frac{\partial C^*}{\partial t} &= K(C - C^*)
 \end{aligned}
 \tag{4.10}$$

where C^* is the concentration in stagnant pores, dimensionless,

f is the fraction of the pore space occupied by mobile fluid, dimensionless,

K is the mass transfer coefficient between stagnant pores and flow channels, $[T^{-1}]$.

The solution to Eqs. 4.10 with semi-infinite core boundary conditions was provided by Coats and Smith. Brigham (1974) clarified the boundary conditions to the capacitance model (Eqs .4.10) similarly to that for the convection-dispersion model (Eq .4.5). Mennella et al. (1999) solved Eqs. 4.10 analytically by employing Brenner's finite core boundary conditions when neglecting mass transfer between stagnant regions and flow channels. Baker (1977) modified the capacitance model based on Brigham's corrections on boundary conditions and found that his experimental data from miscible displacements through a vugular limestone core matched well with his solution to the capacitance model.

Hidajat et al. (2004) employed the capacitance model to characterize vuggy carbonate samples in their study. They found that the stagnant fraction obtained from this model was consistent with the CT images. Narayanan and Deans (1988) and Hicks et al. (1994) also conducted miscible displacements in heterogeneous carbonate cores. In both published works, X-ray CT scanning was employed to observe the flow structure during miscible floods. Using X-ray CT scanning to record the tracer displacement process

provided an accurate way of understanding the rock transport properties. Unfortunately, this method is not feasible for us because it is impossible to fit the bench-scale experiment apparatus in any CT scan instrument. Narayanan and Deans found that centimeter-scale heterogeneity controlled the flow properties through a vuggy carbonate sample from the Gulf-Connor Fenn-Big Valley, Canada. They also discovered that the dispersion in their heterogeneous carbonate sample was convection dominated. A similar fact was also found from miscible flooding on our rock sample.

Deans (1988) and Hicks et al. (1994) also numerically modeled miscible displacements through carbonate cores using the three parameter capacitance model. In their models, they assigned the porosity to each grid cell from CT data, and assigned the permeability from its relationship with porosity. Hicks et al. (1994) found that without considering capacitance effects in their model, the simulation results would not match the experimental effluent concentration histories. However, they discussed that this fact did not prove there were dead-end regions present in the cores. This is because the miscible displacement simulation results depend significantly on the permeability distribution and the porosity-permeability relationships, which were claimed inadequate in their paper.

Moctezuma-Berthier and Fleury (2000) characterized the heterogeneity of their vuggy rock sample using Koval's model. The heterogeneity factor H in Koval's empirical model (Eq. 4.11) increases when the degree of the heterogeneity increases. For a homogeneous system, $H = 1$.

$$c(x,t) = \begin{cases} 0, & t \leq \frac{x}{Hv} \\ \frac{H - \sqrt{Hx/vt}}{H-1}, & \frac{Hx}{v} < t < \frac{x}{Hv} \\ 1, & t \geq \frac{Hx}{v} \end{cases} \quad (4.11)$$

4.2.5.2 Dispersion Models Matching of Experiment Four

An analytical solution from the standard convection dispersion model with a Peclet number of 0.1 was plotted in Figure 4.19 in an attempt to model experiment four. The figure shows that the experiment plot is very different from the analytical solution. Although this analytical solution matches the abrupt concentration drop with the experiment result, it cannot match the two plateau sections displayed in the plot. This mismatch indicates that the transport properties of our sample can not be simply explained by the standard convection dispersion model. Moreover, the Peclet number of 0.1 gives a dispersivity of 100 cm, which is too large for a sample of 10 cm long. This was also observed by Moctezuma-Berthier and Fleury for their vuggy carbonate sample (2000). This suggests that a single dispersivity value in the convection-dispersion model is not enough to explain the dispersion observed in the experiment.

Effort was also made to explain transport through sample C before the end of slug injection. Figure 4.20 shows the effluent concentration history from experiment four and three analytical solutions for a step change boundary condition: the standard convection-dispersion solutions with both infinite and finite boundary conditions and Koval's empirical model solution. The effluent concentration history from Koval's model with heterogeneity factor H of 70 exactly matches that from the 1D convection dispersion model using the infinite boundary condition and a Peclet number of 0.05. Even though both of these parameters indicated a highly heterogeneous system, the analytical solutions could not fit the experimental data. This suggests that sample C is even more heterogeneous. The solution with finite boundary condition with Peclet number 0.1 seems even further away from the experiment result. Therefore, none of the above models can explain the experiment effluent profile. This indicates that the heterogeneity

of sample C can not be explained by these models. In fact, none of the dispersion models to date allow considering heterogeneity in macroscopic scale (Coats and Smith 1964).

4.2.6 Tracer Preferential Flow Tests

Another set of tracer transport tests was conducted to examine the tracer breakthrough time and the fast path volume of sample C. These tests attempted to inject a pulse of tracer, rather than a slug injection as in the experiments described above. A small amount of salt water, compared with the volume of the tap water accumulated on top of the rock, was prepared. First, tap water went through sample C at a constant flow rate. When steady state was achieved, the prepared salt water was injected and mixed completely with tap water in tube E on top of the sample. Meanwhile, the TDS reading on the conductivity meter was monitored. Time recording was stopped when the TDS reading first jumped up to a higher value. The time period recorded between this moment and that of the salt water injection was the breakthrough time of salt water going through the first fast path. The effluent volume collected for this time period was the first fast path volume.

The results showed that at 17 centimeter water head (equivalent to 0.65 psi), the salt water breakthrough time in several tests ranges from 4.1 seconds to 9.7 seconds; the fast path volume ranges from 28 cm³ to 40 cm³. This confirms the previous results that sample C has a fast path with large conductivity, which leads to a short breakthrough time. Since the breakthrough time of 9 s and fast path volume of 30 cm³ were consistent with transport experiment four, these two parameters along with other parameters in experiment four were modeled using the simple capillary-tubes model explained in Chapter 5.

4.3 SUMMARY

The flow and transport experiments on the sub-samples of the Pipe Creek Reef rock can be summarized as follows:

- The effective permeabilities of the sub-samples have a large range: 10 md for sample B, 10 Darcy for sample C, and 100 Darcy for sample A.
- The experimental results strongly suggest that vugs are interconnected. The connections in sample B appear to be constricted by narrow throats, in which mud completely stopped the flow during the experiments.
- The magnitude of the permeability strongly depends on the connectivity of the vugs within the sample. Good connectivity produces large permeability.
- An extremely early breakthrough time (0.03 PVI) and strong asymmetry of the effluent concentration histories indicate both bypassing and the presence of dead-end volume.
- At least three types of pore space were observed for flow through this system: a flowing-vug network forming fast flow paths, dead-end-vugs that touch the flowing-vug network, and a mixture of matrix and separate-vugs.
- Overall, the Pipe Creek sample is highly heterogeneous and flow through this system displays complicated physics that can not be explained by available dispersion models.

Table 4.1 Flow experimental results of sample A.

Run	Sand Only		Rock and Sand					
			Setup 1				Setup 2	Setup 3
	1	2	3	4	5	6	7	8
Water head h (cm)	11	2	4.5	9	15.5	18	3.5	8
Sandpack length L1 (cm)	23	32	19	14.5	8	5.5	20	15.5
Rock height L2 (cm)	-	-	10.5	10.5	10.5	10.5	7	5
Sandpack/air and rock length L3 (cm)	-	-	-	-	-	-	3.5	5.5
Total flow rate (cm ³ /s)	112	83	94	82	95	143	156	98
Apparent permeability of the entire system (d)	135	135	124	124	141	134	146	132
Average permeability of the section contains the rock (d)	-	-	106	110	147	134	121	68
Effective permeability of the rock (d)	-	-	95	102	151	134	113	109

Table 4.2 Screen size distribution of the sand used in the flow experiments shown in Table 4.1.

Grain Size for Sand F35		
screen diameter (μm)	weight (g)	percentage(%)
425	85	46.3
297	87.3	47.6
250	7.7	4.2
210	1.2	0.7
180	1.2	0.7
150	0.4	0.2
<150	0.6	0.3
Total	183.4	100.0

Table 4.3 Flow experimental results of sample B.

Run	1	2	3	4	5	6	7	8
Water head h (cm)	12	15.3	20.8	16.9	11.2	5.9	9.4	9.4
Flow rate (cm ³ /s)	0.011	0.019	0.027	0.023	0.018	0.014	0.012	0.011
Effective Perm. (md)	8.5	18.1	30.8	23.2	13.6	6.9	8.2	7.6
Run	9	10	11	12	13	14	15	16
Water head h (cm)	12.8	9.7	5.5	14.5	19.6	23.8	20.3	16.4
Flow rate (cm ³ /s)	0.011	0.006	0.002	0.005	0.009	0.012	0.009	0.009
Effective Perm. (md)	9.0	4.1	1.1	4.7	9.7	14.8	9.9	8.8

Table 4.4 Flow experimental results of sample C.

Run	1	2	3	4	5	6
Water head h (cm)	15.5	29	13.5	2.5	14.5	23
Flow rate (cm ³ /s)	11.6	17.8	12.6	7.8	12.8	15.3
Effective Permeability (D)	12	11	13	16	13	12

Table 4.5 Parameters and estimates from four tracer experiments on sample C.

Run	1	2	3	4
Water head (cm)	19	15.2	18.5	18.5
Flow rate (cm ³ /s)	7.5	6.5	7.1	7.1
Effective permeability (D)	6.3	6.4	6.2	6.2
CT scan pore volume (cm ³)	1142	1142	1142	1142
Estimated pore volume (cm ³)	1319	1563	1044	1086
Mean residence time (s)	185	248	217	158
Total mass Injected (g)	33	22	63	75
Total mass Produced (g)	43	33	65	81
Total mass Error	0.29	0.48	0.04	0.07

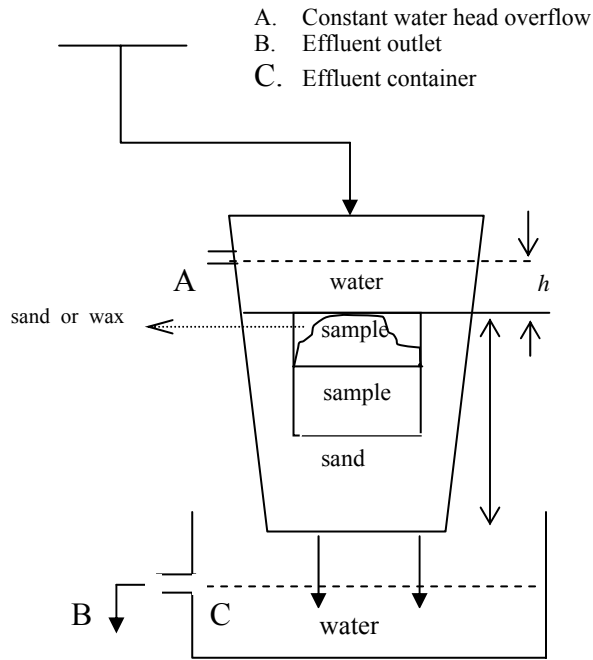


Figure 4.1 Flow experimental apparatus for sample A. C is a container to collect effluent during the experiments. B is the outlet in container C, from which effluent was collected for flow rate measurements.

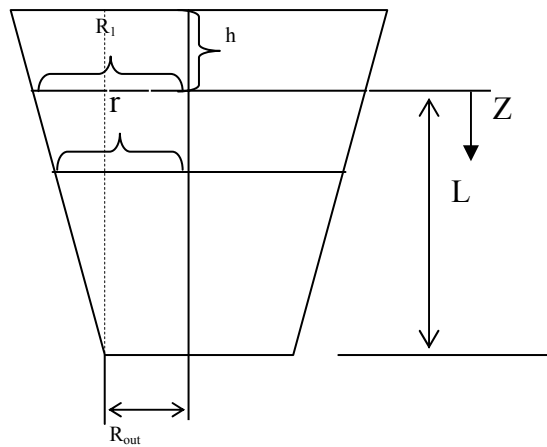


Figure 4.2 Geometric sketch of the combined system in flow experiments of sample A. Flow goes from the top to the bottom.

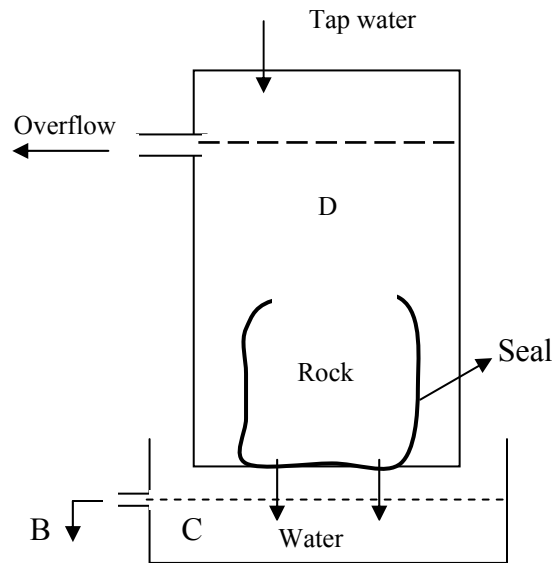


Figure 4.3 Flow experimental apparatus for sample B (denoted as “Rock” in the figure). The rock sample was sealed around the side with the top surface open for water flow through. Water was filled in the big pipe D up to the overflow level. Container C is used to collect effluent from the experiment. Effluent was collected from outlet B for flow rate measurements.

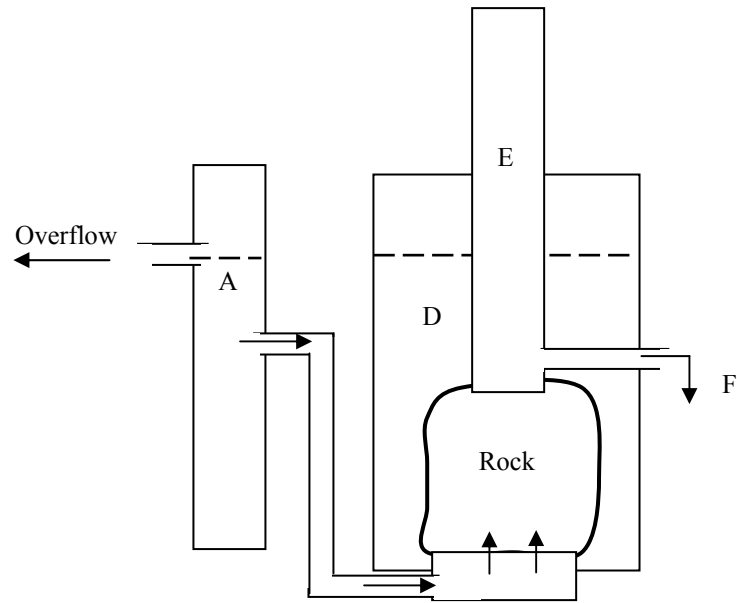


Figure 4.4 Flow experimental apparatus for sample B (denoted as “Rock” in the figure). The rock was sealed around the side; water head was built up in tube A; water level in the big pipe D was maintained to be not less than that in tube A. The effluent from outlet F was collected for flow rate measurements.

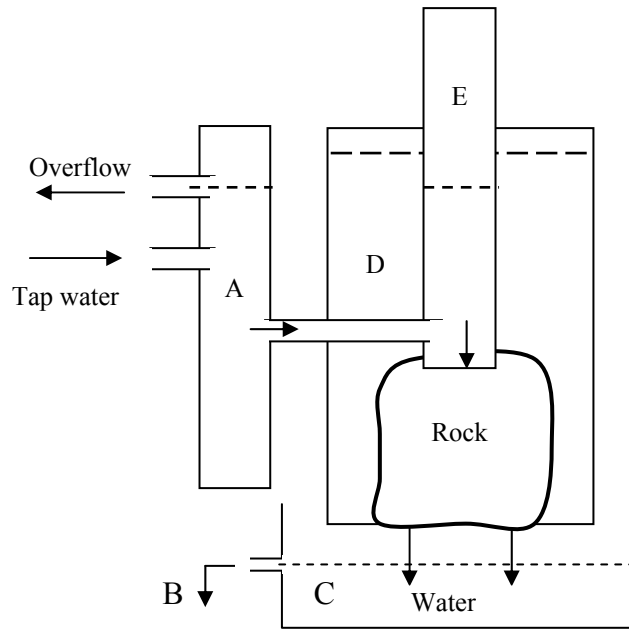


Figure 4.5 Flow experimental apparatus for sample B (denoted as “Rock” in the figure). The rock was sealed around the side. Tubes E and A are connected and the water head built up in tube E was controlled by adjusting the height of tube A. Water level in pipe D was maintained to be not less than that in tube E. Effluent coming out of outlet B was collected for flow rate measurements. Flow goes from the top to the bottom of the rock sample.



Figure 4.6 Rock sealed on a plastic disk, which has a hole in the center that allows water to flow through; the diameter of the hole is 23 cm.

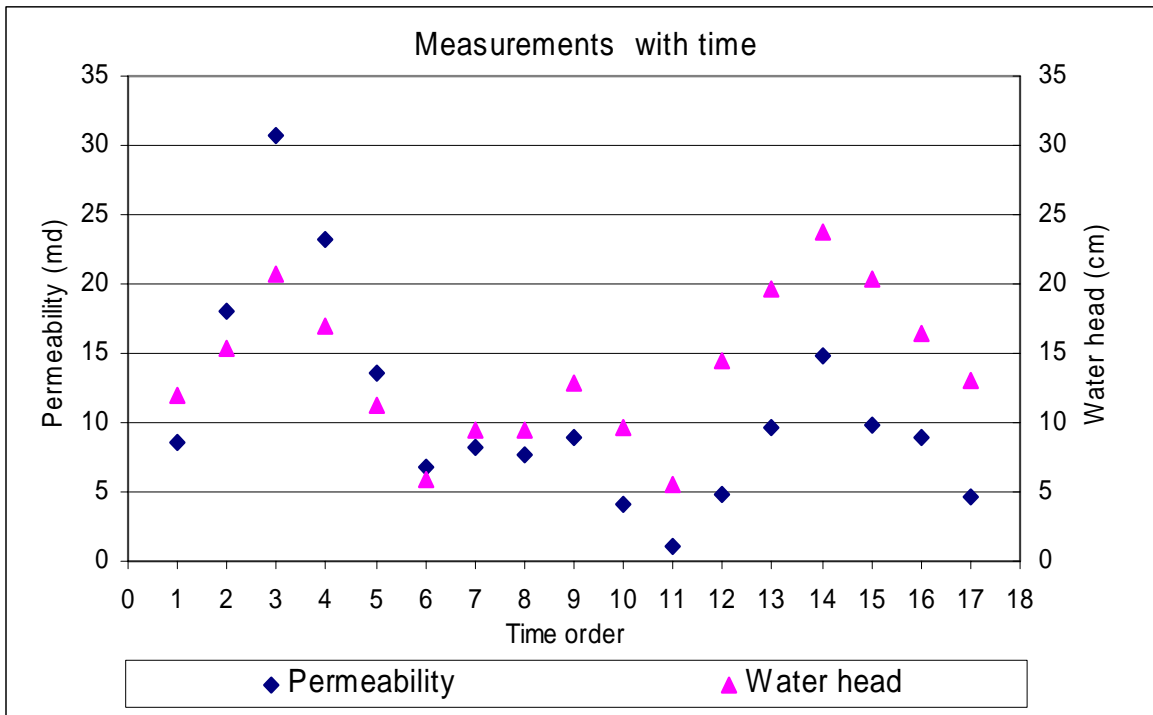


Figure 4.7 Flow experimental results of sample B. The plot shows the permeability measured changes with time. With the same water head, the permeability measured decreases with time.

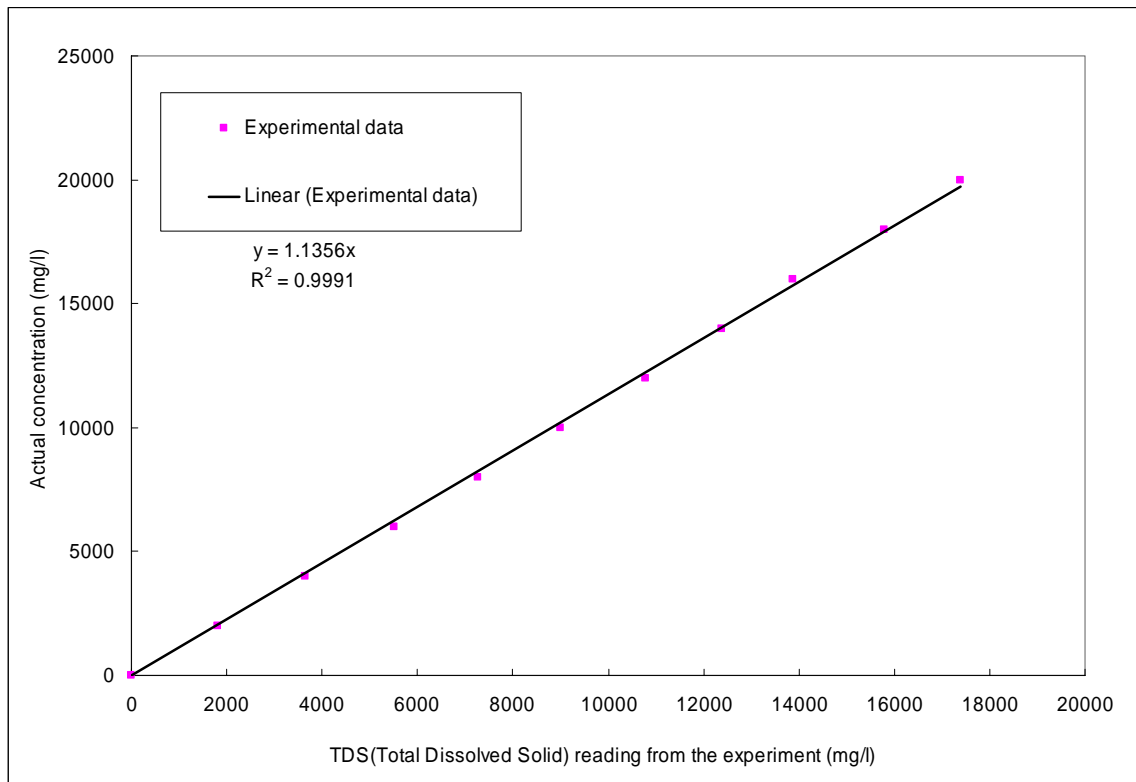


Figure 4.8 Conductivity meter calibration. The slope of the straight line (1.1356) is used in calibrating the TDS reading from the experiment into concentration.

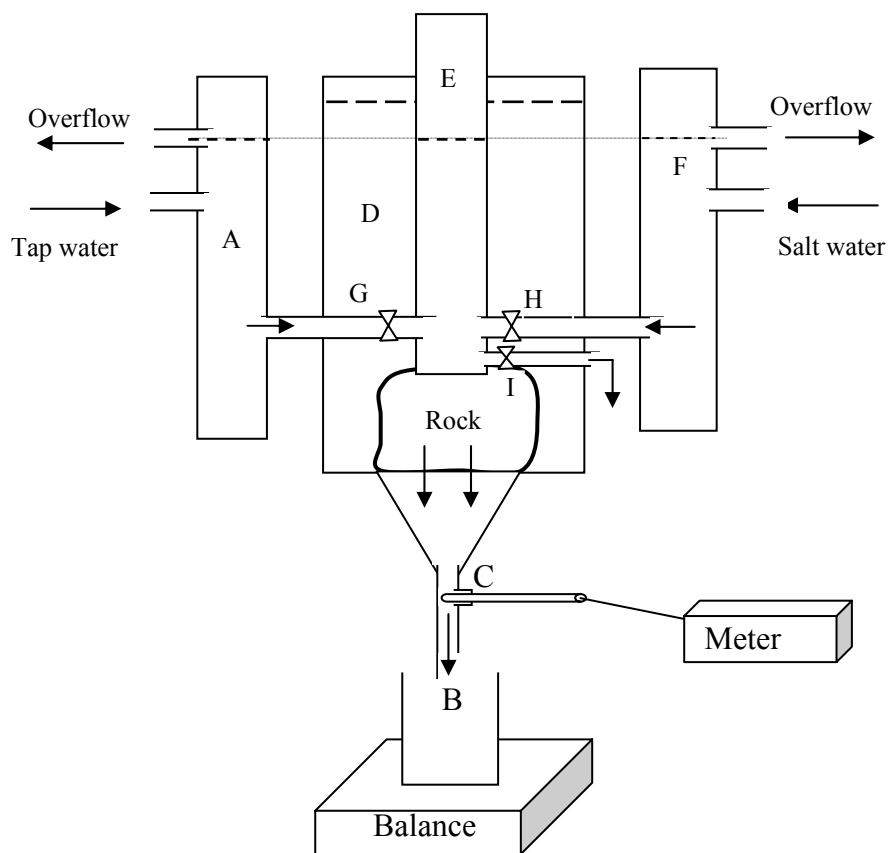


Figure 4.9 Tracer experimental apparatus for sample C, which was built based on the flow experiment apparatus shown in Fig. 4.5. Tube F was added for supplying salt water. Container B is used to collect effluent from the experiment. Port C in the outlet tube is used for placing the conductivity probe. Valves G and H are used to control the supply of either salt water or tap water and they can also control the flow rate. Valve I is used to drain out the fluid remaining on top of the rock sample.

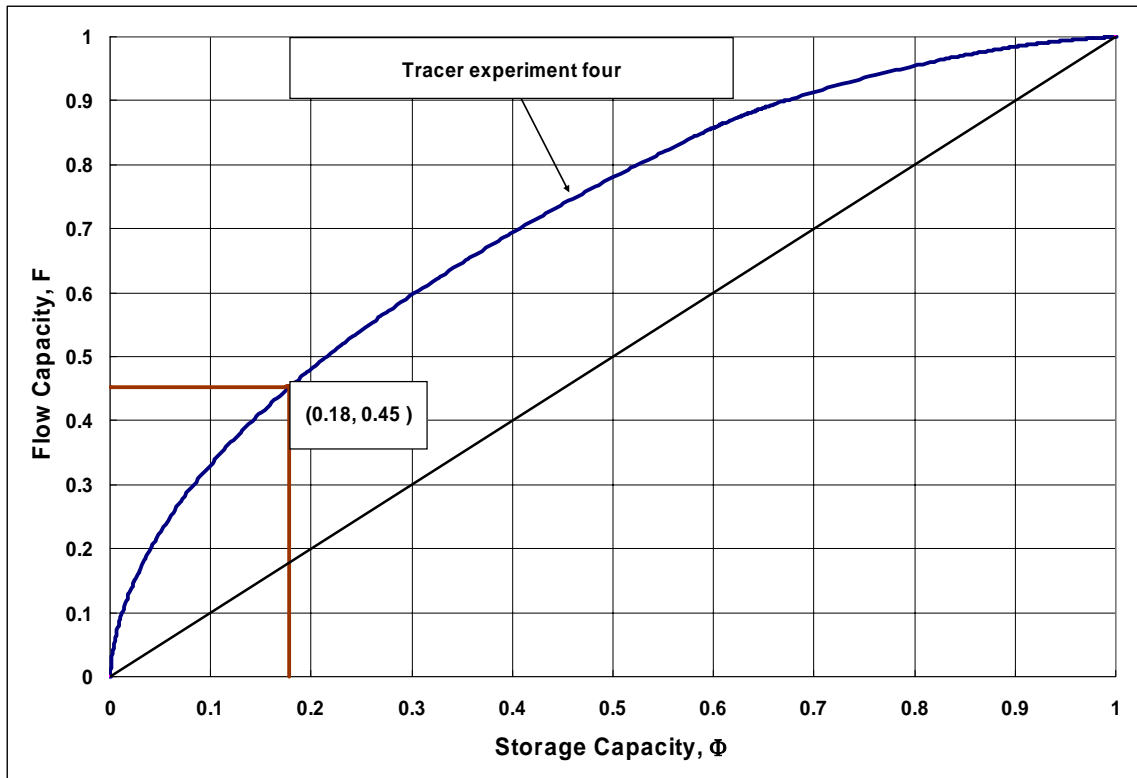


Figure 4.10 Flow capacity and storage capacity diagram for tracer transport experiment four (sample C). This plot was generated using Shook and Forsmann's method. The plot shows some 45% of the total flow coming out of 18% of the storage.

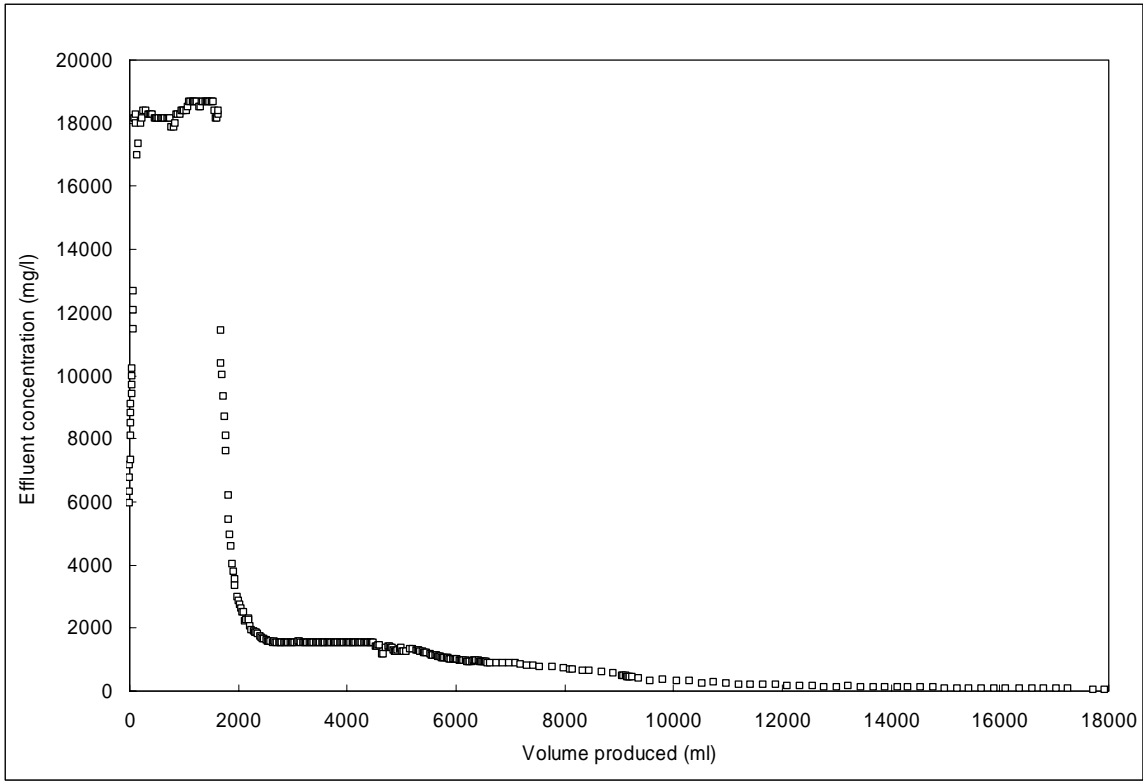


Figure 4.11 Effluent concentration history from experiment one. The injecting tracer concentration is 20,000 mg/l. The slug size is 1.6 pore volumes.

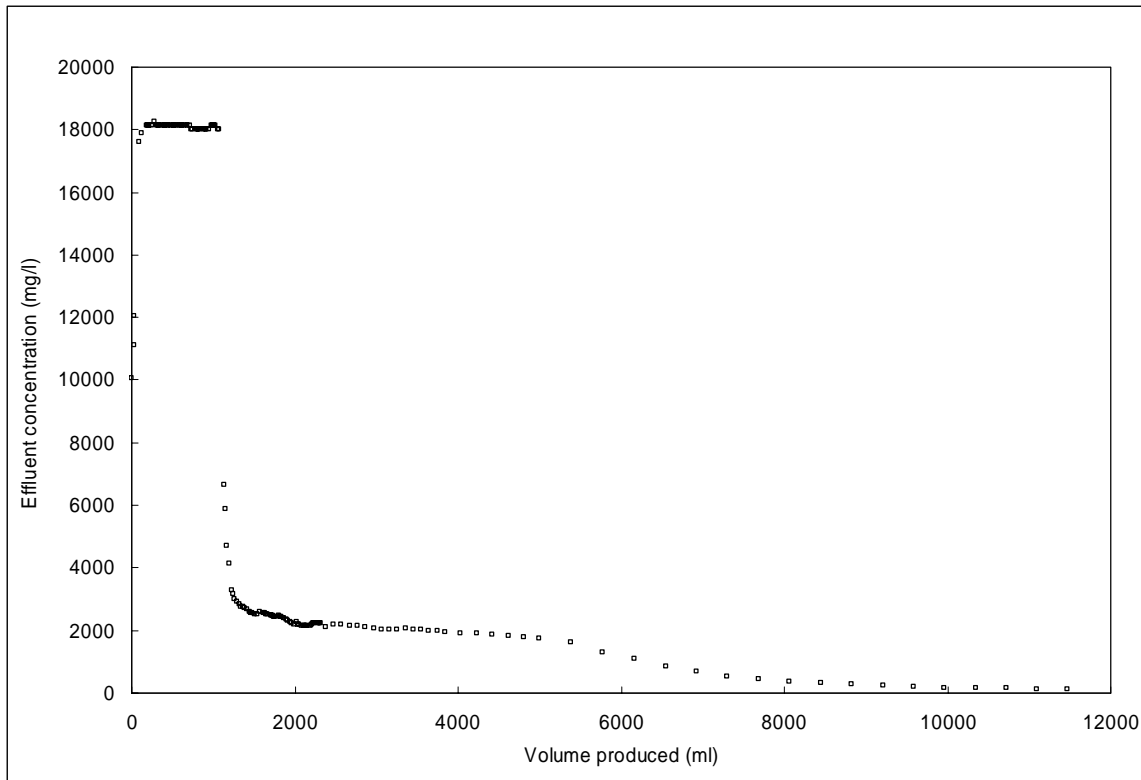


Figure 4.12 Effluent concentration history from experiment two. The injecting tracer concentration is 20,000 mg/l. The slug size is 0.7 pore volumes.

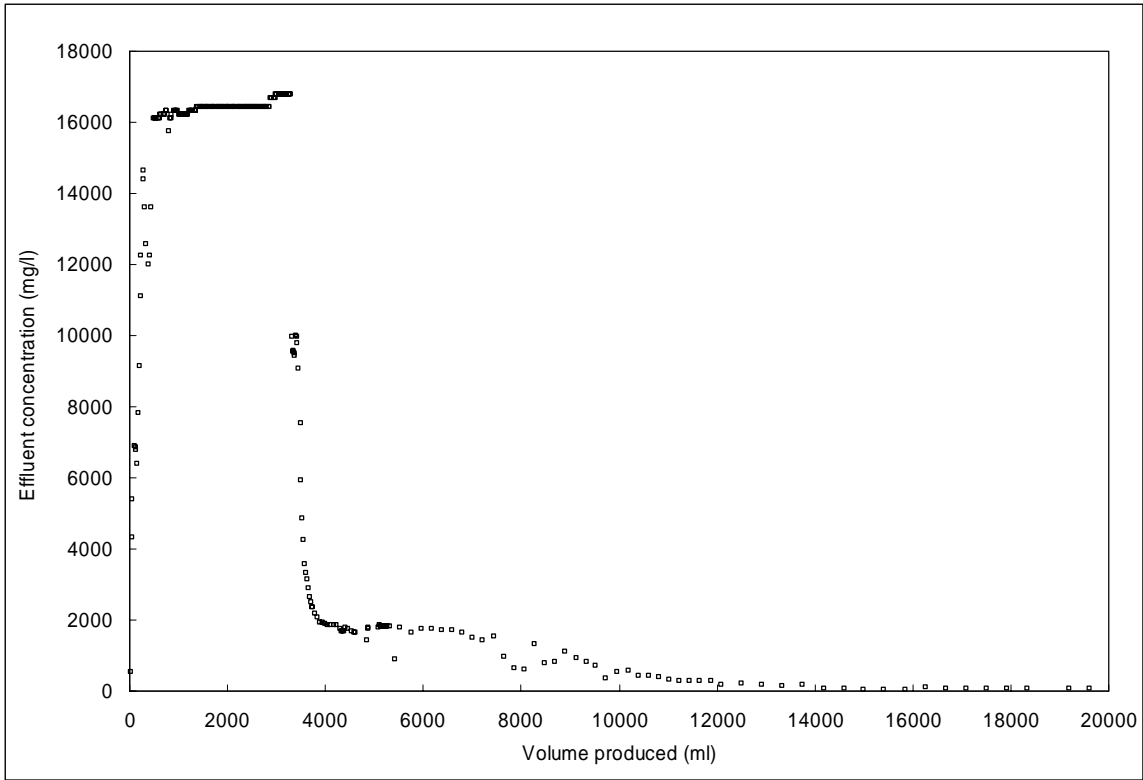


Figure 4.13 Effluent concentration history from experiment three. The injecting tracer concentration is 18,000 mg/l. The slug size is 3.4 pore volumes.

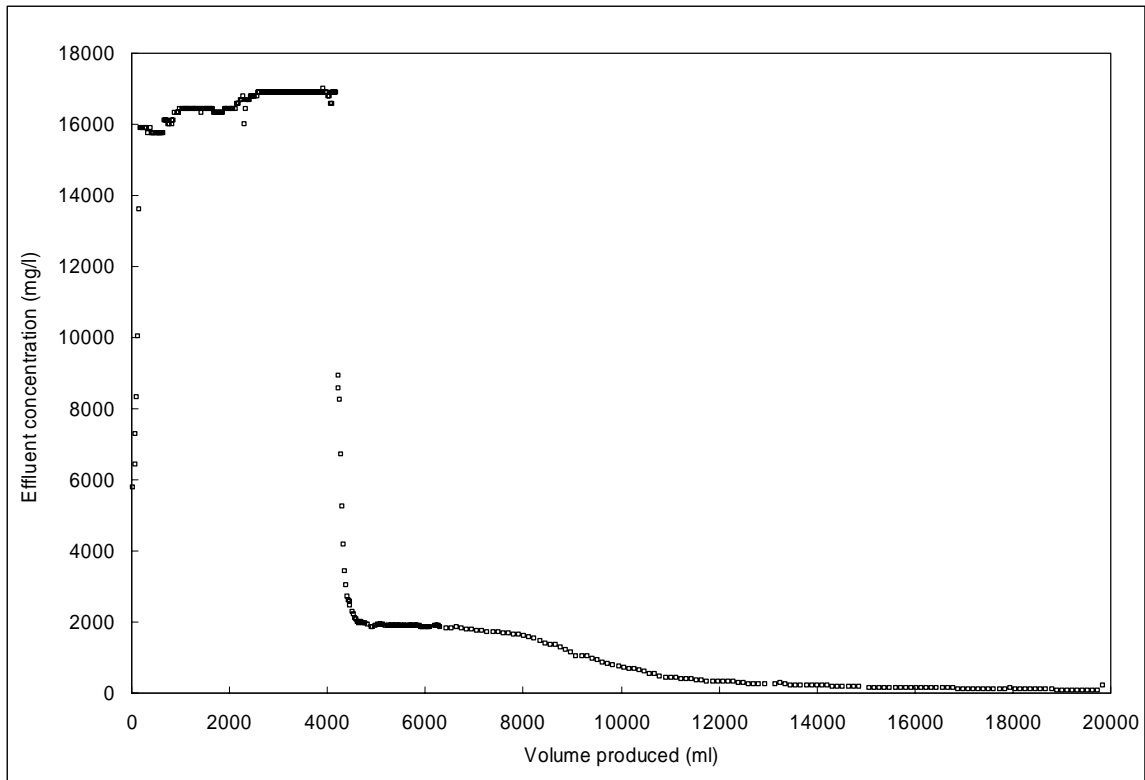


Figure 4.14 Effluent concentration history from experiment four. The injecting tracer concentration is 18,000 mg/l. The slug size is 4.1 pore volumes.

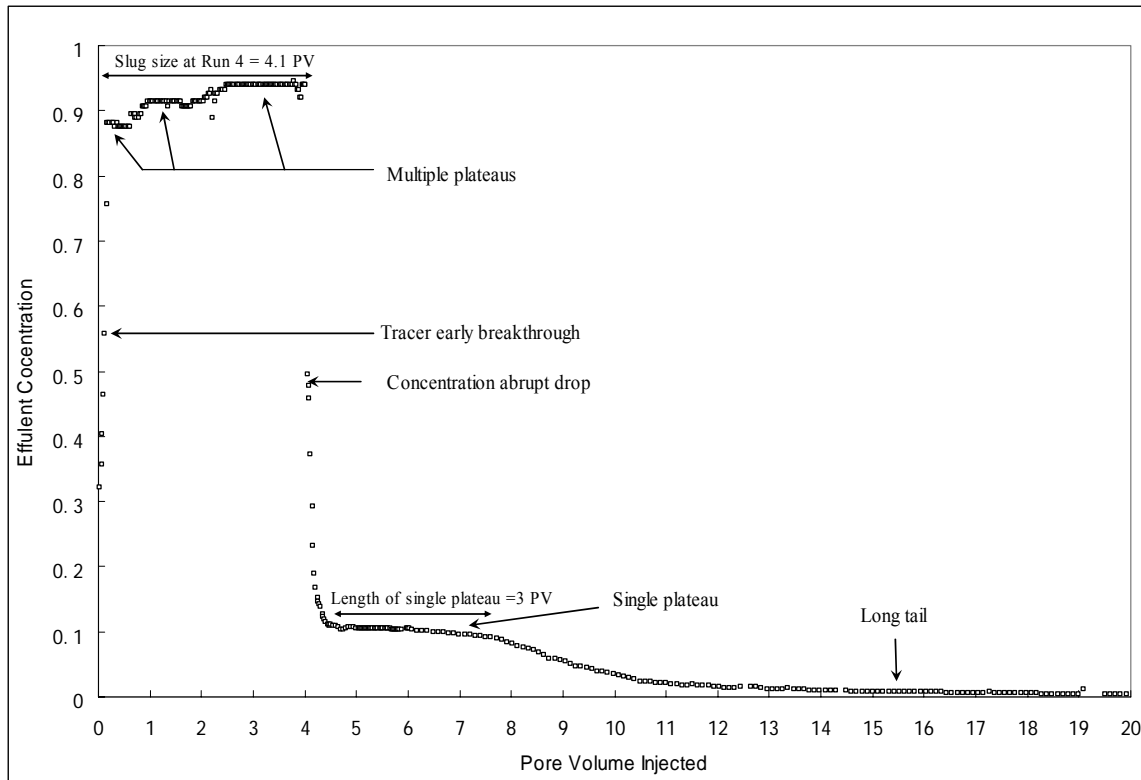


Figure 4.15 Effluent concentration history from experiment four in dimensionless forms. This figure labels five common characteristics, which are also observed in curves from the other three experiments. The dimensionless pore volume was normalized based on the CT scan pore volume of 1142 cm³ in sample C.

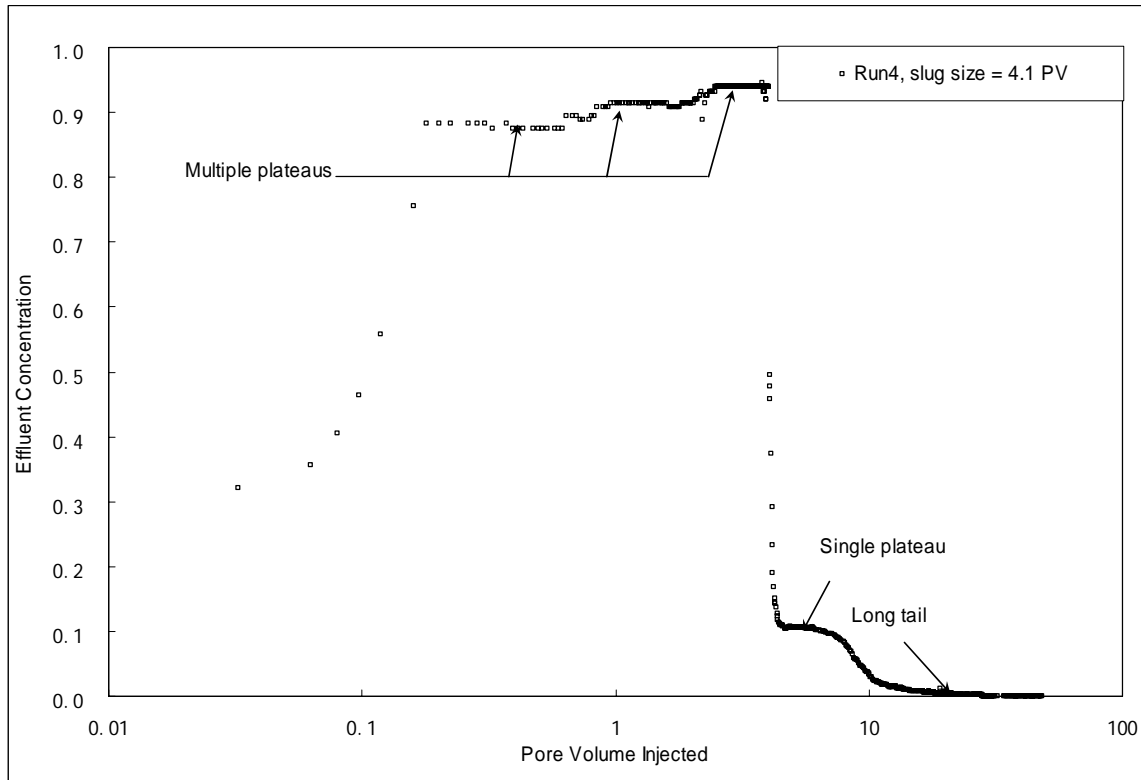


Figure 4.16 Effluent concentration history from experiment four. This figure emphasizes the tracer early breakthrough on a log plot.

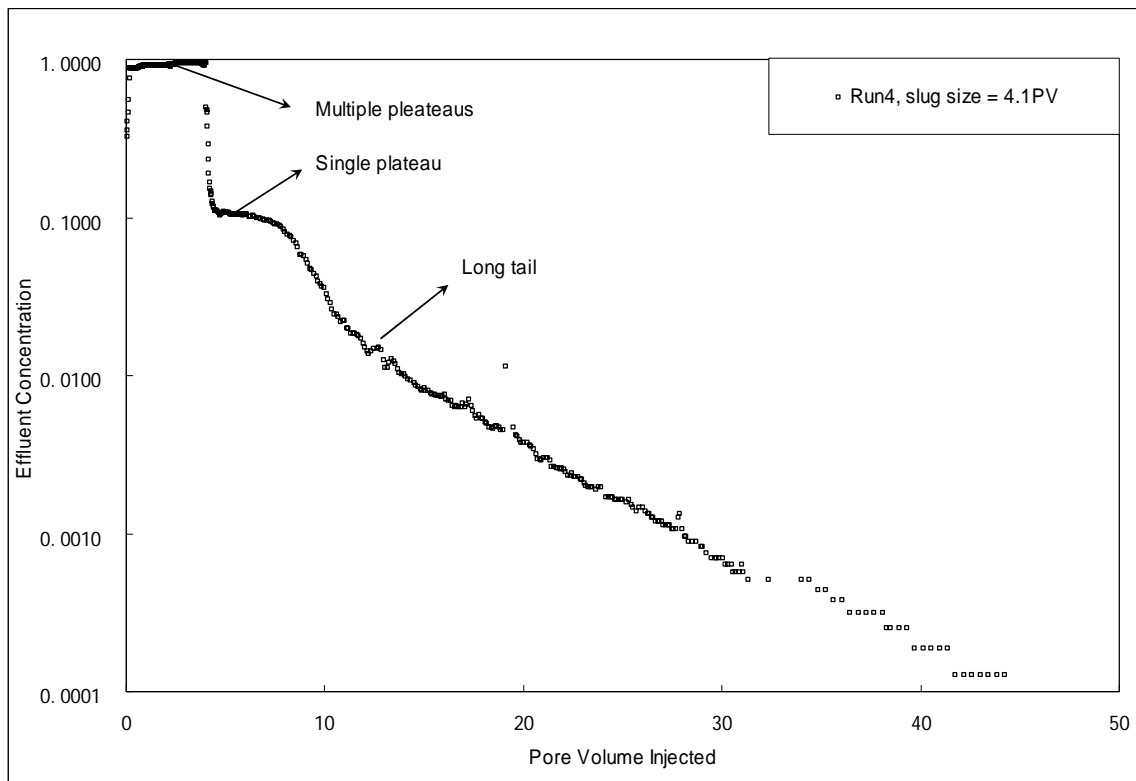


Figure 4.17 Effluent concentration history from experiment four. This figure emphasizes the long tail in the history plot.

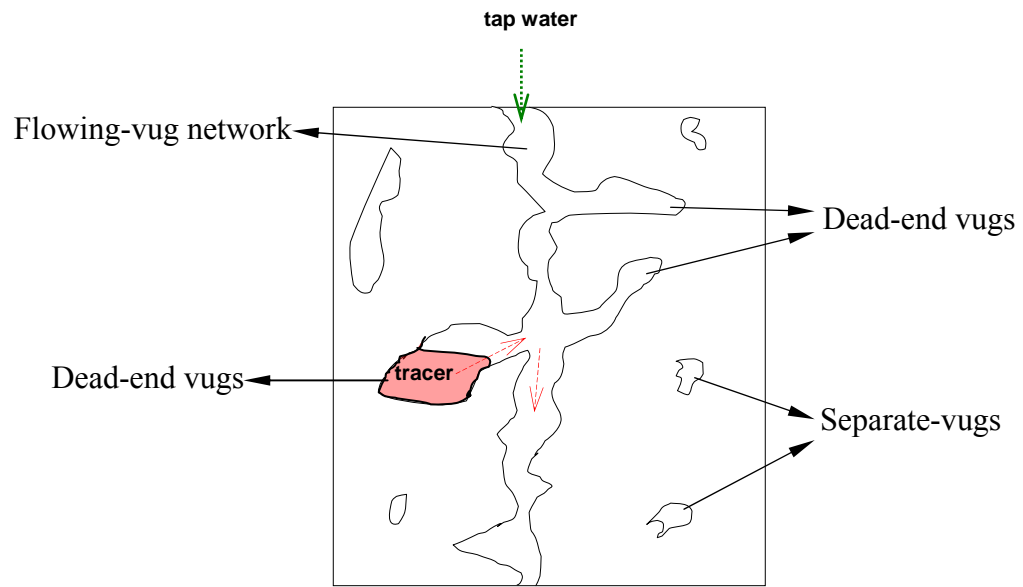


Figure 4.18 Tracer transferring from dead-end vugs into flow paths. The boundary condition is injecting tap water. Fine dashed arrows represent tap water, coarse dashed arrows represent tracer.

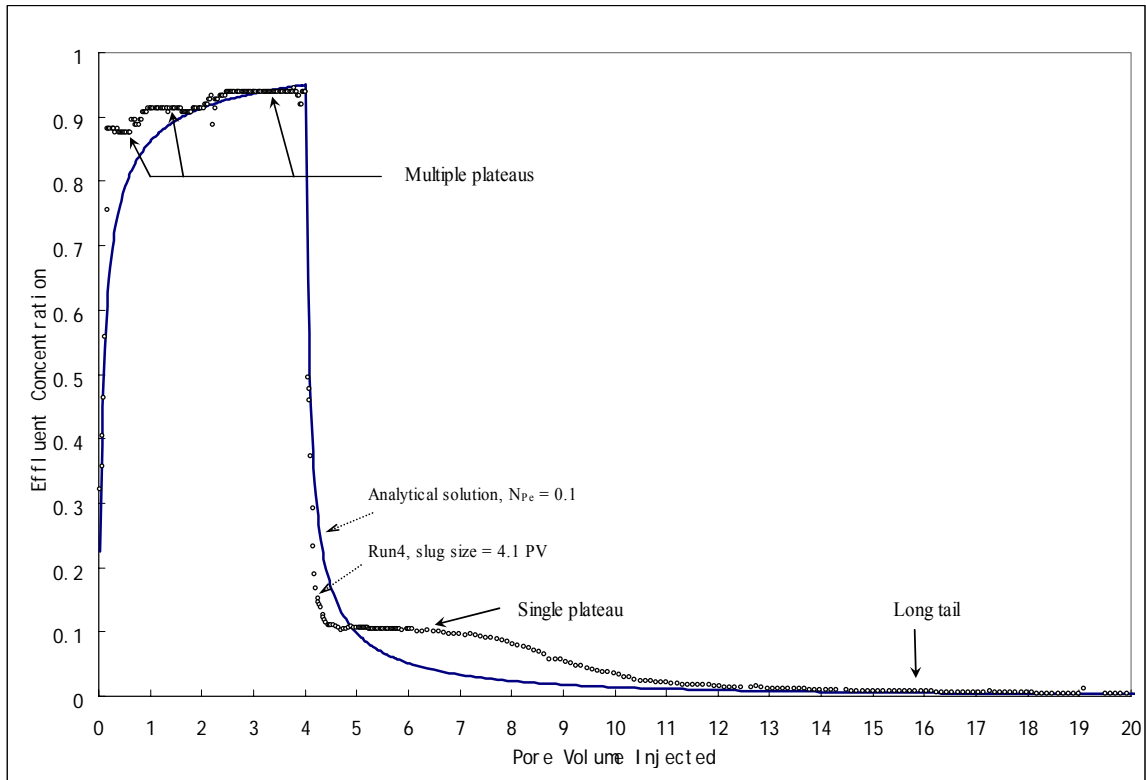


Figure 4.19 Effluent concentration histories from experiment four and 1D convection dispersion equation with Peclet number 0.1. The figure shows the analytical solution does match the experimental data poorly.

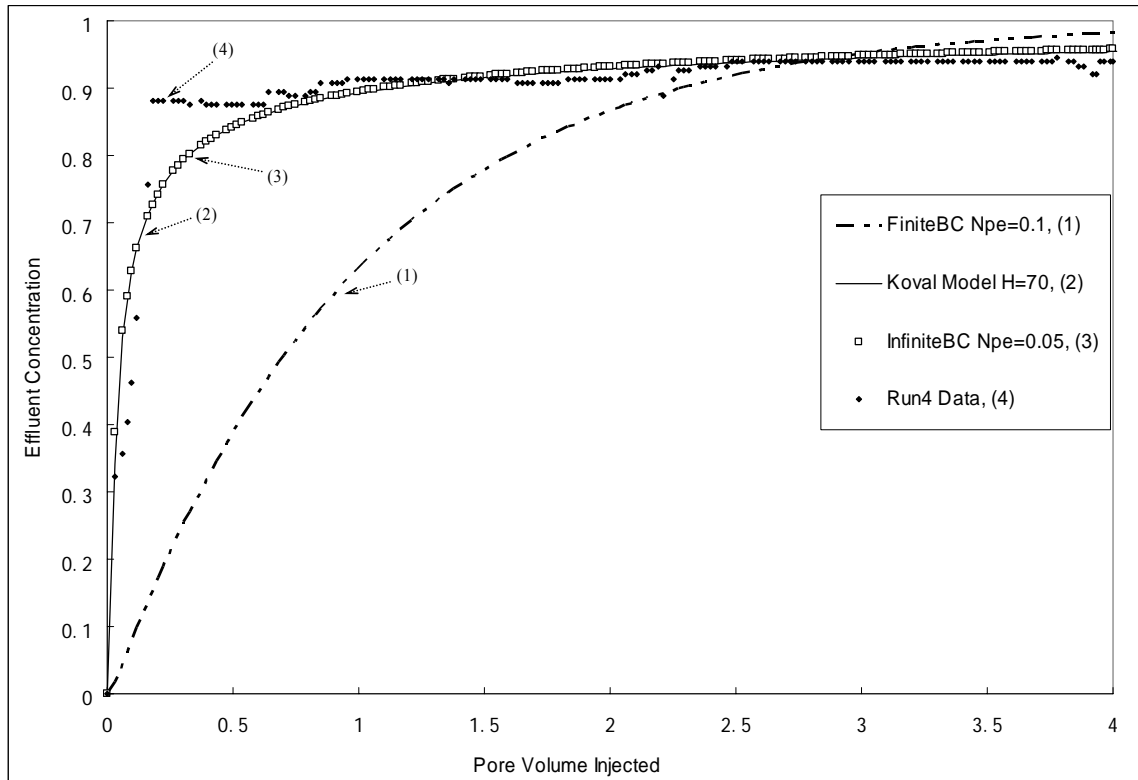


Figure 4.20 Model matching of effluent concentration history from experiment four. The concentration history from the experiment before the end of slug injection was modeled with three analytical solutions from 1D convection-dispersion model with both finite and infinite boundary conditions and Koval model.

NOMENCLATURE

C	Tracer concentration, [ML ⁻³]
C^*	Concentration in stagnant pores, dimensionless
D	Dispersion coefficient, [L ² T]
f	Fraction of the pore space occupied by mobile fluid, dimensionless
H	Heterogeneity factor
h	Water head above the top of sample, [L]
k_{avg}	Effective permeability of the combined system in flow experiment on sample A, [L ²]
K	Mass transfer coefficient between stagnant pores and flow channels, [T ⁻¹]
L	Length of the tested system, [L], in Equation 4.1
L	Length of the core / sample, [L], in Equation 4.2
R_1	Bucket inner radius at the mouth of the tested system, [L]
R_{out}	Outlet system radius (rubber ring radius), [L]
R	Radius of the plastic disk, where the sample open to the air, [L]
t	Time, [T]
t_D	Dimensionless time, $\frac{vt}{L}$
t_s	Duration of the injected tracer slug
\bar{V}	First temporal moment of tracer volume, [L ³]
V_s	Tracer slug volume, [L ³]
v	Average interstitial velocity, [LT ⁻¹]
V	Cumulative volume of fluid injected since the injection of tracer slug, [L ³]
x	Linear distance, [L]

Chapter 5 Theoretical Model Calculations

In the literature, one can find numerous models available on modeling porous media and physical properties of the rock and fluid. Among them, the most basic one is the bundle-of-capillary-tubes model, which is simple and can capture the pore size distribution of the modeled sample. Pore-network models are also frequently used and have been employed to simulate flow through carbonates (e.g. Xu et al., 1999, Cooper et al., 1999). Xu et al. (1999) successfully modeled the petrophysical properties of fluid flow through a heterogeneous carbonate sample. Ramakrishnan et al. (2001) modeled vuggy carbonates using an effective medium approximation of spheres submerged in a uniform field.

However, none of the carbonate samples in the above studies contains centimeter-scale vugs as our sample does. The large-scale heterogeneity makes it difficult to use any available complicated network model simulating flow and transport through the sample. A bundle-of-capillary-tubes model, on the other hand, is simple to use and is useful to capture the important features displayed in our sample. This chapter explains the bundle-of-capillary-tube modeling of flow and transport through sample A and sample C. The capillary tubes in the bundle-of-capillary-tubes model are imagined as the connected vugs. The matrix in the rock samples is modeled as an impermeable medium.

5.1 THEORETICAL MODEL CALCULATIONS ON SAMPLE A

Sample A was modeled as a bundle-of-capillary-tubes; the flow experiment three (see Table 4.1) was simulated. The hydraulic head, the dimension of the combined porous

system, and the flow rate in this experiment were considered in the modeling. The bucket in the experiment was assumed to be cylindrical (Figure 5.2). As shown in Figure 5.1, the matrix in sample A was assumed to have zero permeability; the connected vugs were assumed as identical capillary tubes of a single diameter through the entire length. The following two sections explain the modeling of flow through sample A with laminar and turbulent flow assumptions respectively.

5.1.1 Model Calculations Assuming Laminar Flow through Connected Vugs

With the assumption of laminar flow through capillary tubes in the model, the effective permeability of the modeled sample was calculated using Hagen-Poiseuille's Law and Darcy's Law. For a straight tube with a radius r , its equivalent permeability is calculated using Eq. 5.1. For many straight tubes with the same radius r , the permeability of the bundle-of-tubes with porosity ϕ is calculated from Eq. 5.2.

$$k = \frac{r^2}{8} \quad (5.1)$$

$$k = \frac{\phi r^2}{8} \quad (5.2)$$

Opposite to the process of calculating permeability from the experiment measurement, the permeability of the modeled sample was first calculated and the effective permeability of the combined system was then estimated. The model permeability was calculated as a function of capillary radius using Eq. 5.2. Taking the model permeability as the permeability of sample A, the average permeability of the

combined system (Figure 5.2) was estimated. This value is called model-average permeability in this section. The results are shown in Figure 5.3.

The plot in Figure 5.3 shows the model-average permeability versus the capillary tube radius for different numbers of capillary tubes. The experimentally determined average permeability (124 Darcy) of the combined system and of the sand (135 Darcy) are also plotted. The model-average permeability of the combined system with no tubes in the model is about 68 Darcy, which is the permeability of the system with an impermeable rock surrounded with 135 Darcy sand. With one or more tubes in the model, the model-average permeability of the combined system becomes a constant of about 210 Darcy when the capillary tube radius is large enough. This means the apparent permeability of the combined system is constrained by the sand with the relatively smaller permeability when the permeability of the capillary tubes is larger than 135 Darcy.

The key feature of this plot is the intersections of the experimental permeability with the model-average permeability. For example, the meeting point of the experimental permeability with the single tube model-average permeability corresponds to a capillary tube radius of nearly 2,000 microns. It means that the average permeability of 124 Darcy for the combined system could be produced by a single capillary tube of radius 2,000 microns. However, the largest vug size seen on the top of the small sample is on the order of 1 cm in radius. A capillary tube model of this size would give a much larger average permeability than 124 Darcy. This suggests that the large channel visible at the surface must become narrow inside the rock. Thus the vugs in sample A must be connected by relatively narrow channels.

5.1.2 Model Calculations Assuming Turbulent Flow through Connected Vugs

Because large size vugs were seen on the surface of sample A, it was suspected that flow through large vugs in the sample might be turbulent. Therefore, modeling of flow through sample A with the bundle-of-capillary-tubes model was also performed with the assumption that the flow through connected vugs (capillary tubes in the model) is turbulent. Similarly to the permeability calculation procedure for laminar flow assumption, the effective permeability of the combined system was calculated with the turbulent flow assumption. With this assumption, the combined system in Figure 5.2 was divided into two parallel sub-systems. The sand around the annulus in the bucket throughout the entire combined system was considered as the first sub-system. The rest of the combined system is the rock and the sand under the rock, which was considered as the second sub-system. The flow through the first sub-system was assumed as laminar because there was only sand in it.

A detailed derivation of the effective permeability of the combined system for this turbulent flow assumption is shown in Appendix B. The general procedure is briefly introduced as follows. The flow rate going through the modeled sample (bundle-of-capillary-tubes) was first calculated; the potential drop over the sample was then estimated. At this step, the relative roughness of the tubes (connected vugs) in the model was assumed as 0.015, which is for a tube with a material of stave wood type with a diameter of less than 1 inches (2.54 cm) (Moody, 1944). The friction factor was obtained using the chart, Figure 1 in Moody's paper, when Reynolds number is greater than 2,000. When Reynolds number is less than 2,000, the flow becomes laminar; thus the friction factor is calculated from formula 5.3. For turbulent flow through a sand pack or a real porous medium, the Reynolds number should be much smaller than 2000. However, in

this calculation, only flow through connected vugs was modeled, therefore, the Reynolds number for tube/pipe flow of 2,000 is appropriate.

$$f = \frac{64}{\text{Re}} \quad (5.3)$$

where f is the friction factor,

Re is the Reynolds number.

The rock permeability and the effective permeability of the combined system were then calculated. The plots of the effective permeability with tube radius were shown in Figure 5.4, in which the effective permeability calculated from the laminar flow assumption was also plotted.

As can be seen in Figure 5.4, the plots calculated from turbulent flow assumption agree well with that calculated from the laminar flow assumption except when the tube number is one. In this case, the intersection of the effective permeability of 124 Darcy with the model-average permeability gives a radius of around 2,500 microns. This means that the permeability of 124 Darcy is equivalent to a single tube of 5 mm in diameter with the turbulent flow assumption. However, the diameter of 5 mm is still too small compared to the size seen on the top surface of the rock. Therefore, the same conclusion as that from laminar flow calculation was obtained that the largest channel visible at the rock surface must narrow down through the sample.

5.2 THEORETICAL MODEL CALCULATIONS ON SAMPLE C

The tracer transport through sample C was also modeled using the bundle-of-capillary-tubes model. The objective of this calculation was to estimate the size and

volume of the fast path that caused significant preferential flow in the transport experiment. Transport experiment four was simulated by setting up the same water head in the model calculation (pressure drop 0.4 psi). The pore volume (1142 cm³, section 2.4.1), and permeability (6 Darcy) of sample C, the flow rate (7 cm³/s), breakthrough time (9 seconds, section 4.2.5) and the volume of the preferential flow path of 30 cm³ (section 4.2.5) were matched to the experiment data by adjusting the diameter and the number of the capillary tubes. Step-input type of salt water injection instead of slug injection was modeled.

The connected vugs in sample C were first approximated as a simple bundle of capillary tubes with different diameters, but with each tube having a constant diameter (Fig. 5.5, Model II). Larger tube diameters produce higher rates and quicker tracer breakthroughs even though they have larger volumes. Thus, the tracer breakthrough time in experiment four was matched by the breakthrough time from the largest tube in the model, and the fast path volume was the total volume of all the tubes of that size. The porosity and permeability of the model was produced by the combined effect of all the capillary tubes. The modeling results showed that to match the 9 second breakthrough time, the diameter of the largest tube must be around 120 microns. So to get a fast path volume of 30 cm³, there must be about 300,000 such tubes. However, the corresponding flow rate of this model was around 50 cm³/s, which was much higher than the measured result of 7 cm³/s. It is not possible to simultaneously match the breakthrough time, fast path volume, total pore volume, and effective permeability with this simple, uniform-diameter capillary tube model. This is consistent with our previous conclusion that the vugs in the sample are connected by narrow throats.

A more complicated capillary-tube model with non-uniform diameters was then used to simulate the experiment (Fig. 5.5, Model III). In this model, each tube was

assumed to contain three sections with two different diameters. Ten types of these segmented tubes were used in the model, each with a different set of narrow and wide diameters. The narrow sections of the tubes were used to model the narrow throats in the connected vug network. The experiment and rock parameters were matched by trial and error. The number of each of these ten tubes and their section diameters are shown in Table 5.1.

It was found that this more complicated model could simulate the experimental concentration history during slug injection much better because it includes tubes with narrow constrictions (Figure 5.6). Figure 5.6 shows that the modeling result seems to match that of the experiment. The modeled results of the experiment and rock parameters are shown in Table 5.2. It shows that the largest error in the table is 7.6%, which is from the pore volume calculation. This error was acceptable in the modeling because it is not significant, and the objective of the modeling was not for exact parameters matching but to get a rough estimation of the narrow throat size.

The early breakthrough time (9 s) and fast path volume (30 cm^3) was simulated by the two largest identical tubes in the model (Fig. 5.7). These two tubes were those with both the largest volume and the largest throat size. They accounted for 45% of the total flow through the model, but only 3% of the total porosity. Although this shows more heterogeneity than that observed from the flow versus storage capacity diagram, 45% of the flow comes from 18% of the porosity, both of them indicate a highly heterogeneous pore system with highly preferential flow paths in sample C. The diameter of these largest throats, 1 mm, is consistent with our previous conclusion that the vugs in the sample must be connected by throats with a diameter less than 4 mm. The large diameter (2 cm) section contributes mostly to the large volume of the preferential flow path (30 cm^3) but contributes very little to the flow rate ($7 \text{ cm}^3/\text{s}$) because flow is constrained by

the small size (1 mm) in one section. This explains why constant diameter tubes (Model II) could not model the transport through the sample. The largest section diameter of 2 cm was modeled because this is the visible size of vugs on the surface of sample C. Numerous other smaller tubes (Table 5.1) contribute mostly to the porosity and little to the flow rate.

Although these quantitative analysis results are not unique, they indicate some important features of the rock sample such as the structure of the tube. As seen in Table 5.1, the largest tube size is in a unit of centimeter; whereas the smallest tube size is in a unit of micron. This demonstrates that the rock has a wide range of heterogeneity scales.

5.3 SUMMARY

The mathematical model calculation shows the following:

- Vugs in the vuggy sample are interconnected with narrow constrictions that are less than a few millimeters.
- The fast path in sample C is equivalent to two of the identical capillary tubes with different diameters as shown in Figure 5.7. The large volume of the fast path can be explained by large diameter (2 cm) sections in the largest tubes.
- Both the capillary-tubes model and the flow-storage diagram in Chapter four suggest that most of the flow comes from a small fraction of the total pore volume.
- Although the capillary tube model cannot quantitatively describe the flow and transport through this vuggy carbonate, it can qualitatively give information about the connection of the vugs within the sample.

Table 5.1 Table of size and number of tubes in the capillary-tube model III. Sample C was modeled by 10 types of capillary tubes. Each type tube contains three sections of two diameters with the total length of these sections to be the length of sample C. The number of tubes is summarized for each tube type in this table. A few of such tubes in Model III are shown in Fig. 5.5.

		Section 1	Section 2	Section 3
Length (cm)		2.5	5	2.5
Tube type	Number of tubes	Radius (micron)		
1	2	10000	500	10000
2	18	5000	300	5000
3	40	1000	100	1000
4	5000	200	40	200
5	80000	100	20	100
6	800000	50	10	50
7	8000000	10	5	10
8	20000000	5	4	5
9	200000000	1	0.5	1
10	2000000000	0.5	0.1	0.5

Table 5.2 Comparison of results from capillary-tube model with those from experiment four. In the column labeled “Experiment four”, the pore volume of sample C was from the CT scan; other parameters were from experiment four.

	Experiment four	Model	Error(%)
Permeability (d)	6.2	6.6	6.45
Flow rate (cm ³ /s)	7.1	7.6	7.04
Breakthrough time (s)	9	9	0.00
First fast path volume (cm ³)	30	31	3.33
Pore volume (cm ³)	1142 (CT)	1055	-7.62

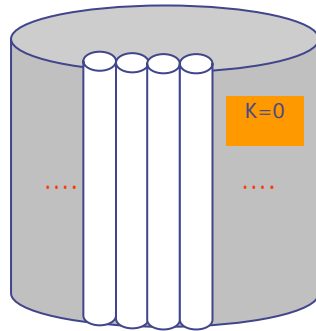


Figure 5.1 Bundle-of-capillary-tubes model I. This model contains identical capillary tubes of a single diameter through the entire section.

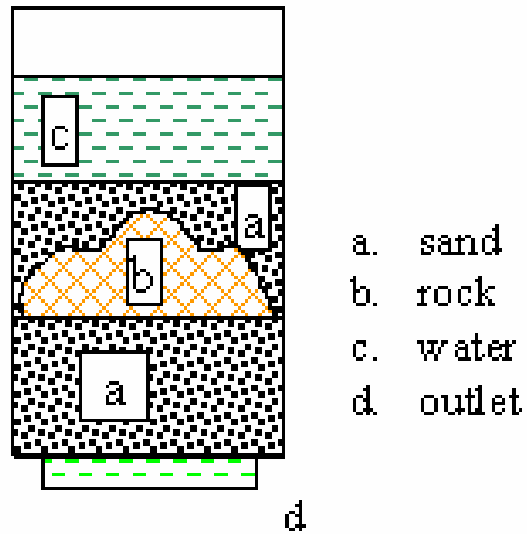


Figure 5.2 Illustration of experimental setup for flow through sample A.

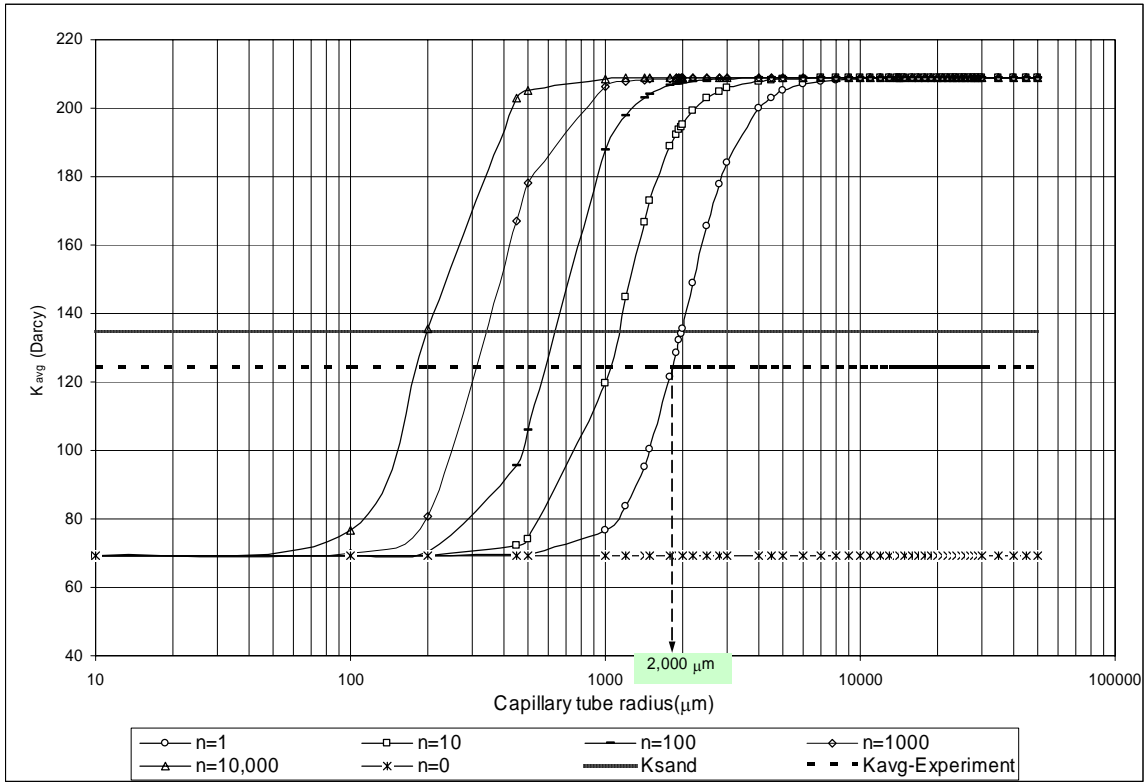


Figure 5.3 Average permeability of the combined system vs. tube radius for laminar flow assumption. In the figure labels, n means the number of the capillary tubes. This figure gives the effective permeability of the combined system for different number of capillary tubes n . The sand permeability is 135 Darcy and the effective permeability is 124 Darcy for the combined system measured from experiment three. The arrow in the figure points to a tube radius of nearly 2,000 microns, which shows the tube radius that corresponds to the intersection of the permeability from the model with $n = 1$ and that from the experiment.

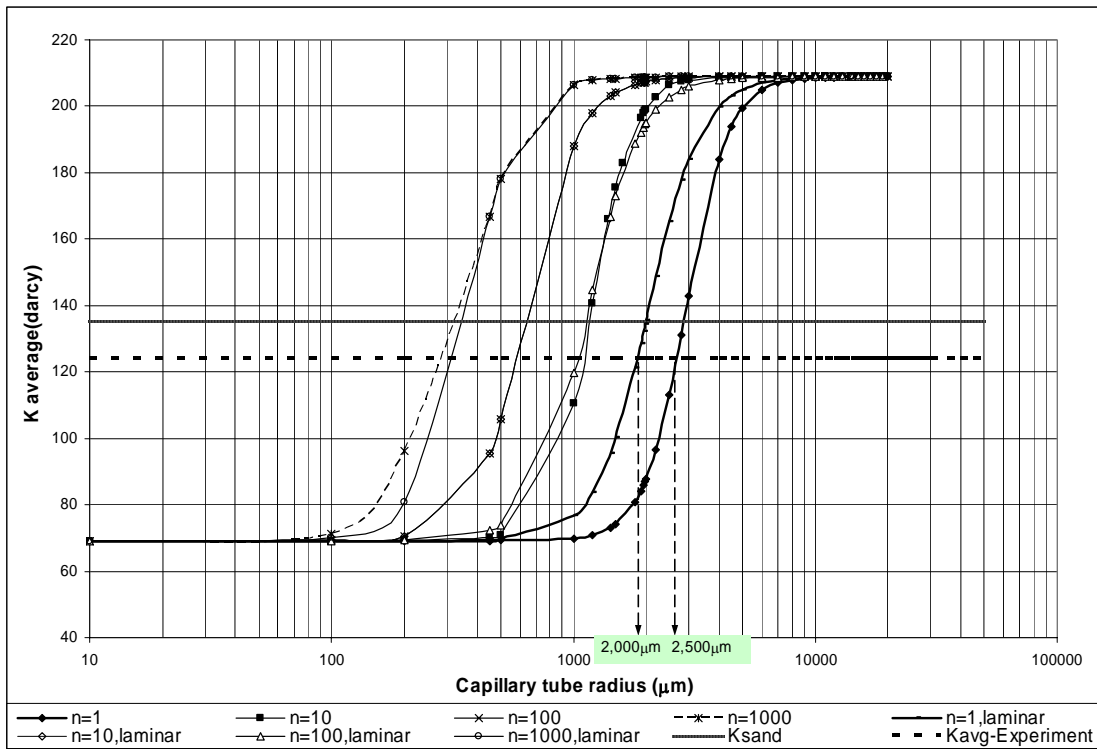


Figure 5.4 Average permeability of the combined system vs. tube radius for turbulent flow assumption. In the figure labels, n means the number of the capillary tubes. This figure conveys similar information as that of Fig. 5.3 except this shows the result of turbulent flow assumption in tubes.

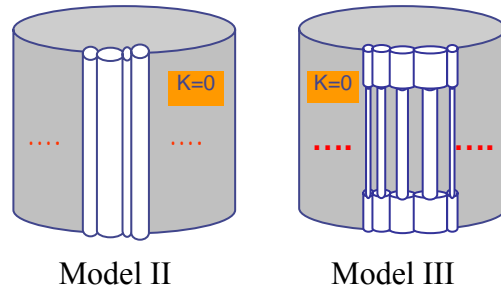


Figure 5.5 Bundle-of-capillary-tubes model used for modeling sample C. Model II contains different tubes of constant diameters. Model III contains different tubes with each having three sections of two different diameters.

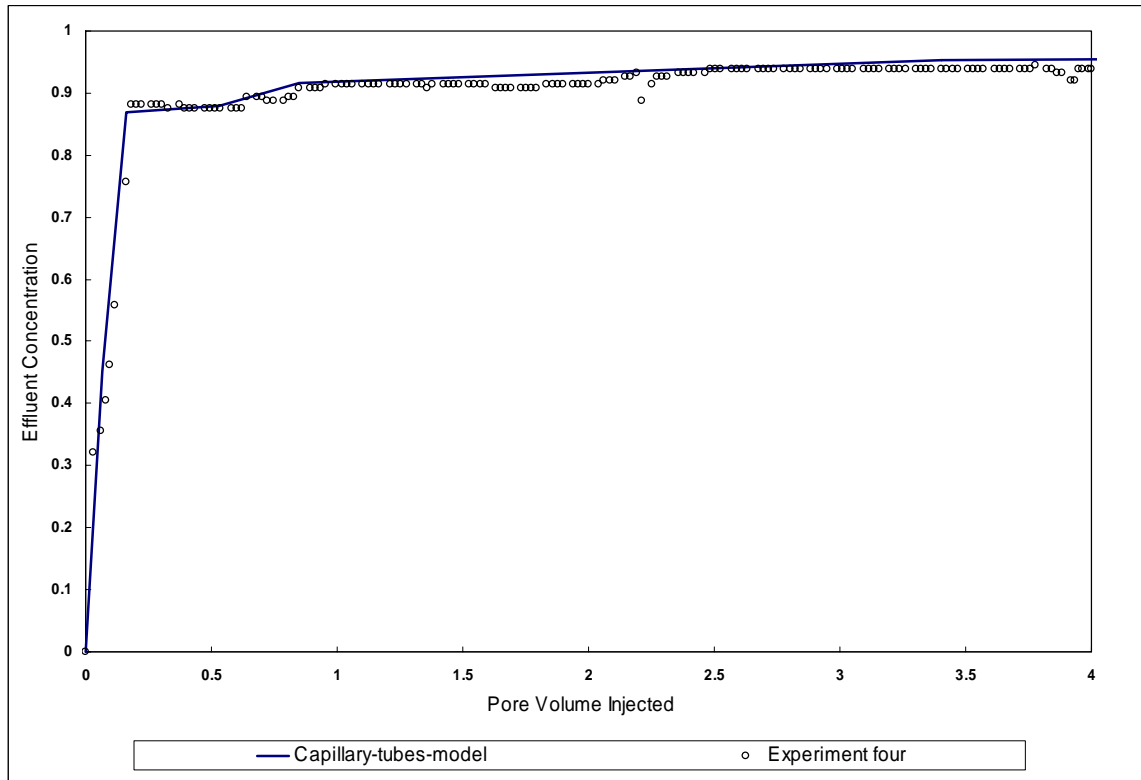


Figure 5.6 The effluent concentration profile estimated from capillary tube model III with tube radius and section length shown in Table 5.1. The effluent concentration history from experiment four was also plotted and it showed a good match with the model result.

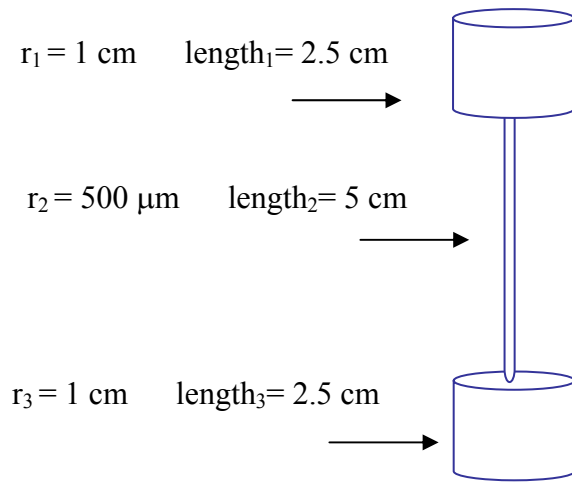


Figure 5.7 Sketch of the largest capillary tube in model III. The constraint of this tube is of size 1 mm in diameter.

NOMENCLATURE

f	Friction factor
k	Permeability of the bundle-of-tubes, [L ²]
r	Radius of a straight tube, [L]
Re	Reynolds number
ϕ	Porosity

Chapter 6 Flow and Transport Simulations on Computational Sub-sample

This chapter introduces the software and the computational machines used in numerical simulations on the computational sub-sample. Initial conditions, boundary conditions, and some input parameters are explained. The flow simulation section describes the permeability assignment and the permeability upscaling method. The transport simulation section discusses the study on tracer dispersion in the vuggy carbonate sample. The objective of performing these simulations is to investigate the connectivity of the vugs in the computational sub-sample and to understand the transport properties of the rock. Flow and transport simulations on a touching-vug network, characterized from CT (Computed Tomography) scan data, are presented. This is to understand the contribution of the touching-vug network to flow and transport through vuggy samples.

6.1 NUMERICAL SIMULATOR AND MACHINES

6.1.1 Parallel Subsurface Simulator (Parssim)

A simulator called Parssim (Parallel Subsurface Simulator) was used to conduct flow and transport simulations. Parssim was developed by the Center for Subsurface Modeling (CSM) in The Institute for Computation Engineering and Science (ICES) at The University of Texas at Austin. Parssim is a simulator for single phase flow and reactive transport of incompressible fluids through a heterogeneous porous medium. This simulator is also capable of simulating the decay of radioactive tracers or contaminants in

the subsurface, linear adsorption, wells and leaking sources, and bioremediation. It can be used as an aquifer or reservoir simulator. The detailed Parssim user manual (Arbogast, 2000), the source code and the sample input file are available at <http://www.ices.utexas.edu/~arbogast/parssim/>. The following is a brief introduction of the simulator from the user manual.

Parssim uses a rectangular data structure to define the subsurface domain. The domain can have a regular or irregular geometry. An irregular subsurface domain can be mapped to a rectangular, computational domain without loss of accuracy or efficiency using a mapping technique. Parssim allows writing output files in the format that can be visualized using *Eye* or *Tecplot*, which are plot and visualization software for 2-Dimensional and 3-Dimensional data.

Parssim can run in serial on a single processor, or on a parallel and distributed memory computer using Message Passing Interface (MPI). For parallel computation, the grid is divided into sub-domains that contain almost the same number of cells; each sub-domain runs only on one parallel processor. During the computation, the information is communicated among the processors.

Parssim consists of four main parts: driver, flow, transport, and chemistry. The flow and transport are the only two packages used in this research. The driver routines manage the user interface and the coupling of flow and transport routines. The flow routine, Parcel, uses a locally conservative, cell-centered finite difference scheme. The transport routine, ParTrans, uses a locally conservative method of Characteristic-Mixed Finite Element Method (CMM) or a Godunov Method (Arbogast, 2000). The higher order Godunov Method (HOG) was used in our simulations.

The current version of Parssim (v. 2.1) uses Darcy flow in both vug and matrix cells. Since the vugs might be too large to be safely described by Darcy's law, Navier-

Stokes law has been considered to compute flow in vugs. A mixed finite element method for the coupled Darcy and Stokes flow problem has recently been developed (Arbogast and Brunson). For a large-scale medium, a macroscopic model-Darcy's flow was derived from the Darcy and Stokes coupled micro-scale model (Arbogast and Lehr). They found that the equivalent permeability obtained for the macro scale media collected both the vug and the matrix information. Effort will be made in the future to use the Darcy and Stokes coupled model to compute the effective permeability and to understand the transport properties of the vuggy system. However, for this research, Darcy flow simulation will give useful information for this extremely complex system. We assigned vug cells a large permeability to simulate flow in vugs using Darcy's law.

6.1.2 Machines

Two clusters in CSM have been used for simulation. Longhorn was mostly used for flow simulations and Bevo was used for transport simulations. Constructed in 1998, Longhorn has 64 Pentium II 400MHz computers with 256MB of SDRAM connected by both a 100Mbit ethernet network and a Myrinet LANai 4.1 network (1Gbit). Longhorn is running RedHat Linux 7.2 and has a shared RAID level 0 disk array of 140GB. This cluster was reconstructed in summer 2004.

Bevo was constructed in June 2003. It consists of 45 dual processor AMD Athlon 2400MP 2GHz computers (90 processors), each with 2GB ECC DDR RAM connected by a 1Gbit ethernet network and a Myrinet 2000 network (5Gbit). Bevo has a shared RAID level 0+1 disk array of 560GB.

6.2 PARAMETERS INPUT TO PARSSIM

Parssim starts running with an input file of the required format. One sample input file is attached in Appendix C. The detailed explanation of a general input file can be found in the Parssim user manual. As for any other reservoir simulator, the required input parameters include dimensions of the domain to be simulated, grid cell numbers in the selected coordinate system (rectangular in our case), and the fluid and rock properties. The important rock properties required are the permeability and the porosity for a single phase flow simulation. For a transport simulation, the diffusion coefficient and longitudinal and transverse dispersion coefficients are also required.

The porosity values were assigned to each grid cell from CT scan data as described in section 2.3. The permeability assigned to each cell depends on the cell type. Recall that the grid cells were categorized into four types: air in vugs, air outside the rock, mud, and rock. Since the sub-volume of the rock used in the computation (13.125 cm × 13.125 cm × 21.6 cm) was taken from the center of the entire sample, it does not include the air outside the rock. As discussed before, mud (mud filled vug) cells were considered as vug cells because presumably there is no recent sediment or mud inside the vugs in subsurface vuggy carbonates. Therefore, each cell in the computational sub-sample corresponds to only two types: vug or matrix. Since the vugs in this sample are large, flow through these cells was modeled by assigning them a relatively large permeability (of the order of many Darcies). Similarly a small permeability is assigned to matrix cells because the matrix has tiny pore space. As a result, the permeability field of the computational sub-sample in the fine grid level (240 × 240 × 144) contains only two values. The large value corresponds to the vug cell and the small value corresponds to the matrix cell. The permeability values are assumed to be scalar quantities.

For flow simulations, constant potential boundary conditions are given for one pair of faces in the flow direction and a no flow condition is specified to the other faces. For transport calculations, the step-input change is selected as the tracer injection type. At time zero, the concentration in each cell is zero.

6.3 PERMEABILITY SCALE-UP INVESTIGATION

Upscaling from fine scale to coarse scale is necessary because the computation on more than eight million cells did not fit into the available computer memory. Moreover, fewer grid cells after upscaling make the computation much faster. The computational grid for the sub-sample directly mapped from CT scan is called level zero, which has $240 \times 240 \times 144$ cells. An upscaling was made from level zero to level 1 by a factor of $3 \times 3 \times 1$. Thus each cell in upscale level 1, whose dimensions is $80 \times 80 \times 144$, includes $3 \times 3 \times 1$ fine cells from 0 level. Cells at upscale level 1 are approximately cubes with side 1.5 mm. Each higher level (from 2 to 8) is upscaled from its previous level by a factor of $2 \times 2 \times 2$. Hence, the cells remain approximately as cubes for all the subsequent upscale levels. The different upscale levels and corresponding grid cells are shown in Table 6.1.

The porosity and permeability have to be upscaled to the higher level accordingly. The porosity is upscaled by simply taking the arithmetic average of the porosities in the fine grid. The permeability upscaling, however, is not this simple. Permeability upscaling has been an important topic for researchers working on reservoir simulation. Permeability upscaling is a technique that will enable us to generate a coarse-grid simulation model from a fine-grid simulation model which captures the fluid flow behavior in the fine-grid system. The ideal upscaling method will provide an appropriate effective permeability without losing key features of the fine grid system. Therefore, numerical simulations were performed to discover an appropriate upscaling method for our rock sample. The

next section reviews related studies in the literature on permeability upscaling. The approaches being applied to investigate the permeability upscaling in this research is explained afterwards.

6.3.1 Literature Review on Power Averaging

An extensive review on permeability averaging techniques can be found in papers by Renard and de Marsily (1997). They reviewed more than 20 permeability averaging methods and categorized them into three groups: heuristic methods, deterministic and stochastic methods. A detailed illustration of each method and comparisons between them was given in their study.

Power averaging has been found to be an effective method to calculate the effective permeability (e.g., Journal et al., 1986, Deutsch, 1985). The formula of power average is shown in Eq. 6.1. When $\alpha = -1$, power average becomes harmonic average; when $\alpha = 1$, power average becomes arithmetic average; when $\alpha = 0$, the power average becomes geometric average through a limit expansion of formula 6.1. A detail theoretical derivation of formula 6.1 was given by Noetinger and Jacquin (1991) and Noetinger (1994). The assumption of obtaining this formula is that the local permeability is isotropic and random.

$$k_{eff} = \left(\frac{1}{n} \sum_{i=1}^n k_i^\alpha \right)^{\frac{1}{\alpha}}, \alpha \in (-\infty, +\infty) \quad (6.1)$$

The effective permeability of a composite block with any permeability in each composite cell, shown in Figure 6.1, has been believed to lie in between the harmonic and the arithmetic average (e.g., Cardwell and Parsons, 1945, Journal et al., 1986, Deutsch,

1989). This means the algebraic exponent α in formula 6.1 is between -1 and +1. Later, Noetinger and Jacquin (1991) and Noetinger (1994) demonstrated experimentally that α equals 1/3 for a 3D log-normal medium with relatively small or no correlation length. Using a renormalization group analysis method, Hristopulos and Christakos (1999) also showed that the 1/3 power average calculates effective permeability in a 3D, spatially uncorrelated and lognormal porous medium.

6.3.2 Investigation of Permeability Upscaling Method

6.3.2.1 Power Average Method

One-third power averaging was used as the permeability upscaling method in our research. To verify that 1/3 is an appropriate exponent for our permeability field, effective permeability was calculated for four upscale levels and for different exponents. If the effective permeability remains the same for all upscaling levels with 1/3 power averaging, then this method preserves the total flow capacity in the fine scale. However, if the effective permeability changes, then the 1/3 power averaging is inappropriate. The effective permeability was also compared for different algebraic exponents. The results showed that one-third power averaging was an adequate method for permeability upscaling in our research. The next paragraph explains the simulation procedure.

To find an appropriate exponent in equation 6.1 for permeability upscaling, vug cells were assigned a permeability of 10 Darcy and matrix cells were assigned a permeability of 1 md at the zero upscale level. Permeability for each grid cell in higher upscale levels was calculated using power average method with dependent exponent values. The effective permeability of the computational sub-sample was calculated giving the potential difference and the flow rate computed from the simulation for each

upscaling level. The same procedure was repeated for flow in three directions and for exponents ranging from -2 to 1. The simulation results are shown in Figure 6.2, Figure 6.3, and Figure 6.4, where L1, L2, L4, and L8 mean upscaling levels 1, 2, 4 and 8 respectively.

In Figure 6.2, the effective permeability decreases dramatically with the upscale level when the exponent α is less than $1/3$; whereas it increases with the upscale level when α is equal to 1. The effective permeability remains relatively the same when α is equal to $1/3$. This observation is also true for the effective permeability in other two flow directions (Figure 6.3 and Figure 6.4). Therefore, $1/3$ power averaging is concluded as a good method for the permeability field in our sample. However, an inverse deduction of the condition for one-third power averaging is not true because the vugs in our sample are correlated. That is, a conclusion of log normal distributed permeability field of zero or small correlation length can not be deducted only because $1/3$ power averaging gives good result.

In addition, using the $1/3$ power averaging, the effective permeability for flow in the z direction remains more consistent for different upscale levels than that in the x and y directions. This suggests that for our permeability field, $1/3$ power averaging preserves the flow properties better in the z direction than in the x and y directions. This might be caused by two reasons. First, the permeability is anisotropic. The permeability field in the x and y directions might be more spatially correlated than that in the z direction. However, $1/3$ power averaging works well for spatially uncorrelated permeability field. The second possible reason is that the sample length in the z direction (21.6 cm) is larger than the x and y directions (13.125 cm). One third power averaging method perhaps allows averaging for a larger distance relative to the correlation length.

6.3.2.2 Common Vug Cell Method

Besides power averaging, another upscaling method was investigated in our research, which is called the common vug cell method. The purpose of this investigation was not to find a permeability upscaling method, but to simply understand a simple upscaling approach. In this investigation, the permeability was upscaled only to the first level. Recall that the upscaling factor from level zero to level 1 is $3 \times 3 \times 1$. The general rule of the common vug cell method is that if the number of vug cells m among the nine neighbor cells at zero level is at least a certain number M ($m \geq M$), then the upscale cell at the first level is assigned to be the vug permeability. Otherwise ($m < M$) it is assigned to be the matrix permeability. The expression is shown in (Eq. 6.2).

$$k_i = \begin{cases} k_{vug}, m \geq M, M \in [0, 9] \\ k_{matrix}, m < M, i \in [1, 80 \times 80 \times 144] \end{cases} \quad (6.2)$$

where k_{vug} is the permeability of vug cells at level zero, $[L^2]$,

k_{matrix} is the permeability of matrix cells at level zero, $[L^2]$,

M is a pre-determined number for each investigation. It ranges from 1 to 9,

m is a variable that counts the number of vug cells among nine fine cells at level zero,

i is the cell subscript at the first level.

The permeability at level zero is a binary field of 10 Darcy in vug cells and 1 md in matrix cells. Therefore, after upscaling, the permeability at the first level is still a binary field of 10 Darcy in vug cells and 1 md in matrix cells. An example case when $M = 5$ is given to explain the common vug cell method. If there are at least 5 vug cells among the nine neighboring cells at level zero, then the permeability at the first level is

assigned to be 10 Darcy. Otherwise, if there are less than 5 vug cells among the nine neighboring cells at zero level, then the permeability at the first level is assigned to be 1 md.

The permeability was upscaled to level 1 for M ranging from 1 to 9 and the effective permeability was computed using Parssim for simulations in the x and z directions at level 1. Obviously, the effective permeability is larger if there are more vug cells at level 1. Therefore, $M = 9$ produces the smallest effective permeability because it requires nine vug cells at zero level for a vug permeability at level 1. On the other hand, $M = 1$ produces the largest effective permeability because the vug cell permeability would be assigned to the upscale level with only one vug cell among nine fine cells at zero level. The effective permeability results are shown in Figure 6.5. Apparently, the effective permeability decreases with the increase of the number of vug cells M , minimum requirement for the coarse cell to have vug permeability.

The effective permeability calculated at level 1 from the common vug cell upscaling method was compared with that from the one-third power averaging. Figure 6.2 shows that with 1/3 power averaging, the effective permeability in the x direction for the upscale level 1 is around 50 md. Figure 6.4 shows that the effective permeability in the z direction for upscale level 1 is around 30 md. The permeability field at level zero was the same for both upscaling investigations. Therefore, these results and those shown in Figure 6.5 are based on the same condition and are comparable. Figure 6.5 shows that the effective permeabilities of 50 md and 30 md in the x and z directions both correspond to the vug cell number M between 3 and 4. This indicates that when M is set as a value between 3 and 4, then the common vug cell upscale method is equivalent to the one-third power averaging for the current permeability field assignment.

6.4 SINGLE PHASE FLOW SIMULATION

6.4.1 Vug Connectivity Investigation

Simulations were conducted to investigate the connectivity of the vug cells in the computational sub-sample. This was achieved by comparing the effective permeability of the sub-sample for a series of permeability assignment in vug cells. The permeability of matrix cells was fixed as 1 md. The permeability of vug cells varied from 100 md to 900 Darcy. These values were picked arbitrarily. If the effective permeability reaches an upper limit as the permeability of vug cells increases, then a conclusion may be reached that the vug cells are not connected. If, on the other hand, the effective permeability increases with the permeability in the vug cells without limit, then the conclusion is that the vug cells are connected.

The simulation results are shown in Figure 6.6, Figure 6.7 and Figure 6.8, where the dimensionless effective permeabilities were plotted against dimensionless vug permeability. Because these three figures are very similar and show the same information, only Figure 6.6 is discussed in detail in the following of this section. The dimensionless effective permeability in this plot has a very clear increasing tendency with dimensionless vug permeability for all upscale levels, which were labeled as L1, L2, L4, and L8 in the figures. The increasing tendency seems to have no limit. This means the larger the assigned vug permeability, the larger the calculated effective permeability. This indicates that vugs must be connected in this computational sub-sample because the increase of the permeability in the isolated voids would have little effect on the effective permeability of the sample if there were no connections between vugs. Therefore, the vugs in this computational sub-sample are connected. This confirms the result found in section 3.2 that vugs are connected to all directions.

Figure 6.6 also shows that the effective permeability is about 2 orders of magnitude smaller than the permeability value assigned to the vug cells. This suggests the vugs are connected through narrow throats. This observation is consistent with the results obtained from the theoretical model calculations in Chapter 5. It was found in Chapter 5 that the vugs are connected through small throats of less than 4 mm in sample A and less than 1 mm in sample C. The effective permeability can also be smaller if there were not many vug cells. In fact, this is consistent with the result obtained from CT scanning and flow experiments (Chapter 2 and Chapter 4). Sample A contains the most number of vugs compared to sample B and sample C, and it has the largest permeability. However, sample B, on average, contains the least number of vugs and it has the smallest permeability.

6.4.2 Comparison of Simulations with Experiments

Because the computational sub-sample was mostly from sample B (Figure 2.4), its numerically computed effective permeability in the z direction was compared with the effective permeability of sample B measured from the experiment, which was of the order of 10 md. Figure 6.8 shows that when the dimensionless vug permeability is 10,000, the dimensionless effective permeability of the sub-sample is between 10 and 100. Since the matrix permeability was assigned as 1 md, the corresponding vug permeability and effective permeability are 10 Darcy and several tens of millidarcy respectively. This indicates that assigning 10 Darcy to vug cells in the simulation and 1 md to matrix cells would give an effective permeability on the order of that measured from the experiment. Therefore, 10 Darcy was assigned to vug cells and 1 md was assigned to matrix cells for the other flow and transport simulations.

Figure 6.9 shows the effective permeability in three flow directions for different upscale levels. It shows that the effective permeability is different in three directions at each upscale level, which indicates that the effective permeability is anisotropic.

6.4.3 Summary

The single phase flow simulation results indicate the following:

- The vugs within the computational sub-sample are found to be connected.
- Vugs are connected through narrow throats.
- One-third power averaging is found to be an appropriate permeability upscaling method for effective permeability calculations. The common vug cell method was found to be equivalent to one-third power averaging with a vug number threshold between 3 and 4.
- One-third power averaging preserves the effective flow capacity better in the z direction than that in the x and y directions.
- The effective permeability is anisotropic

6.5 CONSERVATIVE TRACER TRANSPORT SIMULATION

As mentioned in section 6.4.2, permeability of 10 Darcy was assigned to vug cells and 1 md to matrix cells for transport simulations. The porosity field was mapped from the CT scan data. A step-input concentration boundary condition was used. The effluent concentration history output file from the simulation using Parssim is the pore volume average of the primary phase concentration, which does not incorporate the permeability heterogeneity and cannot predict the effluent concentration measured from experiments. Therefore, a flow velocity averaged concentration was needed because it can incorporate

the permeability heterogeneity in the effluent concentration. The flow velocity average concentration is calculated as the velocity average of the concentration at each grid cell in the outlet face of the computational sub-sample when all grid cells in this face have the same dimensions (Eq. 6.3).

$$C_{avg} |_{z_D=1} = \frac{\sum_{i,j} C_{i,j} v_{i,j}}{\sum_{i,j} v_{i,j}} \quad (6.3)$$

where $C_{avg} |_{z_D=1}$ means the average concentration at the outlet, dimensionless,

i,j are the subscript in the x and y directions, which both range from 1 to 240,

$C_{i,j}$ is the cell concentration at the outlet face, which is Parssim output,

dimensionless,

$V_{i,j}$ is the cell velocity at the outlet face, which is Parssim output, [LT^{-1}].

The Parssim output data was then post processed to obtain the effluent concentration history. Parssim output data includes concentration in each grid cell, the corresponding output time and velocity in each grid cell.

6.5.1 Physical Dispersion Evaluation

To include dispersion in the transport simulations, the *uniformDispersion* option in Parssim was selected. This option assumes constant dispersivities in both the longitudinal and the transverse directions and a constant molecular diffusion coefficient. In our simulations, the dispersivity was set an order of magnitude larger in the longitudinal direction than in the transverse direction.

Figure 6.10 plots the effluent concentration histories from numerical simulations with and without dispersion for flow in the z direction. The dispersivity in the

longitudinal direction was given 1 cm for the simulation with dispersion. The figure shows that the curve without dispersion seems to reflect a more heterogeneous pore space than the one with dispersion. This suggests that the heterogeneity caused by the permeability field, 10 Darcy for vug cells and 1 md for matrix cells in zero upscale level, is very large. The addition of 1 cm dispersivity uniformly to each grid cell may eliminate some of the permeability heterogeneity and generate a curve like that shown in Figure 6.10. This suggests that assigning a dispersivity uniformly to both the vug and the matrix grid cells might be inappropriate. A nonuniformly distributed dispersivity field might be necessary to address the difference of the dispersion behavior between the vug and the matrix. The nonuniform dispersion assignment can be carried out using Parssim in future transport simulations.

The numerical simulation results are compared with the effluent concentration history from experiment four in Figure 6.11. Although the computational sub-sample does not exactly correspond to the sub-sample used in the experiment, sample C, but they occupy similar regions of the original sample (Figure 2.4) and have similar total porosities and vug volume fractions (Chapter 2). Nevertheless, the simulated tracer breakthrough is much slower than the experiment. The arbitrary permeability assignments used for vug and matrix voxels in the simulation might be one reason for the mismatch. However, it is also likely that the Darcy's law assumption for flow in the vugs is not adequate. A coupled Darcy-Stokes simulation, using Darcy's law in the matrix and Stokes' law in the vugs, might be necessary for accurate transport simulations in touching-vug systems.

Figure 6.12 plots the effluent concentration histories with and without dispersion assigned to the simulation for two upscale levels (Level 1 and Level 8). The figure shows that the curves in upscale level 8 show less heterogeneity than that of the upscale level 1.

This is because the upscaling process eliminated some heterogeneity in upscale level 8. This seems to suggest that the one-third power average may not be an accurate upscale method in preserving the transport behavior of fluid through the current rock system, despite of its usefulness for estimating permeability.

The figure also shows that the physical dispersion displayed by the effluent concentration history decreased from level 8 to level 1 in the curve with dispersion compared with the curve without dispersion. For upscale level 1, the effluent concentration history with a dispersivity of 1 cm seems to display less dispersion than that without dispersivity assignment. However, for upscale level 8, the effluent concentration history with a dispersivity of 1 cm seems to display more dispersion than that without dispersivity assignment. This might be attributed to the fact that the dispersivity did not upscale along with the permeability from level 1 to level 8. As discussed before, the permeability field in level 8 is less heterogeneous than that in level 1. Thus incorporating a dispersivity into the transport simulation in a less heterogeneous field (level 8) might efficiently include the dispersion into the effluent concentration history. However, incorporating the same dispersivity in a more heterogeneous permeability field (level 1), on the other hand, might eliminate some heterogeneity. This indicates that it might be necessary to upscale dispersivity along with the permeability with an appropriate method to obtain consistent concentration effluent profiles.

6.5.2 Summary

The transport simulations on the upscale levels indicate the following:

- Darcy's law assumption in both matrix and vug cells may not illustrate the transport behavior of flow through this vuggy system because the effluent

concentration history from the simulation did not predict the transport behavior observed from the experiment.

- The higher upscale level displayed much less heterogeneity than that displayed in the lower level, which suggests that one third power averaging may not be an accurate method in preserving the transport properties of this heterogeneous medium.
- The concentration history from the simulation with a uniform dispersion assignment displayed less heterogeneity than that without dispersion. This indicates that the uniform dispersion coefficient assignment may not be appropriate for transport simulations with the current permeability field assignment. The concentration history obtained from transport simulations with dispersion assignment displayed more heterogeneity in level 8 than in level 1 compared to the concentration history without dispersion assignment. This suggests that a dispersivity upscaling is necessary to obtain consistent concentration histories.

6.6 FLOW AND TRANSPORT SIMULATION ON TOUCHING-VUG NETWORK SYSTEM

To understand the contribution of the touching-vug network to flow and transport through the vuggy samples, high resolution numerical simulations were performed on the largest touching-vug network system obtained from computational visualization. Tracer transport behavior obtained from the touching-vug network simulation was compared with that obtained from the experiment.

As described in section 3.2.1.2, a data set of zeros and ones was obtained from the flow path computation in the z direction. All voxels having number one were considered to belong to the touching-vug network. Voxels having number zero were viewed as

matrix. The matrix here includes both the matrix concept defined in Chapter 2 and the separate-vugs in the computational sub-sample (21% of the pore volume, explained in section 3.2.1.2). Thus, the simulations were focused on the touching-vug network and treated the separate-vugs as part of the matrix. Therefore, a large permeability was assigned to voxels that belong to the touching-vug network and a small permeability to the rest voxels. One-third power averaging was used to up scale the permeability. The initial and boundary conditions for flow and transport simulations for the touching-vug network were the same as those described in section 6.5. Numerical simulations were performed for the upscale levels 1 and 2.

6.6.1 Flow Simulation Results

The velocity vector from numerical simulation in upscale level 1 was imported into Amira and the velocity in the z direction was visualized, which is shown in Figure 6.13. The figure shows that more than one flow path in the z direction and there are narrow throats in the touching-vug network where the velocity streamlines come closer together. The streamlines in the figure were colored according to velocity magnitudes. White color represents small velocity; red and yellow colors represent large velocity.

A small velocity was set as a threshold to filter the velocities smaller than it. The voxels having velocities below the threshold were considered not to contribute to flow. The voxels having velocities higher than the threshold were set to value 1, the rest voxels were set to 0. Hence, the voxels having an integer 1 are those that contribute to flow and the total volume of these cells was called the flowing-vug volume. The arithmetic average of all zeros and ones in the array of $240 \times 240 \times 144$ was calculated, which was the ratio of the flowing-vug volume to the bulk volume of the computational sub-sample. It was determined that the flowing-vug volume accounts for 4.6% of the bulk volume and

21% of the total pore volume of the sub-sample. Thus the dead-end-vug volume in this sub-sample was obtained as the difference between the touching-vug network volume and the flowing-vug volume. The results show that 22% of the total pore volume is in the dead-end-vug volume. A complete summary of the seven types of volumes (pore volume, matrix pore space, vug volume, separate-vug volume, touching-vug network volume, flowing-vug volume and the dead-end-vug volume) in this computational sub-sample is shown in Table 6.2, which also includes the computation result explained in section 3.2.1.2. The relationships among these volumes are also listed in the table, which are summarized below with all volumes normalized by the pore volume:

- Pore volume (1) = Matrix pore space (36%) + Vug volume (64%),
- Vug volume (64%) = Separate-vug volume (21%) + Touching-vug network volume (43%),
- Touching-vug network volume (43%) = Flowing-vug network volume (21%) + Dead-end-vug volume (22%).

6.6.2 Transport Simulation Results

The concentration history from touching-vug network at upscale level 1 was also compared with the result from experiment four in Figure 6.14. Similar to Figure 6.11, this figure shows that the breakthrough time of the simulated concentration history was later than that of the experiment. The possible reasons are the same as those explained for Figure 6.11.

Two effluent concentration histories from the touching-vug network simulation on upscale level 2 are shown in Figure 6.15. The voxels belonging to the touching-vug network were assigned to be 100 Darcy at zero level for both simulations. On the other

hand, one simulation had 10 md assigned to the matrix and the other simulation had 1 md assigned to the matrix. The permeability upscaling method and the dispersivity assignment for both simulations were the same. The figure shows that the curve with permeability field of 100 Darcy-network and 10 md-matrix shows less heterogeneity than that of 100 Darcy-network and 1 md-matrix. This is consistent with the permeability heterogeneity that the former one was less heterogeneous than the latter one. This suggests that the touching-vug network system works properly.

Figure 6.16 shows the effluent concentration history from the touching-vug network simulations for the upscale level 1 and 2. The zero level permeability fields and the dispersivity assignment were the same for these two simulations. The figure shows that the curve for upscale level 2 shows less heterogeneity than upscale level 1. This was also observed in simulation results shown in Figure 6.13. The same reason applies here that the $1/3$ power averaging method may eliminate some heterogeneity displayed at the lower upscale level. This indicates that the touching-vug network simulation generated similar results as that from the original CT scan array simulation, described in section 6.5, which showed that one third power averaging may not be adequate in preserving the transport properties.

6.6.3 Summary

- The study showed that in the computational sub-sample, only 43% of the pore volume is in the largest touching-vug network and 21% of the pore volume is separate vugs. Of the touching-vug network, 22% of the pore volume is in the flowing-vug volume. 21% of the pore volume in the flowing-vugs is found to be dead-end-vugs.

- It was discovered that the one third power averaging method may not preserve the transport properties for flow through the touching-vug network.

Table 6.1 Grid cells at each upscale level.

Upscale Level	$N_x \times N_y \times N_z$	Total Cells
0	240 × 240 × 144	8294400
1	80 × 80 × 144	921600
2	40 × 40 × 72	115200
4	20 × 20 × 36	14400
8	10 × 10 × 18	1800

Table 6.2 Hierarchy of seven types of pore volumes in the computational sub-sample.

	cm ³	Fraction of total pore volume
Total Pore Volume	806	1
Total Pore Volume = Matrix Pore Space + Vug Volume		
Matrix Pore Space	289	0.36
Vug Volume	517	0.64
Vug Volume = Separate-Vug Volume + Touching-Vug Network Volume		
Separate-Vug Volume	170	0.21
Touching-Vug Network Volume	347	0.43
Touching-Vug Network Volume = Flowing-Vug Volume + Dead-End-Vug Volume		
Flowing-Vug Volume	171	0.21
Dead-End-Vug Volume	176	0.22

k_1	k_2
k_3	k_4

Figure 6.1 Illustration of composite block. (Cardwell et al., 1944)

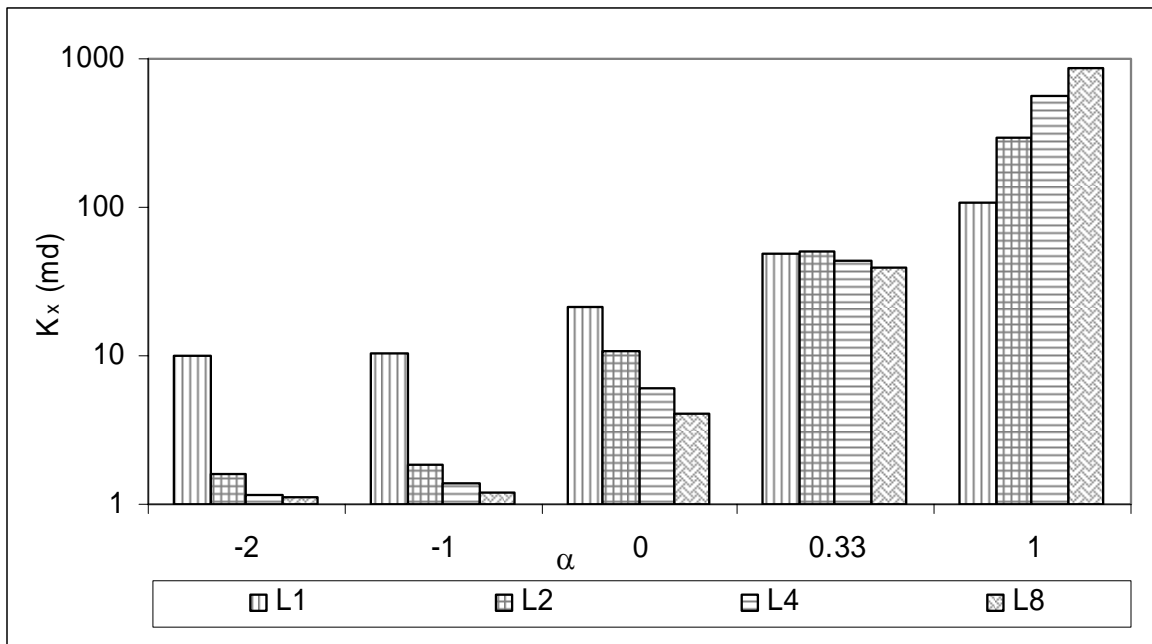


Figure 6.2 Effective permeability for flow in the x direction. L1, L2, L4 and L8 in the figure represent upscale level 1, 2, 4, and 8, respectively. α is the exponent in the power averaging equation (Eq. 6.1).

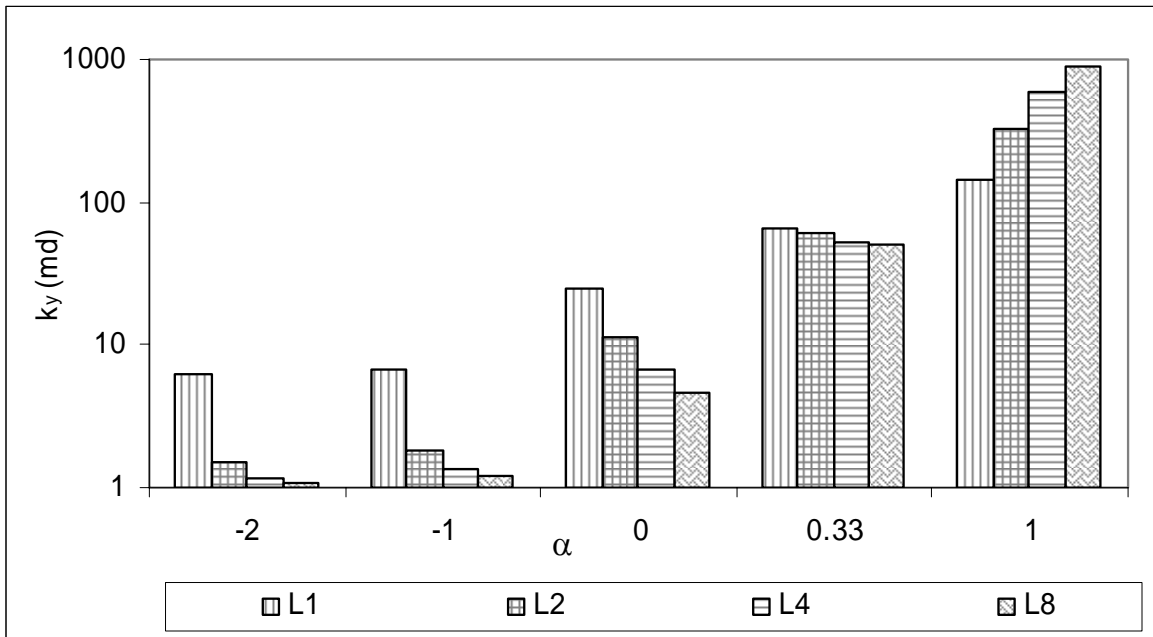


Figure 6.3 Effective permeability for flow in the y direction. L1, L2, L4 and L8 in the figure represent upscale level 1, 2, 4, and 8, respectively. α is the exponent in the power averaging equation (Eq. 6.1).

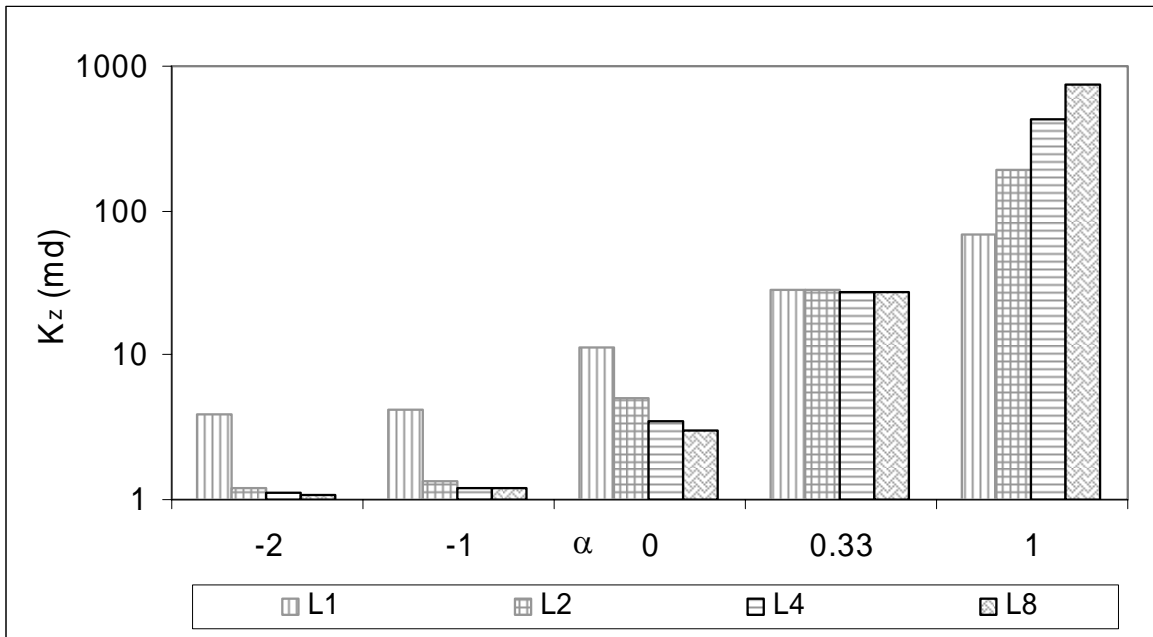


Figure 6.4 Effective permeability for flow in the z direction. L1, L2, L4 and L8 in the figure represent upscale level 1, 2, 4, and 8, respectively. α is the exponent in the power averaging equation (Eq. 6.1).

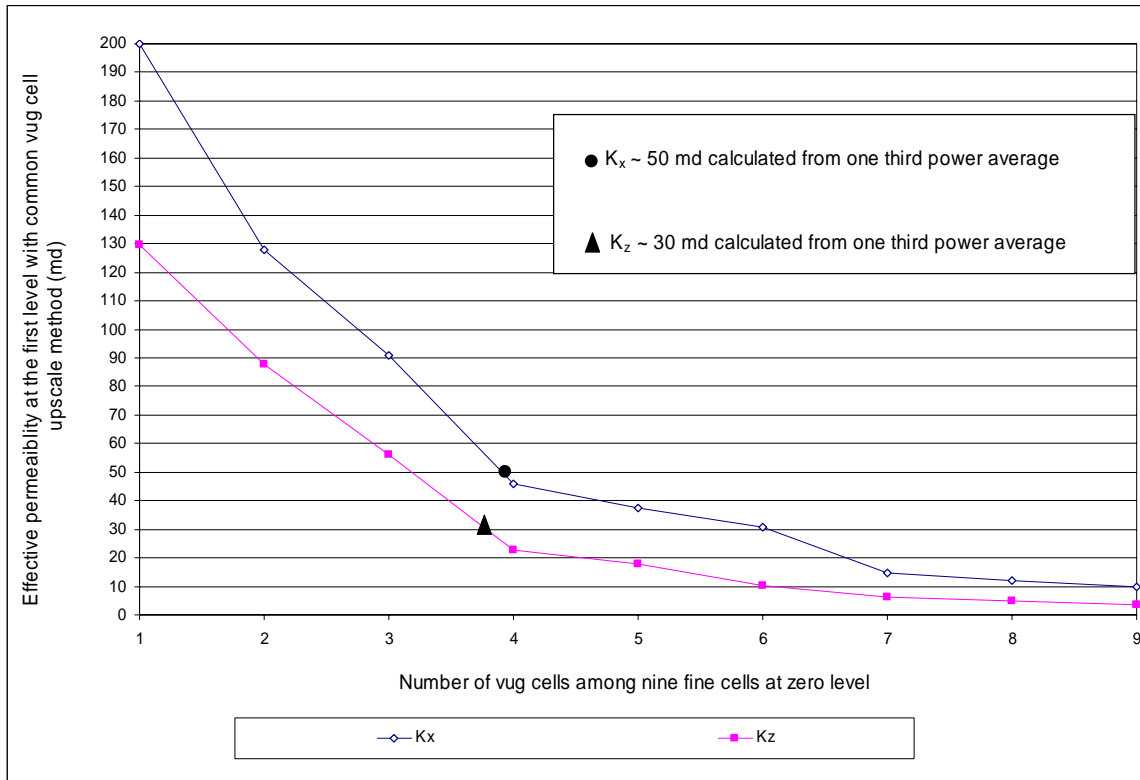


Figure 6.5 Effective permeability calculated from common vug cell permeability upscale method. The horizontal axis is the number of vugs, a parameter in the common vug cell upscale method; the vertical axis is the effective permeability of the computation sub-sample calculated from the flow simulations on the first upscale level with common vug cell permeability upscale method. The circle and triangular dots in the plots represent the effective permeabilities of the computational sub-sample in the x and z directions calculated from the flow simulations on the first level with 1/3 power averaging permeability upscaling method.

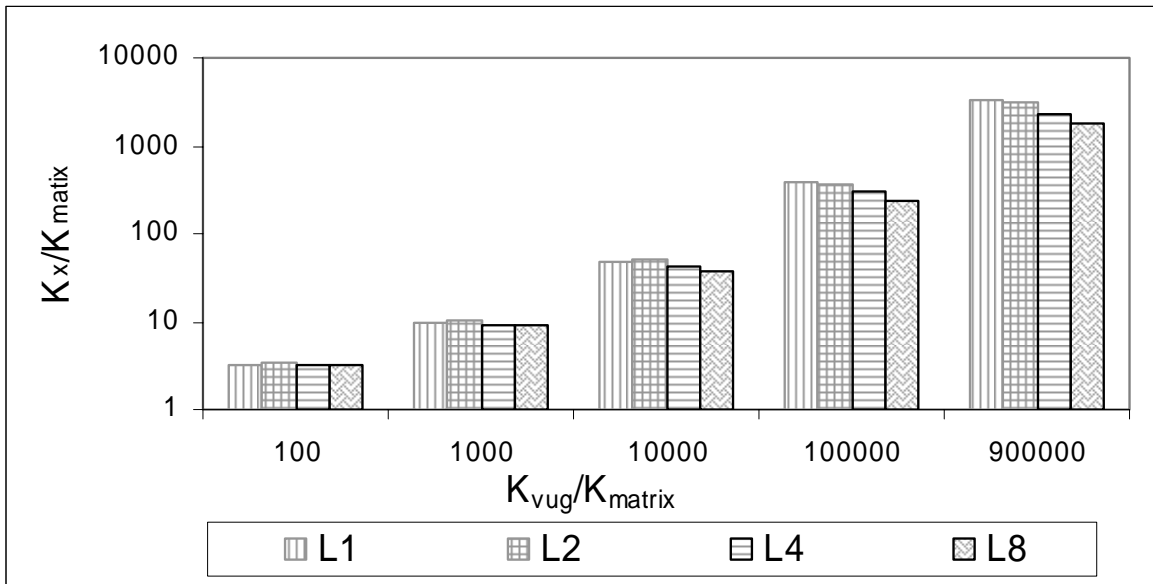


Figure 6.6 Dimensionless effective permeability for flow in the x direction. The effective permeability calculated from the simulation and the permeability assigned to vug cells are normalized by the matrix permeability. L1, L2, L4 and L8 in the figure represent upscale level 1, 2, 4, and 8 respectively.

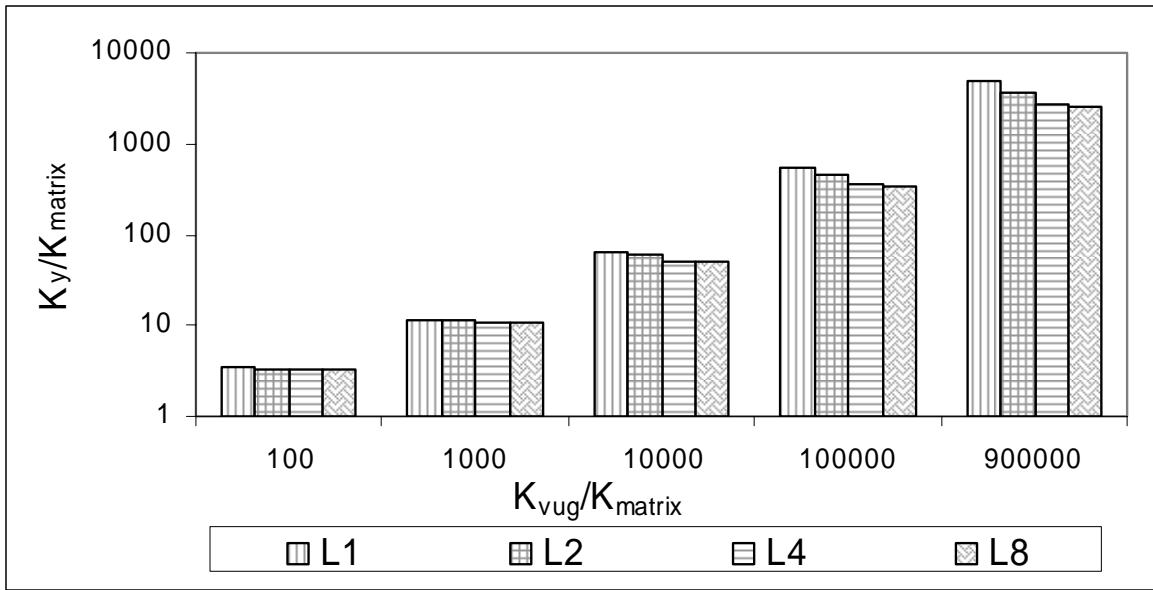


Figure 6.7 Dimensionless effective permeability for flow in the y direction. The effective permeability calculated from the simulation and the permeability assigned to vug cells are normalized by the matrix permeability. L1, L2, L4 and L8 in the figure represent upscale level 1, 2, 4, and 8 respectively.

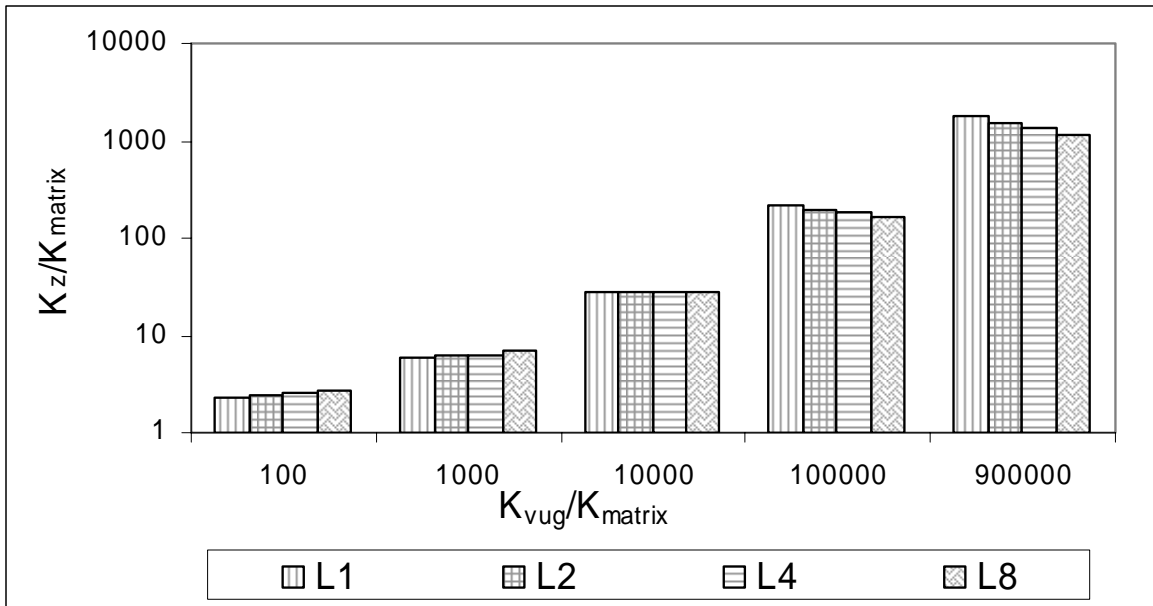


Figure 6.8 Dimensionless effective permeability for flow in the z direction. The effective permeability calculated from the simulation and the permeability assigned to vug cells are normalized by the matrix permeability. L1, L2, L4 and L8 in the figure represent upscale level 1, 2, 4, and 8 respectively.

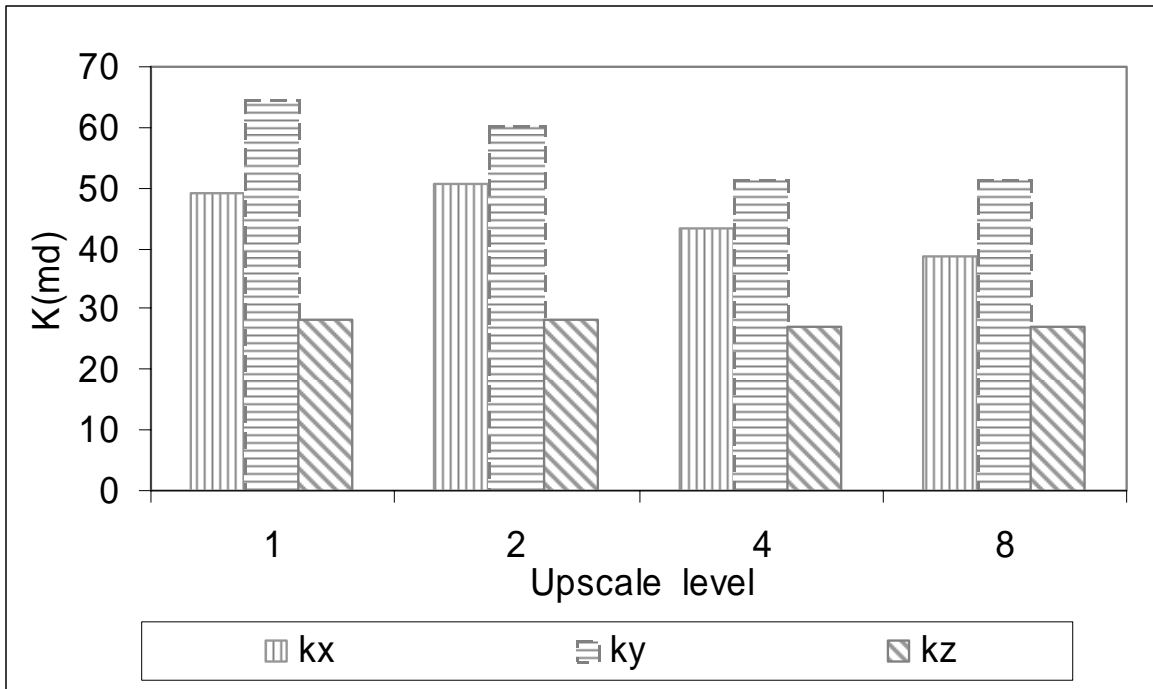


Figure 6.9 Dimensionless effective permeability in three directions. The effective permeability calculated from the simulation and the permeability assigned to vug cells are normalized by the matrix permeability. L1, L2, L4 and L8 in the figure represent upscale level 1, 2, 4, and 8 respectively.

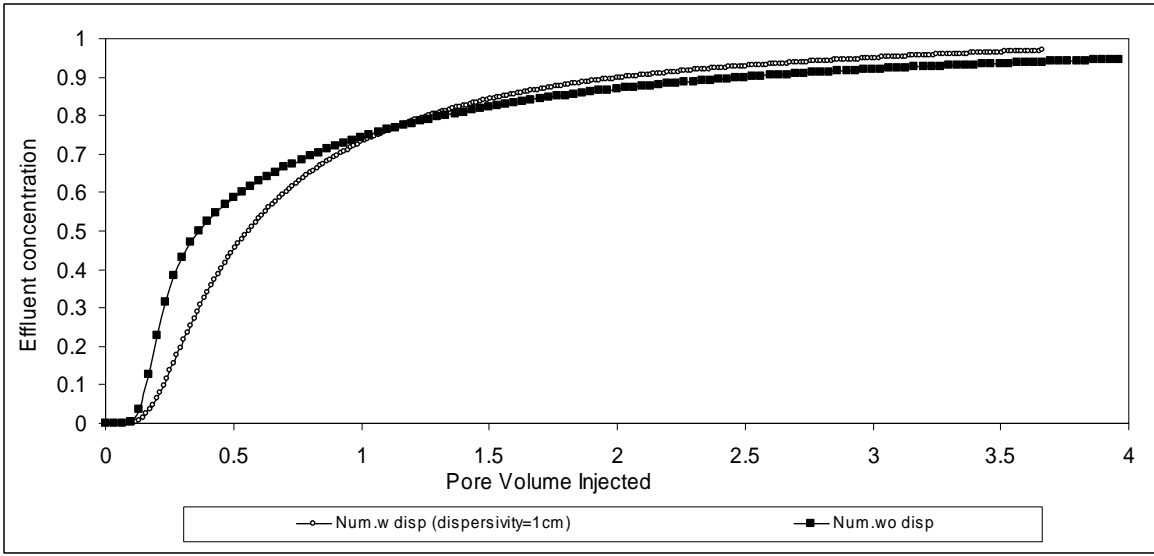


Figure 6.10 Effluent concentration histories at upscale level 1 for simulations with and without dispersions modeling in the simulations.

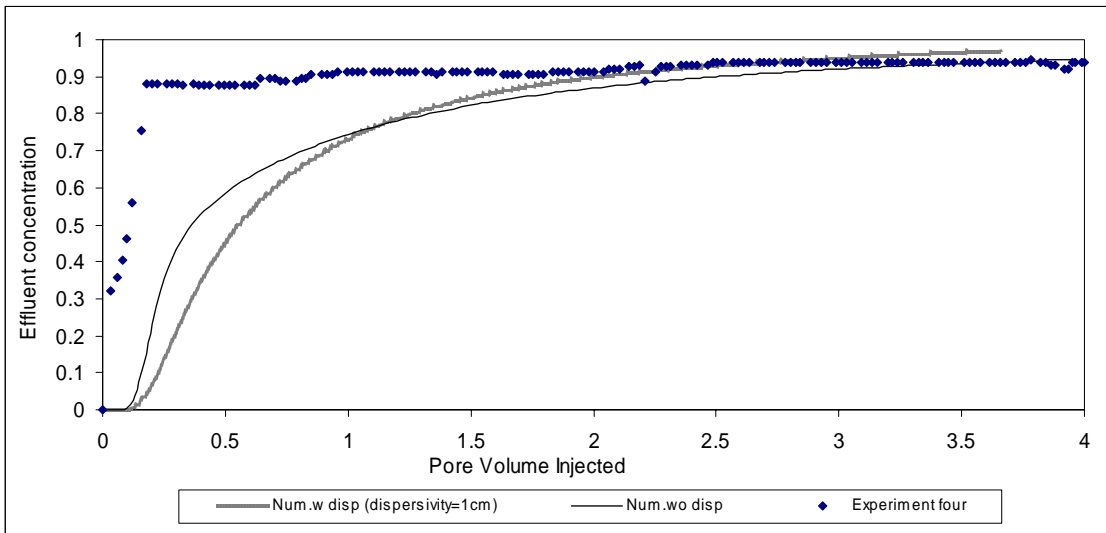


Figure 6.11 Comparison of effluent concentration history from experiment four with numerical results from simulations on upscale level 1.

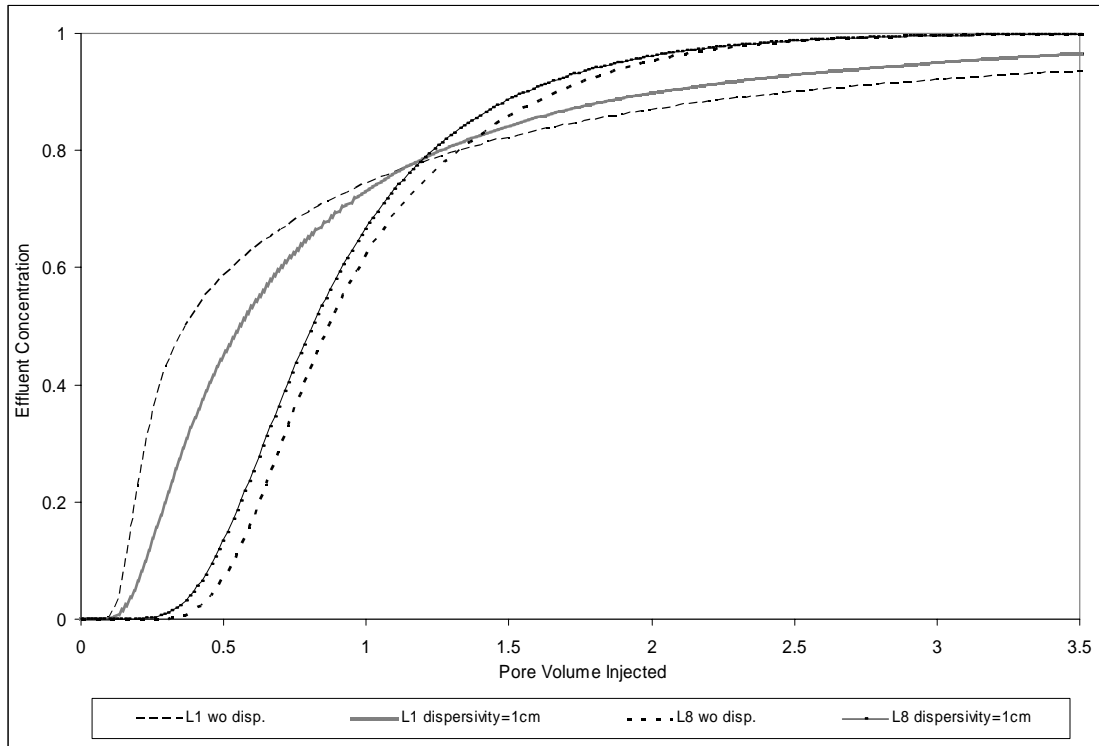


Figure 6.12 Effluent concentration histories from simulation for upscale level 1 and 8. “L1 wo disp.” shows results from upscale level 1 without dispersion modeling in the simulation. “L1 dispersivity = 1 cm” shows results from upscale level 1 with dispersion modeling in the simulation. Results from upscale level 8 are labeled similarly.

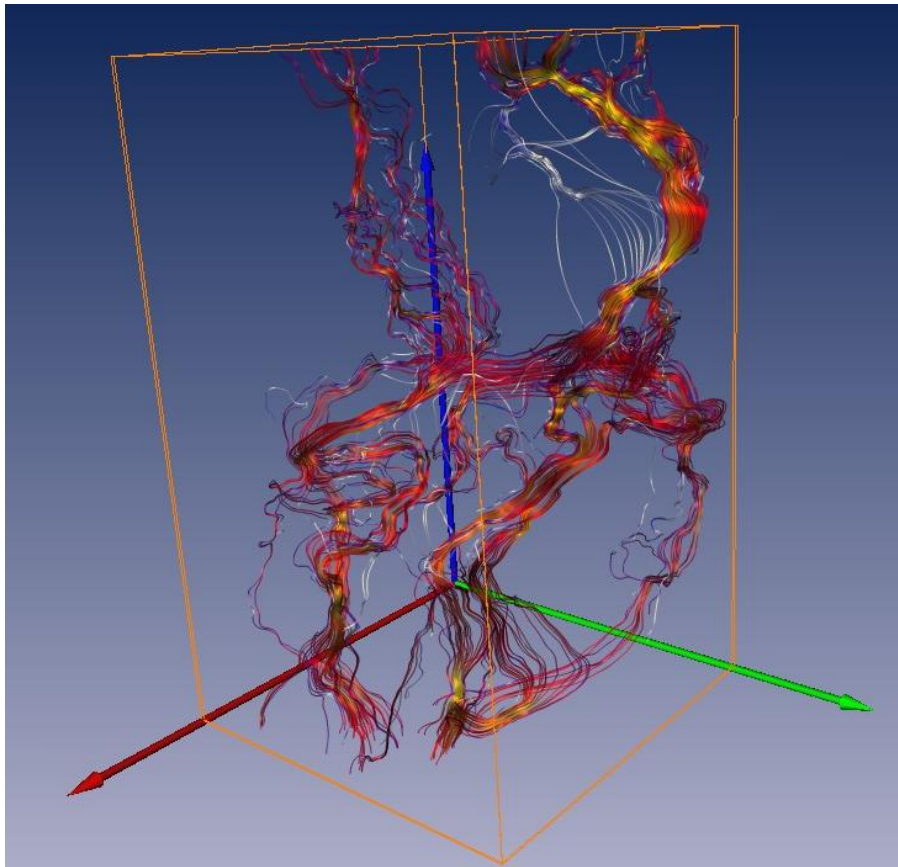


Figure 6.13 Velocity streamlines from touching-vug network simulation for flow in the vertical direction. The touching-vug network is shown in Fig. 3.3.

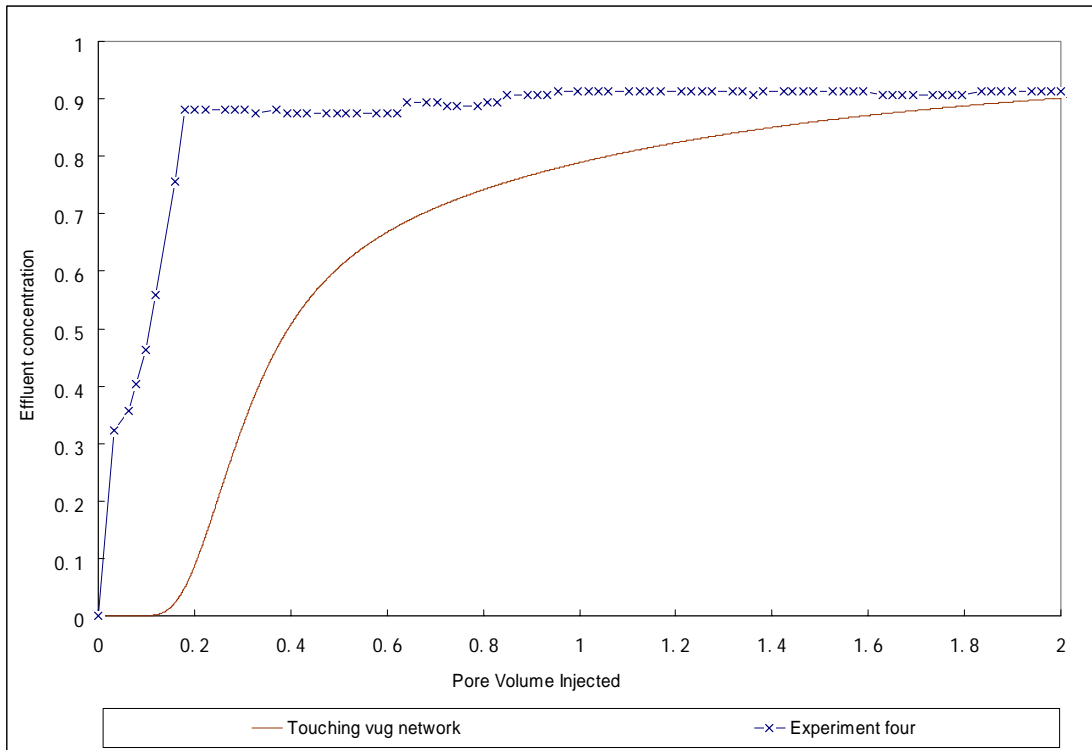


Figure 6.14 Effluent concentration histories from experiment four and touching-vug network simulation on upscale level 1. The longitude dispersivity used in the modeling was 0.5 cm for both simulations.

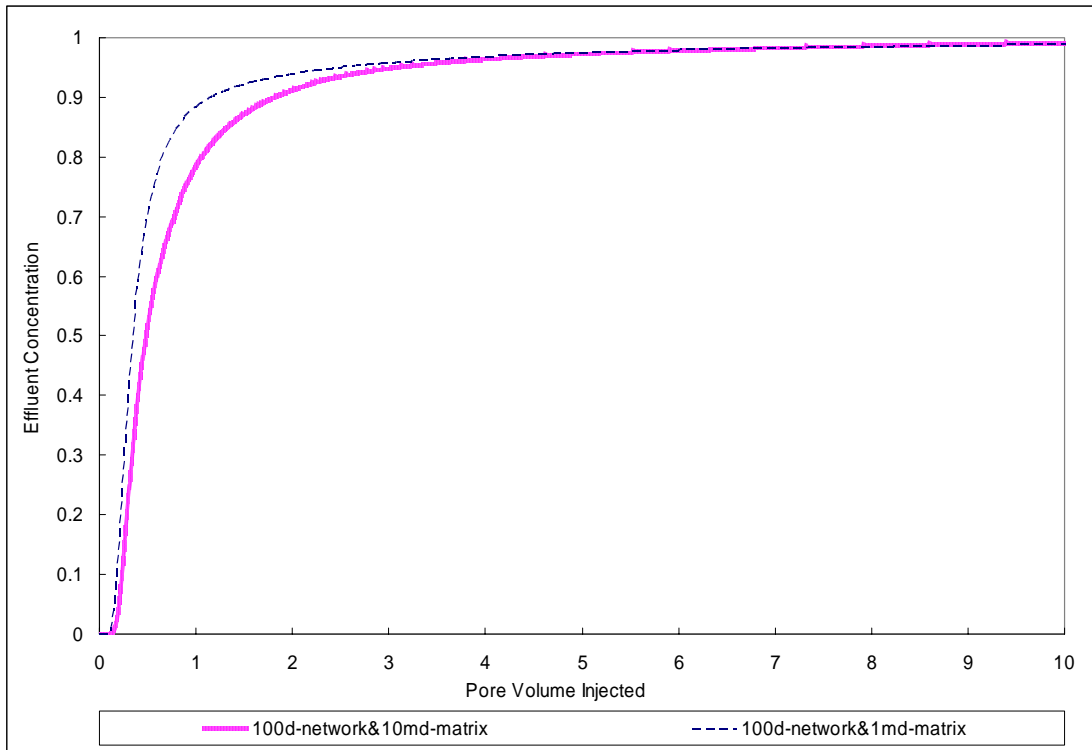


Figure 6.15 Effluent concentration histories from transport simulation on the touching vug network simulation for the upscale level 2. 100d-network&10md-matrix in the label means that the permeability field at the zero level was assigned as 100 Darcy for vugs in the touching vug network and 10 md was assigned for matrix. 100d-network&1md-matrix in the label means that the permeability field at the zero level was assigned as 100 Darcy for vugs in the touching vug network and 1 md for matrix. This figure shows the more heterogeneous the permeability field, the more heterogeneous displayed in the concentration histories.

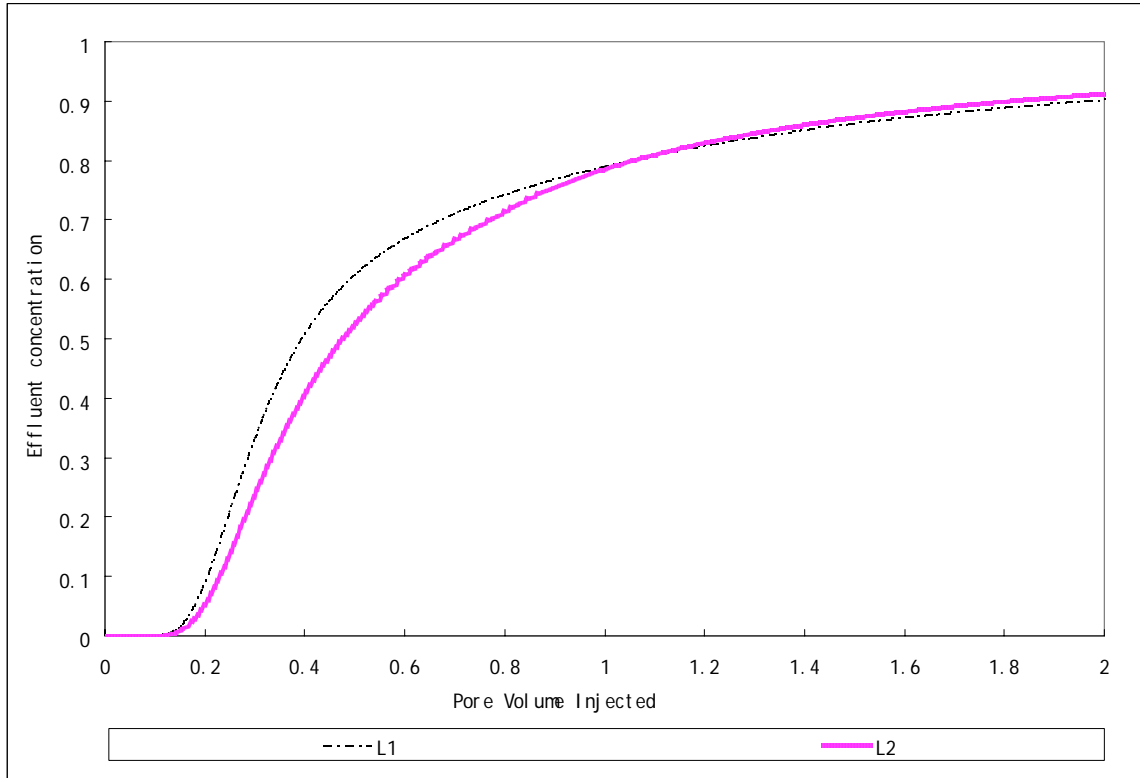


Figure 6.16 Effluent concentration histories from transport simulation on the touching-vug network simulation on the same permeability field at different upscale level. L1 means upscale level 1; L2 means upscale level 2. The zero level permeability fields for both simulations were 100 Darcy for vugs in the network and 10 md in the matrix.

NOMENCLATURE

α	Exponent in power averaging equation 6.1
$C_{i,j}$	Cell concentration at the outlet face from Parssim output, dimensionless
$C_{avg} _{z_D=1}$	Average concentration at the outlet, dimensionless
i	Cell subscript at the first level in equation 6.2
i,j	Subscript in the x and y directions
k_{eff}	Effective permeability of a composite block with any permeability in each composite
k_{matrix}	Permeability of matrix cells at level zero, [L ²]
k_{vug}	Permeability of vug cells at level zero, [L ²]
m	Variable that counts the number of vug cells among nine fine cells at level zero
M	Pre-determined number for each investigation.
$V_{i,j}$	Cell velocity at the outlet face from Parssim output, [LT ⁻¹]

Chapter 7 Conclusions and Future Study

7.1 CONCLUSIONS

A method was developed to characterize the pore space of a vuggy Cretaceous caprinid sample from a debris deposit in the Pipe Creek Reef of Central Texas. Flow and transport through the vuggy carbonate was studied using techniques of physical experiments, numerical simulations, theoretical modeling, and high resolution computational visualizations. Flow and transport behavior through the touching-vug network were discussed. Heterogeneity scales were discovered for the vuggy sample. It was concluded that vugs within the sample are connected into flow paths. However, there is a large volume of dead-end vugs detected in the computational sub-sample. The key conclusions of this work are summarized as follows:

- Vugs present in the sample are connected into flow paths. This conclusion was obtained from experimental observations and measurements, computed tomography (CT) scan data computations, and numerical simulations. The presence of modern mud inside the vugs suggests that the vugs are connected and provided channels for mud to travel through. The flow simulations also showed that the effective permeability increases with the vug permeability without limit. This indicates that vugs are interconnected and form flow paths. It was found from the touching-vug network characterization that the network forms connected flow paths spanning the computational sub-sample in all three coordinate directions.

- The vugs are connected through narrow throats. This was determined from the experiments, simulations, and theoretical modeling. The fact that the vug connections were easily plugged by mud and resulted in a zero flow rate during the experiments indicates that the vugs are connected by narrow throats. The aperture of the connections between vugs within the sample is estimated to be a few millimeters in diameter or less using bundle-of-capillary-tubes models.
- The measured effective permeability ranges from 10 md to 100 Darcy for three sub-samples. This permeability difference suggests that the connectivity of vugs varies with sub-samples. It was found that there are more vug voxels and possibly better connectivity toward the bottom of the 36 cm high sample. Sample A, the bottom portion, has the largest number of vugs and thus the largest permeability. Sample B, the middle and top portion, has the smallest number of vugs and thus the smallest permeability. Sample C, the middle portion, has more vugs than sample B but less than sample A and thus has permeability between that of sample A and sample B.
- Seven types of pore space were characterized on a computational sub-sample of the CT scanning data. The analysis showed that 64% of the total pore volume is in vugs and the remaining 36% is in matrix pore space. The vugs can be subdivided into a touching-vug network and a large number of separate vugs that account for 43% and 21% of the total pore volume, respectively. The touching-vug network can be further subdivided into a flowing-vug volume and dead-end-vugs accounting for 21% and 22% of the total pore volume, respectively.
- Early tracer breakthrough was observed from the tracer experiments and a long tail appeared in the effluent concentration history. This indicated the presence

of both bypassing and dead-end regions in the vuggy sample. At least three significant time scales were deduced from the tracer experiment corresponding to (1) a fast-flowing network of touching vugs, (2) dead-end-vugs having slower tracer transfer to and from the touching-vug network, and (3) separate vugs and matrix pore space with even slower tracer transport rates. Capillary tube model and effluent tracer concentration moment analysis indicate that most of the flow moves through a small fraction of the pore space.

- The one-third power averaging method for the permeability upscaling in the simulations works well in preserving the flow properties. However, it does not preserve as well the transport properties for the vuggy system with a binary permeability field assigned with a permeability ratio of 10,000.
- Tracer transport in this vuggy carbonate sample cannot be explained by the standard 1D convection dispersion model. Rather, the observed transport behavior is a complicated convolution of tracer transferring among the flowing-vug network, the dead-end-vugs, the separate vugs, and the matrix pore space through mechanisms of convection, dispersion, diffusion, and mixing that cannot be explained by a single dispersivity value. From the best understanding of the author, there is no available miscible flooding model in the literature that can successfully explain the transport behavior of flow through this vuggy system.
- The Parssim simulation cannot predict the effluent concentration histories from the experiment. This indicates that applying Darcy's law in vugs in the simulations might not be adequate. Instead, coupled Darcy-Stokes simulation, using Darcy's law in the matrix and Stokes' law in the vugs might be necessary for accurate transport simulations.

- The simulated concentration history with explicit modeling of dispersion in the simulation actually shows less dispersive behavior than that without dispersion modeling for lower upscale levels (finer grids). This suggests that assigning dispersivity uniformly to both the vug and the matrix may not be adequate. Instead, a dispersivity field with various values corresponding to the permeability field might be necessary for reasonable simulation results. This can be done using the nonuniform dispersion option in the Parssim simulator in future transport simulations. It was also found that without dispersivity upscaling, the concentration history with dispersion modeling in the simulation does show more dispersive behavior than that without dispersion modeling for higher upscale levels (coarser grids). This suggests that it might be necessary to upscale the dispersivity along with the permeability to get consistent results.
- Similar simulation results were obtained from touching-vug network simulations. This suggests that touching-vug network systems can be used to represent the full CT scan field.

7.2 FUTURE STUDY

The work in this dissertation provides some preliminary results of studies on vuggy carbonates with a highly heterogeneous nature. However they are by far not enough to completely understand the physics of flow and transport through the vuggy system. More work is needed to better understand vuggy carbonates. Some future studies that the author can foresee are listed in the following, among which some are currently ongoing.

- Numerical simulations should be conducted on the sub-samples corresponding to those used in the physical experiments; thus, a better comparison of

simulations and experiments, and hence a better understanding, can be achieved.

- Standard core flooding studies on limestone samples with holes cut in them, mimicking vugs in the Cretaceous carbonate, should be performed.
- Core studies on vuggy carbonate samples from the Pipe Creek Reef outcrop should be conducted.
- Field tests should be performed in the Pipe Creek Reef outcrop. This include both flow and tracer tests. The understanding of the vugs interconnectivity would thereby be improved to a much larger field scale.

Appendix A Effective Permeability Derivation for the Bucket Geometry System in Flow Experiments on Sample A

The experimental apparatus of flow through sample A is shown in Fig. A1. This appendix derives the effective permeability of the combined experimental system and of the rock.

- Effective permeability of the combined system

Some relations between the radius and the height for the bucket geometry are derived first and the effective permeability of the combined system is then derived from Darcy's law. For the bucket geometry shown in Fig. A1, Eq. A.1 is true. The variable R (Eq. A.2) is derived from Eq. A.1.

$$\frac{R - R_{out}}{R_1 - R_{out}} = \frac{L - z}{L} \quad (\text{A.1})$$

$$R = R_1 + \frac{z}{L}(R_{out} - R_1) \quad (\text{A.2})$$

where R is the radius of the bucket in an arbitrary location below the surface of $z = 0$,

$$R_{out} < R < R_1, [\text{L}],$$

R_{out} is the radius of the bucket at the outlet, [L],

R_1 is the radius of the bucket above the combined system at the surface $z = 0$, [L],

L is the total length of the combined system, $L = L_1 + L_2 + L_3$, [L],

z is a variable indicating the length below surface $z = 0$, $0 < z < L$, [L].

Using Eq. A2, the bucket radius above the rock, R_2 , can be expressed as shown in Eq. A3. The bucket radius above the combined system, R_1 , can also be derived similarly from Eq. A.4 as shown in Eq. A.5.

$$R_2 = R_1 + \frac{L_2}{L}(R_{out} - R_1) \quad (A.3)$$

$$\frac{R_1 - R_{out}}{R_{in} - R_{out}} = \frac{L}{L + h} \quad (A.4)$$

$$R_1 = R_{out} + \frac{L}{L + h}(R_{in} - R_{out}) \quad (A.5)$$

where R_2 is the radius of the bucket above the rock, [L],

R_{in} is the radius of the bucket at water inlet, [L],

h is the height of water above the combined system, [L].

The flow rate for flow through the combined system can be expressed as Eq. A.6, which shows Darcy's law in a differential form.

$$q = -\frac{k}{\mu} \frac{d\Phi}{dz} A(z) \quad (A.6)$$

$$d\Phi = -\frac{q\mu}{k} \frac{dz}{A(z)} \quad (A.7)$$

$$A(z) = \pi R^2 \quad (A.8)$$

where q is the flow rate, [L^3T^{-1}],

Φ is the potential, [$ML^{-1}T^{-2}$],

μ is the viscosity, [$ML^{-1}T^{-1}$],

k is the permeability, [L^2],

$A(z)$ is the area of the bucket, which is a function of z , [L^2].

The bucket cross-section area shown in Eq. A.8 can be expressed as a function of depth z after substituting bucket radius R (shown in Eq. A.2) into Eq. A.8. Eq. A.7 is then integrated after substituting the bucket cross-section area into the equation. The integrated system is the combined system shown in Fig. A.1.

$$\int_{\Phi_{out}}^{\Phi_{in}} d\Phi = \int_0^L \frac{q\mu}{k} \frac{1}{\pi[R_1 + \frac{z}{L}(R_{out} - R_1)]^2} dz \quad (A.9)$$

The left hand integral in Eq. A.9 gives the potential difference, which is the hydraulic potential difference of the combined system (Eq. A.10).

$$\Phi_{in} - \Phi_{out} = \rho g(h + L) \quad (A.10)$$

where ρ is density of the water, [ML^{-3}],

g is the gravity constant, [LT^{-2}].

Therefore the effective permeability of the combined system can be derived after integrating Eq. A.9, the result is shown in Eq. A.11.

$$k_{avg} = \frac{q\mu L}{\pi R_1 R_{out} \rho g(h + L)} \quad (A.11)$$

where k_{avg} is the average permeability of the combined system, [L^2].

The potential drop over the combined system can also be expressed as Eq. A.12.

$$\Delta\Phi_{total} = \Phi_{in} - \Phi_{out} = \frac{q\mu L}{k_{avg}\pi R_1 R_{out}} \quad (A.12)$$

where $\Delta\Phi_{total}$ is the total potential drop over the entire combined system, $[ML^{-1}T^{-2}]$.

- The effective permeability of the rock

To calculate the rock permeability, the combined system was considered as three sections as shown in Figure A1. The potential drop over each of the three sections shown in the figure can be expressed similarly as that shown in Eq. A.12 as follows.

$$\Delta\Phi_1 = \frac{q\mu L_1}{k_1\pi R_3 R_{out}} \quad (A.13)$$

$$\Delta\Phi_2 = \frac{q\mu L_2}{k_2\pi R_2 R_3} \quad (A.14)$$

$$\Delta\Phi_3 = \frac{q\mu L_3}{k_3\pi R_1 R_2} \quad (A.15)$$

where $\Delta\Phi_1$ is the potential drop over section 1 of length L_1 , $[ML^{-1}T^{-2}]$,

$\Delta\Phi_2$ is the potential drop over section 2 of length L_2 , $[ML^{-1}T^{-2}]$,

$\Delta\Phi_3$ is the potential drop over section 3 of length L_3 , $[ML^{-1}T^{-2}]$,

k_1 is the average permeability of section 1, $[L^2]$,

k_2 is the average permeability of section 2, $[L^2]$,

k_3 is the average permeability of section 1, $[L^2]$,

R_3 is the radius of the bucket between section 1 and section 2, $[L]$.

The total potential drop over the combined system is the sum of the potential drops over the three sections shown in Fig. A1.

$$\frac{q\mu L}{k_{avg}\pi R_1 R_{out}} = \frac{q\mu L_1}{k_1\pi R_3 R_{out}} + \frac{q\mu L_2}{k_2\pi R_2 R_3} + \frac{q\mu L_3}{k_1\pi R_1 R_2} \quad (\text{A.16})$$

When section 3 is filled in by sand, then the permeability of this section is the sand permeability. The other situation in the experiment is that $L_3=0$. Therefore, the effective permeability of the section that contains the rock, section 2, can then be calculated from Eq. A.17.

$$k_2 = \frac{L_2}{R_2 R_3 \left(\frac{L}{k_{avg} R_1 R_{out}} - \frac{L_1}{k_1 R_3 R_{out}} - \frac{L_3}{k_3 R_1 R_2} \right)} \quad (\text{A.17})$$

In section 2, the annulus of the bucket was filled in by sand. The total flow rate coming out of section 2 is the sum of the flow coming from the annulus and the rock. The rock was assumed as a cylindrical geometry. Therefore, we have Eq. A.18.

$$\frac{k_2 A_{2avg} \Delta\Phi_2}{\mu L_2} = \frac{k_r A_r \Delta\Phi_r}{\mu L_2} + \frac{k_{annulus} A_{annulus} \Delta\Phi_{annulus}}{\mu L_2} \quad (\text{A.18})$$

where A_{2avg} is the volumetric average of the area in section 2, [L^2],

A_r is the bottom area of the rock sample, [L^2],

$A_{annulus}$ is the annulus area in section 2, [L^2],

$\Delta\Phi_r$ is the potential drop over the rock, [$ML^{-1}T^{-2}$],

$\Delta\Phi_{annulus}$ is the potential drop over the annulus around rock in section 2, [$ML^{-1}T^{-2}$],

$k_{annulus}$ is the permeability in the annulus, which is sand permeability, [L^2].

The volumetric average of the area in section 2 is shown in Eq. A.19.

$$A_{2avg} = \frac{\int_{L_2}^{L_2+L_3} \pi R_2 dz}{L_2} \quad (A.19)$$

Eq. A.19 is integrated after R_2 in this equation is substituted by Eq. A.3. The final result is shown in Eq. A.20. The annulus area $A_{annulus}$ is the difference of A_{2avg} and A_r .

$$A_{2avg} = \frac{\pi L}{3L_2(R_{out} - R_1)} \left\{ \left[R_1 + \frac{L_2 + L_3}{L} (R_{out} - R_1) \right]^3 - \left[R_1 + \frac{L_3}{L} (R_{out} - R_1) \right]^3 \right\} \quad (A.20)$$

$$A_{annulus} = A_{2avg} - A_r \quad (A.21)$$

The effective permeability of the rock can then be calculated from Eq. A.22. When the annulus is filled in by sand the $k_{annulus}$ is the sand permeability; when the annulus is filled in by impermeable was, then $k_{annulus} = 0$.

$$k_r = \frac{k_2 A_{2avg} - k_{annulus} A_{annulus}}{A_r} \quad (A.22)$$

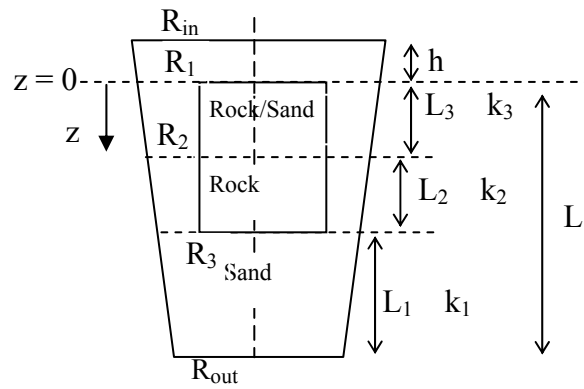


Figure A.1 Cross section sketch for rock permeability calculation.

NOMENCLATURE

A_{2avg}	Volumetric average bucket cross-section area in section 2, [L ²]
A_r	The bottom area of the rock, [L ²]
$A_{annulus}$	Annulus area between rock and bucket; [L ²]
$A(z)$	Cross-section bucket area at depth z of the bucket, [L ²]
g	Gravity constant, [LT ⁻²]
h	Water head, [L]
k	Permeability, [L ²]
k_1	Average permeability of section 1 in Fig. A.1, [L ²]
k_2	Average permeability of section 2 in Fig. A.1, [L ²]
k_3	Average permeability of section 3 in Fig. A.1, [L ²]
$k_{annulus}$	Permeability of the annulus, which is sand permeability
k_{avg}	Effective permeability of the combined system, [L ²]
k_r	Average permeability of the rock sample, [L ²]
L_1	Length of section 1 in Fig. A.1, [L]
L_2	Length of section 2 in Fig. A.1, [L]
L_3	Length of section 3 in Fig. A.1, [L]
L	Total length of the combined system, $L = L_1 + L_2 + L_3$, [L]
q	Total flow rate through the combined system, [L ³ T ⁻¹]
q_2	Total flow rate through section 2, [L ³ T ⁻¹]
q_r	Flow rate through the rock in section 2, [L ³ T ⁻¹]
$q_{annulus}$	Flow rate through the annulus in section 2, [L ³ T ⁻¹]
R	Radius of the bucket, [L]
R_1	Radius of the bucket at the surface $z = 0$, [L]
R_2	Radius of the bucket above the rock, [L]
R_3	Radius of the bucket between section 1 and section 2, [L]
R_{in}	Radius of the bucket at the inlet, [L]
R_{out}	Radius of the bucket at the outlet, [L]

z	Variable indicating the length below surface $z = 0$, $0 < z < L$, [L]
μ	Viscosity, [ML ⁻¹ T ⁻¹]
ρ	Density of water, [ML ⁻³]
Φ	Potential, [ML ⁻¹ T ⁻²]
$\Delta\Phi_{total}$	Total potential drop over the entire combined system, [ML ⁻¹ T ⁻²]
$\Delta\Phi_1$	Potential drop over section 1 of length L_1 , [ML ⁻¹ T ⁻²]
$\Delta\Phi_2$	Potential drop over section 2 of length L_2 , [ML ⁻¹ T ⁻²]
$\Delta\Phi_3$	Potential drop over section 3 of length L_3 , [ML ⁻¹ T ⁻²]
$\Delta\Phi_r$	Potential drop over the rock, [ML ⁻¹ T ⁻²]
$\Delta\Phi_{annulus}$	Potential drop over the annulus around rock in section 2, [ML ⁻¹ T ⁻²]

Appendix B Derivation of Effective Permeability of Bundle-of-Capillary-Tubes Assuming Turbulent Flow through Tubes

This appendix explains how to derive the effective permeability of the combined system when flow through the rock was modeled as turbulent flow through the bundle-of-capillary-tubes. Flow through sample A was modeled based on experiment three (see Table 4.1 for dimensions of the apparatus). Hence, the water head, the flow rate, the dimensions of the combined system in the experiment were known parameters. The combined system was divided into two sub-systems. The first sub-system was the annulus between the sample and the bucket and the annulus had only sand; thus the flow through the annulus was considered as laminar flow.

Therefore, the first step was to calculate the flow rate (Eq. B.1) through the annulus with known potential gradient and the annulus area from the experiment. The permeability of the sand was obtained from the experiment. After getting the annulus flow rate, the flow rate through the rock was calculated as the difference of the annulus flow rate from the total flow rate measured from the experiment (Eq. B.2). From the flow rate through the rock, the velocity through each capillary tube in the bundle-of-capillary-tubes model was calculated with a certain tube number and tube diameter (Eq. B.3). The Reynolds number was then obtained using Eq. B.4.

$$Q_{annulus} = \frac{k_{sand} A_{annulus}}{\mu} \nabla \Phi \quad (B.1)$$

where $Q_{annulus}$ is the flow rate of the annulus between the rock and the bucket, $[L^3T^{-1}]$,

$A_{annulus}$ is the area of the annulus between the rock and the bucket that is perpendicular to flow, [L²],

μ is the viscosity of the water, [ML⁻¹T⁻¹],

$\nabla\Phi$ is potential gradient of the combined system in experiment three, [ML⁻²T⁻²].

$$Q_r = Q_{total} - Q_{annulus} \quad (B.2)$$

where Q_{total} is the total flow rate through the combined system, [L³T⁻¹],

Q_r is the flow rate through the rock sample, [L³T⁻¹].

$$V_t = \frac{Q_r}{n \times \pi r_t^2} \quad (B.3)$$

where V_t is the velocity of each tube in the model, [LT⁻¹],

n is the number of capillary tubes,

r_t is the radius of each capillary tube, [L].

$$Re = \frac{DV_t\rho}{\mu} \quad (B.4)$$

where Re is the Reynolds number,

D is the diameter of the capillary tube, [L],

ρ is the density of the water, [ML⁻³].

The next step was to calculate the potential drop of flow through the capillary tube (Eq. B.5). At this step, the relative roughness of the tube was assumed as 0.015. This value is categorized as a tube of stave wood with less than 1 inch (2.54 cm) diameter by Moody (1944). With the known roughness and Reynolds number, the friction factor was

estimated from the Reynolds number-friction factor chart in Moody's paper if the Reynolds number was greater than 2000. When the Reynolds number was less than 2000, the Moody friction factor was calculated using Eq. B.6.

$$\frac{\Delta\Phi}{L_r} = \frac{(\Phi_0 - \Phi_{L_r})}{L_r} = \left(\frac{4}{D}\right)\left(\frac{1}{2}\rho V_i^2\right)f \quad (\text{B.5})$$

$$f = \frac{64}{\text{Re}} \quad (\text{B.6})$$

where L_r is the length of the rock, [L],

$\Delta\Phi$ is the potential drop of a tube with length L_r , [$\text{ML}^{-1}\text{T}^{-2}$],

f is the friction factor.

Because the matrix in the bundle-of-capillary-tubes model was considered as an impermeable medium, it was reasonable to assume the flow through the model as laminar flow. The potential drop across the rock in the model was assumed the same as that across each tube. Therefore, the effective permeability of the model could be estimated from Darcy's law as shown in B.7.

$$k_r = \frac{Q_r \mu L_r}{A_r \Delta\Phi} \quad (\text{B.7})$$

where k_r is the effective rock permeability estimated from the model, [L^2],

A_r is the rock area that is perpendicular to the flow direction, [L^2].

The effective permeability of the section that contains the rock was then calculated from flow in parallel as shown in Eq. B.8. The effective permeability of the combined system was estimated from flow in series as shown in Eq. 9. The geometry of experiment three is shown in Figure B1.

$$k_2 = \frac{k_r A_r + k_s A_{annulus}}{A_2} \quad (\text{B.8})$$

$$k_{avg} = \frac{L_r + L_s}{\frac{L_s}{k_s} + \frac{L_r}{k_2}} \quad (\text{B.9})$$

where A_2 is the cross section area above sand section, [L^2],

k_2 is the effective permeability of the section that contains rock (Figure B1), [L^2],

L_s is the length of the sand section (Figure B1), [L].

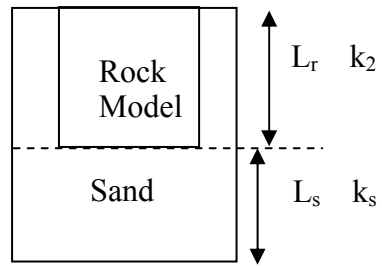


Figure B.1 Geometry of experiment three.

NOMENCLATURE

A_2	Cross section area above sand section, [L^2]
A_r	Rock area that is perpendicular to the flow direction, [L^2]
$A_{annulus}$	Area of the annulus between the rock and the bucket that is perpendicular to flow, [L^2]
D	Diameter of the capillary tube, [L]
f	Friction factor
k_r	Effective rock permeability estimated from the model, [L^2]
k_2	Effective permeability of the section that contains rock (Figure B1), [L^2]
L_r	Length of the rock, [L]
L_s	Length of the sand section (Figure B1), [L]
n	Number of capillary tubes
μ	Viscosity of the water, [$ML^{-1}T^{-1}$]
Q_{total}	Total flow rate through the combined system, [L^3T^{-1}]
Q_r	Flow rate through the rock sample, [L^3T^{-1}]
$Q_{annulus}$	Flow rate of the annulus between the rock and the bucket, [L^3T^{-1}]
Re	Reynolds number
V_t	Velocity of each tube in the model, [LT^{-1}]
$\Delta\Phi$	Potential drop of a tube with length L_r , [$ML^{-1}T^{-2}$]
$\nabla\Phi$	Potential gradient of the combined system in experiment three, [$ML^{-2}T^{-2}$]
ρ	Density of the water, [ML^{-3}]

Appendix C Sample Parssim Input File

```
# For running tracer through the level01, upscaling of the Pipe Creek sample
# Cell-centered permeability distributions
# With the boundary conditions of 600 psi inlet, 575 psi outlet
```

\$\$ GENERAL INFO

```
1 # computeFlow: Compute flow
2 # computeTransport: Compute transport
0 # computeChemistry: Compute chemistry
0 # computeRND: Compute RND

[m] # baseLength: Internal length base units
[g] # baseMass: Internal mass base units
[sec] # baseTime: Internal time base units
[degC] # baseTemperature: [degK], [degC], or [degF]
```

\$\$ SOLUTION PARAMETERS

```
2 1 1 # nDom_x, _y, _z:
      # Parallel subdomain divisions (-1=auto select)
```

\$\$\$ Flow

```
# This sectional unit is needed only if computeFlow != 0
30000 # max iterations
```

1.0E-09 # interface relative tolerance
1.0E-12 # absolute tolerance
1 # balancing preconditioner
681240000 # workspace

\$\$\$ Transport

This sectional unit is needed only if computeTransport != 0

1000 # maxIter_t: Dispersion maximum number of iterations
1.0e-06 # relTol_t: Dispersion relative tolerance
1000000 # dWorkspace_t: Double workspace for transport
-1 # cflFactor: Numerical CFL factor

\$\$\$ Chemistry

This sectional unit is needed only if computeChemistry > 0

0 # chmLoadBalFlag: Parallel chemistry load balancing
100 # chmMaxIter: Maximum number of nonlinear iterations
1.0E-10 # chmAbsTol: Absolute KKT tolerance
1.0e-30 # chmEpsConc: Minimal concentration parameter
0 # chmScaleFlag: Diagonal scaling
0 # chmTestSolFlag: Test second-order sufficiency conditions
0 # chmGuessType: initial guess (-1=auto,0=transported,1=previous)
0 # chmInterpFlag: Use interpolation in the back-track line-search
10 # nViol: Number of non-monotonic line-searches
1.0e-4 # chmAlpha: Alpha parameter
1 # hessFlag: Analytical Hessian

```
0.8      # tauMin: Movement to the boundary factor
1.0e-2   # chmRho: IP reduction factor of perturbation parameter
1        # ntReact: Number of reaction steps per transport step
0        # odeAlgType: ODE integration (0=RK1, 1=RK2, 2=RK4)
0        # switchFlag: Species switching
100000   # dWorkspace_c: Double workspace for chemistry
100000   # iWorkspace_c: Integer workspace for chemistry
```

\$\$ TIME

```
0      # tInitial: Initial time
500000 [s]      # tFinal: Final time
```

\$\$\$ Flow

```
100
1
{ 0.0 0.7 [s] }
```

\$\$\$ Transport

```
# This sectional unit is needed only if computeTransport != 0,
# computeChemistry != 0, or computeRND != 0
10000000   # nStepsMax_t: Maximum number of transport steps
100        # nStepsMax_t_per_f
1          # ndtMax_t: Number of transport time step sizes
{ 0.0      8.4040789801723967E-003 [s] }
```

\$\$ GRID

```
80 80 144 # nx, ny, nz: Number of grid cells
0 0 0
1 # zIsDepth: Direction of the z coordinate
uniform
```

Use the following when gridType is uniform

```
0.0 13.125 [cm] # xMin, xMax: Minimal and maximal x points
0.0 13.125 [cm] # yMin, yMax: Minimal and maximal y points
0.0 21.6 [cm] # zMin, zMax: Minimal and maximal z points
```

\$\$ MATERIAL PROPERTIES

```
0 # turn off gravity 9.8 [m/sec^2] # gravity: Gravitational constant
{$INCLUDE phi.01.chunk.min0.001 }
```

\$\$\$ Permeability

```
scalar
{[md] $INCLUDE perm_01_chunk-100d-1md }
```

\$\$\$ Dispersion

```
# This sectional unit is needed only if computeTransport != 0
1 # uniformDispersion: Flag for uniform dispersion
# Use this syntax if uniformDispersion is true (i.e., 1)
```

```
1.0E-07 [m^2/sec]    # molDiff: Molecular diffusion
0.005 [m]           # longDisp: Longitudinal dispersion
0.0005 [m]          # transDisp: Transverse dispersion
```

\$\$\$ Sorption

```
# This sectional unit is needed only if computeTransport != 0,
# computeChemistry != 0, or computeRND != 0
```

```
1 # nSorpTypes: Number of sorption types
```

```
# For each of the nSorpTypes sorption types, give the following
```

```
{ porosity } # sorp: Sorption capacities
```

\$\$ PHASE PROPERTIES

```
1.0 [cp]           # fluidViscosity: Flowing phase viscosity
```

```
1000 [kg/m^3]     # fluidDensity: Flowing phase mass density
```

```
1                 # nPhases: Number of phases
```

```
$$$ Phase # 1
```

```
Aqueous           # phaseNames: Phase name
```

```
multi-species     # phaseType: multi-species or single-species
```

```
55.55             # chmPhaseDensity: Molar density
```

\$\$ CHEMISTRY

```
# This sectional unit is needed only if computeChemistry > 0
```

298.0 # absTemp: Equilibrium temperature
1.0 # chemPres: Equilibrium pressure
ideal # ideal: ideal or non-ideal

\$\$ CHEMICAL SPECIES

1 # nComps: Number of components
0 # nProducts: Number of products
nSpecies = nComps + nProducts

\$\$\$ Component #1

Tracer # specieName: Specie name
1.0 # molecularWeight: Molecular weight
0.0 # phaseDist: The alpha parameter in Henry's Law

SSSS Chemistry

1 # phaseIdentity: Participating phase
+1 # compCharge: Charge

\$\$ MISCIBLE DISPLACEMENT

0 # modelMiscDisp: Miscible displacement model

\$\$ INITIAL CONDITIONS

\$\$\$ Flow

This sectional unit is needed only if computeFlow = 0

\$SS Transport

This sectional unit is needed only if computeTransport != 0,

computeChemistry != 0, or computeRND != 0

{

constant 1.00E-06 # tracer

}

\$\$ BOUNDARY CONDITIONS

3 # nBCRegions: Number of boundary regions

2 # maxnBCInterp_f: Maximum number of flow interpolation times

3 # maxnBCInterp_t: Maximum number of transport interpolation times

constant 3 # bcRegion_x_min: Boundary region map

constant 3 # bcRegion_x_max: Boundary region map

constant 3 # bcRegion_y_min: Boundary region map

constant 3 # bcRegion_y_max: Boundary region map

constant 1 # bcRegion_z_min: Boundary region map

constant 2 # bcRegion_z_max: Boundary region map

\$SS Region # 1 THE INLET FACE

SSSS Flow

2 # inflow boundary at constant Pressure (dirichlet)

potential

1

{ 0.0 600.0 [psi] }

SSSS Transport

```
2          # constant concentration inlet
{ 1      { 0.0  1.0}  }
```

```
$$$ Region # 2 THE OUTLET FACE
```

```
$$$ Flow
```

```
2          # outflow boundary at constant pressure (2=dirichlet)
potential
```

```
1
```

```
{ 0.0      575.0 [psi]}
```

```
$$$ Transport
```

```
0          # outflow concentrations...
```

```
$$$ Region # 3
```

```
$$$ Flow
```

```
0          # no flow boundary
```

```
$$$ Transport
```

```
0
```

```
$$ WELLS
```

```
0          # nWells: Number of wells
```

```
3
```

```
# maxnWellInterp_f: Maximum number of flow interpolation times
```

```
5          # maxnWellInterp_t: Maximum number of transport interpolation times
```

\$\$ LEAKS

0 # nLeaks: Number of leaks

0 # maxnLeakInterp: Maximum number of interpolation times

\$\$ OUTPUT

1 # runNumber: Run number

Tracer test on kvar permeability set

runDescription: Title or description

5 # verbosity: Driver verbosity flag

10 # debug: Driver debug flag

output # outDir: Output directory

1 # outFormat3D: Output 3-D file format

1 # nSpeciesPerOutfile: Number of species per 3-D output file

1 # initialOut: Output 3-D initial conditions flag

1 # outFormat1D: Output 1-D file format

\$\$\$ Flow

-1

-1

+250.0 [days]

+250.0 [days]

potential

5

1

\$SS Transport

```
# This sectional unit is needed only if computeTransport != 0,  
# computeChemistry != 0, or computeRND != 0  
-10          # dStepOut_conc: Steps between concentration outputs  
0.1 [s]     # dtOut_conc: Time between concentration outputs  
1           # nHistories_t: Number of 1-D time histories  
1           # outFlags_t_1: Monitor transport progress  
1           # outFlags_t_2: Monitor transport time step cuts  
1           # outFlags_t_3: Monitor transport dispersion solver  
0           # outFlags_t_4: Debug transport CMM trace-back points  
0           # outFlags_t_5: Debug (write) transport conc  
0           # outFlags_t_6: Debug transport call and set-up  
0           # outFlags_t_7: Debug transport CMM trace-back integrals.  
0           # outFlags_t_8: Debug chemistry  
0           # outFlags_t_9: Debug transport dispersion linear system assembly
```

\$SSS History

```
1           # historyType_t: History type (1=CP, 2=CT, 3=MP, 4=MT)  
1, 1, 144   # historyIndexLo_t_x, _y, _z: Lower cell of region  
80, 80, 144 # historyIndexHi_t_x, _y, _z: Upper cell of region  
1           # nHistSpecies_t: Number of species in the history  
{  
1           # histSpecie_t: Species in the history
```

```
}  
1          # dStepOut_hist_t: Steps between history outputs  
43.7[s]   # dtOut_hist_t: Time between history outputs
```

References

- Arbogast, T., "User's guide to Parssim1: The Parallel Subsurface Simulator, Single Phase". Technical Report TICAM Report 98-13, The Center for Subsurface Modeling, Texas Institute for Computational and Applied Mathematics (now as The Institute for Computational Engineering and Science), The University of Texas at Austin, Austin, Texas, May 1998. <http://www.ices.utexas.edu/~arbogast/parssim/>.
- Arbogast, T. and Brunson, D. S.: "A Computational Method for Approximating a Darcy-Stokes System Governing a Vuggy Porous Medium," submitted.
- Arbogast, T., Brunson, D. S., Bryant, S. L., and Jennings, J. W.: "A Preliminary Computational Investigation of a Macro-Model for Vuggy Porous Media," in *Computational Methods in Water Resources XV*, C. T. Miller et al., eds., New York, 2004, Elsevier.
- Arbogast, T. and Lehr, H. L.: "Homogenization of a Darcy-Stokes System Modeling Vuggy Porous Media," submitted.
- Arns, C., Bauget, H. F., Limaye, A., Sakellariou, A., Senden, T. J., Sheppard, A. P., Sok, R. M., Pinczewski, W. V., Bakke, S., Berge, L. I., Øren, P.-E, and Knackstedt, M. A.: "Pore Scale Characterisation of Carbonates Using X-ray Microtomography," paper SPE 90368 presented at the SPE Annual Technical Conference and Exhibition held in Houston, Texas, USA, 26-29 September, 2004.
- Babadagli, T. and Al-Salmi, S.: "A Review of Permeability-Prediction Methods for Carbonate Reservoirs Using Well-Log Data," *SPE Reservoir Evaluation & Engineering*, pp 75-88, April, 2004.
- Bebout, D. G., "Lower Cretaceous Stuart City Shelf margin of South Texas: Its Depositional and Diagenetic Environments and Their Relationship to Porosity," *GCAGS Transactions*, Vol. 24, pp 56-84, 1974.
- Badarinadh, V., Suryanarayana, K., Youssef, F. Z., Sahouh, K. and Valle, A.: "Log-Derived Permeability in a Heterogeneous Carbonate Reservoir of Middle East, Abu Dhabi, Using Artificial Neural Network," paper SPE 78487 presented at the SPE 10th Abu Dhabi International Petroleum Exhibition & Conference, 13-16 October, 2002.

- Baker, L.E., "Effects of Dispersion and Dead-End Pore Volume in Miscible Flooding," *Soc. Pet. Eng. J.*, Vol. 17, pp 219-227, June, 1977.
- Bein, A., "Rudistid Fringing Reefs of Cretaceous Shallow Carbonate Platform of Israel," *AAPG Bull.*, Vol. 60, pp 258-272, 1976.
- Botton-Dumay, R., Manivit, T., Massonnat, G., and Gay, V.: "Karstic High Permeability Layers: Characterization and Preservation While Modeling Carbonates Reservoirs," paper SPE 78534 presented at the 10th Abu Dhabi International Petroleum Exhibition and Conference, 13-16 October, 2002.
- Brenner, H., "The Diffusion Model of Longitudinal Mixing in beds of Finite Length. Numerical Values." *Chemical Engineering Science*, Vol.17, pp 229, 1962.
- Brigham, W. E., "Mixing Equations in Short Laboratory Cores," *Soc. Pet. Eng. J.*, Vol. 14, pp 91-99, 1974.
- Cardwell, W. T. and Parsons, R. L., "Average Permeabilities of Heterogeneous Oil Sands," *Trans AIME*, Vol. 160, pp 34-42, 1945.
- Chilingar, G.V., Mannon, R.W., and Rieke, H.H. III: *Oil and Gas Production from Carbonate Rocks*, Elsevier, New York City, 1972.
- Coogan, A. H., Bebout, D. G., and Maggio, C., "Depositional Environments and Geologic History of the Golden Lane and Poza Rica Trends, Mexico – An Alternative View," *AAPG Bull.*, Vol. 56, pp 1419-1447, 1974.
- Coogan, A. H., "Early and Middle Cretaceous Hippuritacea (rudists) of the Gulf Coast," In D. G. Bebout and R. G. Loucks, editors, *Cretaceous carbonates of Texas and Mexico*, Applications to subsurface exploration, pp 32-70, 1977.
- Cooper, J. W., Wang, X., and Mohanty, K. K., "Non-Darcy-Flow Studies in Anisotropic Porous Media," *SPE Journal*, Vol. 4, No.4, pp 334-341, December 1999.
- Dabbouk, C., Ali, L., Williams, G. and Beattie, G.: "Waterflood in Vuggy Layer of a Middle East Reservoir – Displacement Physics Understood," paper SPE 78530 presented at the 10th Abu Dhabi International Petroleum Exhibition and Conference, 13-16 October, 2002.
- Deans, H. A., "A Mathematical Model for Dispersion in the Direction of Flow in Porous Media," *Trans. AIME*, Vol. 228, No. 49, 1963.
- Dechaseaux, C., Coogan, A. H., Cox, L. R., and Perkins, B. F., Superfamily Hippuritacea Gray, 1848.– In: *Treatise on Invertebrate Paleontology part N, Mollusca 6*,

- Bivalvia, MOORE, R. C. (ed.), Vol. 2, N749-N817, Lawrence, Kansas, Geological Society of America and University of Kansas, 1969.
- Deeds, N. E., Development and Evaluation of Partitioning Interwell Tracer Test Technology for Detection of Non-aqueous Phase Liquids in Fractured Media, *Ph.D Dissertation*, The University of Texas at Austin, 1999.
- Dehghani, K., Edwards, K. A., and Harris, P. M.: "Modeling of Waterflood in a Vuggy Carbonate Reservoir," paper SPE 38910 presented at the SPE Annual Technical Conference and Exhibition held in San Antonio, Texas, 5-8 October, 1997.
- Dehghani, K. and Kamath, J.: "High-Temperature Blowdown Experiments in a Vuggy Carbonate Core," *SPE Journal*, pp 283-287, September, 2001.
- Deutsch, C., "Estimating Block Effective Permeability with Geostatistics and Power Averaging," paper SPE 15991, unsolicited and submitted to SPE (or its predecessor organization) for consideration for publication in one of its technical journals, 1985.
- Deutsch, C., "Calculating Effective Absolute Permeability in Sandstone/Shale Sequences," *SPE Formation Evaluation*, September, Vol. 4, No. 3, pp 343-348, September, 1989.
- deZabala, E. F. and Kamath, J.: "Laboratory Evaluation of Waterflood Behavior of Vugular Carbonates," paper SPE 30780 presented at the SPE Annual Technical Conference & Exhibition held in Dallas, U. S. A., 22-26 October, 1995.
- Dwarakanath, V., Deeds, N., and Pope, G., "Error Analysis of Partitioning Interwell Tracer Tests," *Environmental Science and Technology*, Vol.33, pp 3829-3836, 1999.
- Edgell, H. S., "Significance of Reef Limestones as Oil and Gas Reservoirs in The Middle East and North Africa," presented at the 10th Edgeworth David Symposium, held at the University of Sydney, 4-5 September, 1997.
- Egermann, P., Laroche, C., Manceau, E., Delamaide, E., and Bourbiaux, B.: "Experimental and Numerical Study of Water-Gas Imbibition Phenomena in Vuggy Carbonates," paper SPE 89421 presented at the 2004 SPE/DOE Fourteenth Symposium on Improved Oil Recovery held in Tulsa, Oklahoma, U.S.A., 17-21 April, 2004.
- Gaulier, C.: "Studying Vugular Rocks By-Constant-Rate Mercury Injection," paper SPE 3612 prepared for the 46th Annual Fall Meeting of the Society of Petroleum Engineers of AIME, New Orleans, La., 3-6 October, 1971.

- Ground Water and Drinking Water Chapters, 1998 Report to Congress, *National Water Quality Inventory*. EPA 816-R-00-013, August, 2000. www.epa.gov/safewater.
- Hauns, M., Jeannin, P.-Y., and Atteia, O.: "Dispersion, Retardation and Scale Effect in Tracer Breakthrough Curves in Karst Conduits," *Journal of Hydrology*, Vol. 241, pp 177-193, 2001.
- Hicks, P. J., Deans, H. A., and Narayanan K. R.: "Distribution of Residual Oil in Heterogeneous Carbonate Cores Using X-Ray CT," *SPE Formation Evaluation*, pp 235-240, September, 1992.
- Hicks, P. J., Narayanan, K., and Deans, H. A., "An Experimental Study of Miscible Displacements in Heterogeneous Carbonate Cores Using X-Ray CT," *SPE Formation Evaluation*, Vol. 9, pp 55-60, March, 1994.
- Hidajat, I., Mohanty, K. K., Flaum, M., and Hirasaki, G.: "Study of Vuggy Carbonates Using NMR and X-Ray CT scanning," *SPE Reservoir Evaluation and Engineering*, pp 365-377, October, 2004.
- Himmelblau, D. M. and Bischoff, K. B., *Process Analysis and Simulation: Deterministic Systems*, pp 69-80, John Wiley & Sons, Inc., New York, 1968.
- Houseworth, J. E., "Characterizing Permeability Heterogeneity in Core Samples From Standard Miscible Displacement Experiments," *SPE Formation Evaluation (SPEFE)*, June, 1993.
- Hristopulos, D. T. and Christakos, G., "Renormalization Group Analysis of Permeability Upscaling", *Stochastic Environmental Research and Risk Assessment*, Vol. 13, pp 131-160, 1999.
- Iwere, F. O., Moreno, J. E., Apaydin, O. G., Ventura, L. V., and Garcia, J. L.: "Vug Characterization and Pore Volume Compressibility for Numerical Simulation of Vuggy and Fractured carbonate Reservoirs," paper SPE 74341 presented at the SPE International Petroleum Conference and Exhibition in Mexico held in Villahermosa, Mexico, 10-12 February, 2002.
- Jennings, J. W. and Lucia, F. J.: "Predicting Permeability from Well Logs in Carbonates with a Link to Geology for Interwell Permeability Mapping," *SPE Reservoir Evaluation & Engineering*, pp 215-225, August, 2003.
- Jennings, J. W., Lucia, F. J., Bryant, S. L., Arbogast, T. J., Brunson, D. S., Ketcham, R. A., and Colbert, M. W., "Progress Report: Cretaceous Touching-Vug Pore Systems," The University of Texas at Austin, March, 2001.

- Journel, A. G., Deutsch, C. V., and Desbarats, A. J., "Power Averaging for Block Effective Permeability," paper SPE 15128 presented at the 1986 SPE California Regional Meeting, Oakland, 2-4 April, 1986.
- Ketcham, R. A. and Carlson, W. D., "Acquisition, Optimization and Interpretation of X-ray Computed Tomographic Imagery: Applications to the Geosciences," *Computers and Geo-sciences*, Vol. 27, pp 381-400, 2001.
- Kosakowski, G., Berkowitz, B., and Scher, H.: "Analysis of Field Observations of Tracer Transport in a Fractured Till," *Journal of Contaminant Hydrology*, Vol. 47, pp 29-51, 2001.
- Koval, E. J., "A Method for Predicting the Performance of Unstable Miscible Displacement in Heterogeneous media," *Soc. Pet. Eng. J.*, pp 145-154, June, 1963.
- Lucia, F. J.: "Petrophysical Parameters Estimated from Visual Description of Carbonate Rocks: a Field Classification of Carbonate Pore Space," *J. Pet. Tech.* (1983) Vol. 35, pp 626-637.
- Lucia, F. J., *Carbonate Reservoir Characterization*, Springer-Verlag, Berlin, (1999).
- Lucia, F. J.: "Petrophysical Parameters Estimated from Visual Description of Carbonate Rocks: a Field Classification of Carbonate Pore Space," *J. Pet. Tech.*, Vol. 35, pp 626-637, 1983.
- Lucia, F. J.: "Rock-Fabric/Petrophysical Classification of Carbonate Pore Space for Reservoir Characterization," *AAPG Bulletin*, Vol. 79, pp 1275-1300, 1995.
- Lucia, F. J., Kerans, C., and Jennings, J. W., "Carbonate Reservoir Characterization," *Journal of Petroleum Technology*, pp 70-72, June, 2003.
- Marzouk, I., Takezaki, H., and Suzuki, M.: "New Classification of Carbonate Rocks for Reservoir Characterization," paper SPE 49475 selected for presentation at the 8th Abu Dhabi International Petroleum Exhibition and Conference held in Abu Dhabi, U.A.E., 11-14 October, 1998.
- Massonnat, G. and Pernarcic, E.: "Assessment and Modeling of High Permeability Areas in Carbonates Reservoirs," paper SPE 77591 presented at the SPE Annual Technical Conference and Exhibition held in San Antonio, Texas, 29 September-2 October, 2002.
- Mathisen, T., Lee, S. H., and Datta-Gupta, A.: "Improved Permeability Estimates in Carbonate Reservoirs using Electrofacies characterization: A Case Study of the

- North Robertson Unit, West Texas,” *SPE Reservoir Evaluation & Engineering*, pp 176-184, June, 2003.
- Maxfield, B. T., Ginosar, D. M., and McMurtrey R. D., “Evaluation of Fluorocarbon Tracer Retention in Dry and Wet Sand Column Tests,” *Geothermal Resource Council Transaction*, Vol. 26, pp 22-25, September, 2002.
- Mennella, A., Bryant, S. L., and Lockhart, T. P., “Analysis of High-Dispersion Tracer Tests in Cores Containing Polymer Gels,” *Journal of Petroleum. Science and Engineering*, Vol. 23, pp 201-212, 1999.
- Moctezuma-Berthier, A. and Fleury, M., “Permeability Mapping on Vuggy Core Sample Using Tracer Experiments and Streamline Simulations,” SPE 58992, this paper was prepared for presentation at the 2000 SPE International Petroleum Conference and Exhibition in Mexico held in Villahermosa, Mexico, 1-3 February, 2000.
- Moctezuma-Berthier, A., Vizika, O., Thovert, J. F., and Adler, P. M.: “One- and Two-Phase Permeabilities of Vugular Porous Media,” *Transport in Porous Media*, Vol. 56, pp 225–244, 2004.
- Moody L. F.: “Friction Factor for Pipe Flow,” *Transactions of the A.S.M.E.*, pp 671-684, November, 1944.
- Narayanan, K. and Deans, H. A., “A Flow Model Based on the Structure of Heterogeneous Porous Media,” paper SPE18328 presented at the 1988 SPE Annual Technical Conference and Exhibition, Houston, 2-5 October, 1988.
- Noetinger, B., “The Effective Permeability of a Heterogeneous Porous Medium,” *Trans. Porous Media*, Vol. 15, pp 99-127, 1994.
- Noetinger, B. and Jacquin, C., “Experimental tests of a Simple Permeability Composition Formula,” paper SPE 22841 presented at the 1991 SPE Annual Technical Conference and Exhibition held in Dallas, TX, 6-9 October, 1991.
- Qassim, N. A., Jawad, W. A., and Abdulwabha, A. E.: “Creative Modeling of a Heterogeneous Carbonate Reservoir in Bahrain Field (Kharai Reservoir),” paper SPE 81531 presented at the SPE 13th Middle East Oil Show & Conference in Bahrain 5-8 April, 2003.
- Okasha, T. M., Funk, J. J., and Al-Enezi, S. M.: “Wettability and Relative Permeability of Lower Cretaceous Carbonate Rock Reservoir, Saudi Arabia,” paper SPE 81484 presented at the SPE 13th Middle East Oil Show & Conference held in Bahrain, 5-8 April, 2003.

- Ramakrishnan, T. S., Rabaute, A., Fordham, E. J., Ramamoorthy, R., Herron, M., Matteson, A., and Raghuraman, B.: "A Petrophysical and Petrographic Study of Carbonate Cores from the Thamama Formation", paper SPE 49502 presented at the SPE 8th Abu Dhabi International Petroleum Exhibition & Conference held in U.A.E., 11-14 October, 1998.
- Ramakrishnan, T. S., Ramamoorthy, R., Fordham, E., Schwartz, L., Herron, M., Saito, N. and Rabaute, A.: "A Model-Based Interpretation Methodology for Evaluating Carbonate Reservoirs", paper SPE 71704 presented at the SPE Annual Technical Conference and Exhibition, New Orleans, 30 September-3 October, 2001.
- Renard, Ph. and de Marsily, G., "Calculating Equivalent Permeability: A Review," *Advances in Water Resources*, Vol. 20, No. 5-6, pp 253-278, 1997.
- Paruchuri, R. K. Modeling Flow and Transport in Heterogeneous Media, *Master Thesis*, December, 2003
- Petta, T. J., "Diagenesis and Geochemistry of a Glen Rose Patch Reef Complex, Bandera County, Texas," In D. G. Bebout and R. G. Loucks, editors, *Cretaceous carbonates of Texas and Mexico*, Applications to subsurface exploration, pp 138-167, 1977.
- Perkins, B. F., "Paleoecology of a Rudist Reef complex in The Comanche Cretaceous Glen Rose Limestone of central Texas," In B. F. Perkins, editor, *Aspects of Trinity Division Geology*, Volume 8 of Geoscience and Man, pages 131-173, Louisiana State University, 1974.
- Rose, P. R., "Comparison of Type EI Abra of Mexico With the 'Edwards reef trend' of South Central Texas" Corpus Christi Geological Society Annual Meeting field Trip, Perigrina Canyon and Sierra del EI Abra, pp 57-64, 1963.
- Shedid, S. A., and Almehaideb, R. A.: "A New Approach of Reservoir Description of Carbonate Reservoirs", SPE 74344, presented at the SPE International Petroleum Conference and Exhibition in Mexico held in Villahermosa, Mexico, 10-12 February 2002.
- Shook, G. M.: "A Simple, Fast Method of Estimating Fractured Reservoir Geometry from Tracer Tests," *Geothermal Resources Council Transactions*, Vol. 27, 12-15 October, 2003
- Shook, G. M. and Forsmann, J. H., "Tracer Interpretation Using Temporal Moments on a Spreadsheet," prepared for the U. S. Department of Energy Assistant Secretary for Energy Efficiency and Renewable Energy, Contract DE-AC07-05ID14517, Geothermal Technologies Program, Idaho National Laboratory, June, 2005.

- Shook, G. M.: "A Systematic Method, An Alternative Tracer Test Analysis Using Bevoware," *Reservoir Engineering*, pp 31-35, January/February 2005.
- White, W. B.: "Karst Hydrology: Recent Developments and Open Questions," *Engineering Geology*, Vol. 65, pp 85-105, 2002.
- Wilson, J. K. *Carbonate Facies in Geological History*, Springer-Verlag, New York, 1975.
- Xu, B., Kamath, J., Yortsos, Y. C. and Lee, S. H., "Use of Pore-Network Models to Simulate Laboratory Corefloods in a Heterogeneous Carbonate sample," *SPE Journal* , Vol. 4, No. 3, pp 179-186, September, 1999.

Vita

Liyang Zhang was born on November 2, 1976 in Heilin, Yushu, Jilin Province in China, the daughter of Zhilin Zhang and Suyun Xie, the elder sister of Liqing Zhang and Qiuying Zhang. After graduating from Shiyan High School in Yushu city in 1995, she entered the Petroleum Engineering Department at Daqing Petroleum Institute, Anda, Heilongjiang Province. She received her Bachelor of Science in 1999 and entered graduate school in the Petroleum Engineering Department at Daqing Petroleum Institute. In 2002, she graduated with her Master of Science and entered the Department of Petroleum and Geosystems Engineering at the University of Texas at Austin. She presented an SPE paper in 2004.

Permanent Address: Zhang Zhibao Clinic
Yushu, Jilin Province, 130400
People's Republic of China

This dissertation was typed by Liyang Zhang.